2011-03-16

Pyrolysis Kinetics and Chemical Structure Considerations of a Green River Oil Shale and Its Derivatives

James L. Hillier
Brigham Young University - Provo

BYU ScholarsArchive Citation

Hillier, James L., "Pyrolysis Kinetics and Chemical Structure Considerations of a Green River Oil Shale and Its Derivatives" (2011). *Theses and Dissertations*. 2606.
https://scholarsarchive.byu.edu/etd/2606

Pyrolysis Kinetics and Chemical Structure Considerations of a Green River Oil Shale and its Derivatives

James Lyle Hillier

A dissertation submitted to the faculty of
Brigham Young University
in partial fulfillment of the requirements for the degree of

Doctor of Philosophy

Thomas H. Fletcher, Chair
Ronald J. Pugmire
W. Vincent Wilding
William C. Hecker
William G. Pitt

Department of Chemical Engineering

Brigham Young University

April 2011

ABSTRACT

Pyrolysis Kinetics and Chemical Structure Considerations of a Green River Oil Shale and its Derivatives

James Lyle Hillier
Department of Chemical Engineering
Doctor of Philosophy

This work had the objective of determining both the kinetic parameters for the pyrolysis of oil shale and kerogen as well as using analytical techniques coupled with pyrolysis to shed light on the structure of a specific Green River oil shale. Because of the problems with linearized methods and disagreement among literature values and methods, a new method was developed to fit kinetic parameters to non linearized data. The method was demonstrated to determine the "correct" answer for mathematically generated data within a few percent error and was shown to have a lower sum squared error than the linearized methods.

The curve-fitting methodology was then applied to pyrolysis kinetic data for kerogen and oil shale. Crushed samples were pyrolyzed at heating rates from 1 to 10 K/min and at pressures of 1 and 40 bar. The transient pyrolysis data were fit with a first-order model and a progressive Distributed Activation Energy Model (DAEM). An F-test was used to determine confidence regions and compare the kinetic parameters among the samples. The activation energies determined ranged from 173 to 226 kJ/mol, with most values around 200-220 kJ/mol. The kinetic coefficients determined for oil shale and the demineralized samples were statistically the same. Only small differences in kinetic coefficients were seen in the size-graded samples. The first-order and DAEM were shown to be statistically different, but a visual inspection of a graph of the model predictions and the data revealed that both models performed well. The largest effect on the kinetic parameters was between samples collected from different geographical locations.

The pyrolysis products (and the parent kerogen sample) were analyzed by several chemical techniques to determine chemical structure information about the parent sample. The GC/MS data for the tars collected showed a distribution of alkenes/alkanes with 11 to 12 carbons in length being the most frequent. XPS analysis demonstrated that any chemical model must have pyridinic and pyrrolic nitrogens as well as carbonyls and carboxyl groups. Therefore a chemical structure model of kerogen should have heteroatoms of nitrogen in the aromatic region (i.e., the portions of the kerogen that are stable at moderate temperatures).

Keywords: James Hillier, oil shale, kerogen, TGA, thermogravimetry, pyrolysis

ACKNOWLEDGMENTS

It takes lots of time and effort to complete the steps necessary to finish a dissertation. I have been helped along the way by many people. First of all I must acknowledge and thank my wife, Ashley, who spent many hours helping me and being with me as I raced to finish for deadlines and for her constant support. Secondly I must thank my parents who always encouraged education and supported me throughout my formal education. I would like to thank Thomas Fletcher for his guidance, encouragement, and time spent on my behalf through out the past few years.

I must thank those who helped me collect the necessary information to put into this dissertation. I would like to thank Ron Pugmire and Mark Solum for collecting the NMR data, Michael Chang for helping with understanding of GC/MS, and the undergraduates who helped collect a significant portion of the data used herein. I would also like to thank Chevron for the research funds to complete this project, and I trust that the data are useful to them. Finally I must thank God for his help in everything good I have ever undertaken.

TABLE OF CONTENTS

LIST OF TABLES

LIST OF FIGURES

NOMENCLATURE

A	Pre-exponential factor
A′	modified pre exponential- $A' = 10^{(\log A)/10}$
ASTM	a voluntary standards developing organization
B_C	bridges and loops per cluster
C	number of carbons per cluster
C_x	x number of carbons in a hydrocarbon chain
CHNS	Carbon, Hydrogen, Nitrogen, and Sulfur analysis
CPD	Chemical Percolation Model
d/d_{max}	ratio of the distributed variable to its maximum
DAEM	distributed activation energy model
DAF	dry ash free
E	Activation energy
$\overline{E}$	Mean activation energy
EGA	Evolved gas analysis
f_a	aromatic carbons
f_a^C	the fraction of carbonyl and carboxyl carbons
f_a'	aromatic carbons with carbonyls subtracted
f_a^H	protonated aromatic carbons
f_a^N	total non protonated aromatic carbons
f_a^P	aromatic carbon with oxygen carbon attachment
f_a^S	aromatic carbon with alkyl attachment
f_a^B	aromatic bridgehead and inner carbons
f_{al}	aliphatic carbon
f_{al}^H	aliphatic CH and CH_2
f_{al}^*	aliphatic CH_3 and non protonated carbons
f_{al}^O	aliphatic carbon with oxygen attachment
F	F-statistic value
F_{crit}	critical F-statistic value from F-distribution
FTIR	Fourier transform infrared spectroscopy
fwhm	full width half maximum
GC	Gas Chromatograph
GRG	generalized reduced gradient
GROS	Green River Oil Shale
H	heating rate (K/min)
H_0	null hypothesis
k	kinetic coefficient
k_{model}	kinetic coefficient for mathematical model
k_{actual}	kinetic coefficient for mathematical data
m	mass
m_i	i^{th} calculated mass point
m_{i-1}	i^{th}-1 calculated mass point
m_o	initial mass

m'	scaled mass
m'_{normal}	normalized scaled mass
m'_f	final scaled mass
m'_o	initial scaled mass
MS	mass spectrometry
m/z	mass to charge ratio
NMR	nuclear magnetic resonance
n	reaction order or number of observations
p	number of parameters in an equation
p_1	number of parameters in equation 1
p_2	number of parameters in equation 2
P	fraction of intact bridges per cluster
R	ideal gas constant
SA	simulated annealing
SS	sum squared error
t	time (seconds)
T	temperature
T_0	initial temperature
T_i	i^{th} temperature point
T_{max}	temperature of the maximum rate of mass loss
TGA	Thermogravimetric analyzer
TOC	total organic content
XPS	X-ray photoelectron spectroscopy
XRD	X-ray diffraction

Greek Symbols

α	conversion of reactant or confidence level
ε_i	error associated with the i^{th} point
σ	distribution
$\sigma+1$	total attachments per cluster
θ	vector of parameters for an equation
$\hat{\theta}$	vector of parameters for an equation that minimizes the sum squared error

1. **Introduction**

The rise in energy costs has propelled the world to search for alternate sources of energy. Many sources of energy have been considered to supply the increased demand of energy. One source of potential energy is the organic matter in oil shale. As an energy source it is particularly attractive because of its potential to supply the transportation needs of a growing population without a drastic change in established infrastructure. This is because this organic matter can be a raw material to make a product that is similar to conventional liquid hydrocarbon fuels and can be refined into gasoline, diesel fuel, or other high value products.

The organic matter in oil shale is referred to as kerogen. Kerogen is a rather broad definition that encompasses more that 10^{16} tons of carbon worldwide including substances such as oil, coals, as well as the organic matter in oil shale (Vandenbroucke and Largeau, 2007). In this dissertation kerogen refers to the organic portion of oil shale and is bound to a mineral matrix to form the oil shale. This type of kerogen in oil shale represents approximately 10^{12} tons of carbon. The kerogen is divided into types (I, II, or III) based on hydrogen to carbon ratios. One researcher estimates that about 3 trillion equivalent barrels of oil are recoverable from oil shale (Dyni, 2006). The Green River formation spans parts of Utah, Wyoming, and Colorado and contains about 60% of the world's oil shale (by another estimate) which translates to 1.2 trillion barrels oil equivalent (Andrews, 2006; Dyni, 2006). Even conservative estimates conclude that there are at least 800 billion barrels recoverable in this formation.

Oil shale was studied extensively in the 1970s and early 80s when oil prices were high, but due to low oil prices in the late 80s and during the 90s most research in the field was halted. During the current decade oil shale research interest has returned--spurred on by the rising cost of oil. Because of lessons learned during the last oil shale boom, the ever increasing environmental awareness, and governmental regulations, current research is attempting to develop new methods of high efficiency surface processing or *in-situ* methods to lessen environmental impact. Mining and subsequent above ground oil shale retorting (processing) are environmentally damaging because of the amount of water needed, the mining process, and the nature of the waste produced. Many current industrial research projects are focused on investigating *in-situ* oil recovery processes with reduced environmental damage.

These new industrial objectives as well as improved analytical techniques have opened up areas of research in the structure and kinetics of the kerogen in oil shale. These techniques give information about the ratio of oxygen atoms to nitrogen atoms in the structure, as well as what a representative chemical structure might need to include. Oil shale research has been enabled by techniques developed in the last 30 years to extract the kerogen from the mineral matrix. This work utilized both extracted kerogen and the parent oil shale to determine kinetic parameters, a chemical reactivity model, and chemical structure aspects of the kerogen. The results of this research were utilized by a larger research group to construct a working chemical structure model of the kerogen from the Green River formation.

2. Literature Review

This literature review is organized into four sections: Kinetic Parameter estimation from TGA data, Kinetic Parameters for Oil Shale, Chemical Structure Work, and Chemical Reactivity Models.

2.1. Kinetic Parameter Estimation from TGA Data

Thermogravimetry Analysis or TGA is a common technique to determine global kinetic parameters for complex reactions parameters (Freeman and Carroll, 1958; Doyle, 1961; Coats and Redfern, 1964; Campbell et al., 1978; Burnham and Braun, 1999; Li and Yue, 2003; Abu-Qudais et al., 2005; Shao et al., 2008). TGA analysis has been used in many industries ranging from coal char oxidation (Hecker et al., 2003) to analysis of sewage sludge pyrolysis (Scott et al., 2006a; Scott et al., 2006b). These global kinetic parameters (i.e., the activation energy and pre-exponential factor used in the Arrhenius equation) are useful from a modeling and engineering standpoint to describe reaction behavior.

Thermogravimetry involves the measurement of the mass of the sample while heating the sample. As the sample heats up it reacts and mass is released in the form of a vapor or gas. There are two common TGA systems employed: open systems and closed systems. An open system is so named because the sample is exposed to a sweep substance that constantly replaces the medium around the sample and sweeps the products away. This sweep substance is often a well-controlled gas atmosphere. The closed system consists of a sample isolated in a reaction cell, and reaction products persist around the sample. In a closed system some of the reaction products may react with and be reincorporated into the sample. A majority of systems utilize a controlled atmosphere of gases, but one specialized form of a closed TGA utilizes water as the medium and a magnetic balance (Mochidzuki et al., 2000).

Generally mass loss measurements are made at either isothermal conditions or at a constant heating rate. One of the two aforementioned general methods, isothermal, is performed by heating the sample as quickly as possible to the reaction temperature and holding the sample at that temperature while recording the mass versus time. This has been a technique utilized by many researchers (Doyle, 1961; Campbell et al., 1978; Lee, 1991; Vyazovkin and Wight, 1999; Williams and Ahmad, 2000). An isothermal analysis is often carried out by plotting the rate constant from multiple experiments of various temperatures against the inverse of temperature on a log plot. The activation energy, E, is determined from the slope and the kinetic frequency factor is determined from the intercept. Non-isothermal studies involve heating a sample in an apparatus, often linearly with time (i.e., a constant heating rate), and measuring the weight with respect to time or temperature. Time and temperature are usually related through some algebraic expression. In the case of a linear heating rate the expression would be:

$$T = H \cdot t + T_0 \tag{1}$$

Where T is temperature, H is heating rate, t is time, and T_0 is the initial temperature.

Once a mass (or conversion) versus time curve has been generated using the TGA with an experiment, the particular method of determining the activation energy can lead to differing results. This reduction method linearizes the data, and the kinetic parameters can then be determined from the slope and intercept of the resulting linearized equation. Traditional non-isothermal experiments also involve linearizing an equation in some manner and fitting the resulting straight line to obtain activation energy, pre-exponential factor, and reaction order (Rajeshwar, 1981; Lee, 1991; Dogan and Uysal, 1996; Torrente and Galan, 2001; Abu-Qudais et al., 2005). There are some researchers who have pointed out that linearization of an equation is not necessary (Burnham and Braun, 1999).

A first-order global reaction with an Arrhenius form of the rate constant is often assumed:

$$\frac{dm}{dt} = -A \cdot \exp\left(\frac{-E}{R \cdot T}\right) \cdot m \tag{2}$$

where T represents the temperature of the sample, A is the pre-exponential factor, and m is the mass. Equation 2 is a special case of the more general n^{th} order equation (n is the reaction order):

$$\frac{dm}{dt} = -A \cdot \exp\left(\frac{-E}{R \cdot T}\right) \cdot m^n \tag{3}$$

The kinetic expressions shown are not “true” explanations of the mechanism but provide useful equations for engineering applications.

Traditionally there have been two classes of methods utilizing non-isothermal data to determine the kinetic parameters used in Equation 2 (Popescu C., 1998). One method simply requires a linearization of this equation by dividing by the mass and then taking the natural log or log10 of both sides. The resulting equation is shown here as Equation 4 and is referred to as the derivative method in this work.

$$\ln\left(-\left[\frac{dm}{dt}\right]\Big/m\right)=\ln(A)-\frac{E}{RT} \tag{4}$$

Equation 4 is in a linear form so that when the left side of the equation is plotted on the ordinate and 1/T on the abscissa, the resulting graph is a straight line when the reaction is first order. The slope of the straight line yields the activation energy, and the pre-exponential factor can be determined from the intercept. Equation 4 suffers from at least two problems. The first problem is an often numerically imprecise evaluation of the derivative. The second problem is that this equation naturally desensitizes the pre-exponential factor by taking the log of its value. The intercept is found by extrapolation of the data, and small errors in the intercept become large when the pre-exponential factor is determined.

The other common method for determining kinetic parameters from non-isothermal data is to use an integral method.

$$\int_{m_0}^{m}\frac{dm}{m}=\int_0^t -A\cdot e^{-E/R\cdot T}\,dt \tag{5}$$

$$m=m_0\cdot\exp\left(\int_0^t -A\cdot e^{-E/R\cdot T}\;dt\right) \tag{6}$$

Many researchers have turned to using solutions to Equation 2 that are based upon conversion or a normalized mass (Karabakan and Yurum, 1998; Jaber and Probert, 2000; Kok and Pamir, 2003; Benbouzid and Hafsi, 2008). These solutions use approximations to the right hand side of Equation 6 and subsequent linearization to fit the mass versus temp curve, an activation energy and pre-exponential factor can then be obtained (Coats and Redfern, 1964; Ozawa, 1965). There are a few different versions of an integrated form that can be cast into a similar form (Popescu et al., 1992). The Coats and Redfern linearized solution is shown in Equation 7.

$$Log_{10}\left[\frac{-Log_{10}(1-\alpha)}{T^2}\right] = Log_{10}\left[\frac{A \cdot R}{H \cdot E} \cdot \left(1 - \frac{2 \cdot R \cdot T}{E}\right)\right] - \frac{E}{2.3 \cdot R \cdot T} \qquad (7)$$

In Equation 7, α represents the fraction of sample decomposed, A is the pre-exponential factor, E is the activation energy, R is the ideal gas constant, and H is the heating rate. The integral method trades the simpler but imprecise derivative method for the solution to Equation 2 by integration. However, the resulting integral of the right hand side of Equation 6 has no analytical solution and therefore some approximations must be made to arrive at the solution. The Coats and Redfern (1964) derivation uses an approximation of the integral from an infinite sum. The resulting approximation (changed from the traditional Log usage by Coats and Redfern to a Ln usage) is shown in Equation 8 for the case where the reaction order is one (after neglecting some terms in the derivation). These assumptions have been shown to diminish the ability of the method to find the true set of kinetic parameters and are a source of the errors inherent in this method (Cai and Bi, 2008). The term H in Equation 7 represents the heating rate.

$$\ln\left(\frac{-\ln(m)}{T^2}\right)=\ln\left(\frac{A\cdot R}{H\cdot T}\cdot\left(1-\frac{2\cdot R\cdot T}{E}\right)\right)-\frac{E}{R\cdot T} \tag{8}$$

Equation 8 is linear with the ordinate being the LHS and the abscissa as 1/T; the activation energy can be determined from the slope by plotting the left hand side against 1/T. The first term of the right-hand side is relatively constant, can be determined from the intercept, and yields the pre-exponential factor. Equation 8 is the way the Coats and Redfern equation is shown in their paper and is similar to Equation 7. The slope yields the activation energy and the natural log of the pre-exponential factor is the intercept. These linear methods pre-date computers and are “pencil and ruler” methods. One summary of some of these methods is described by Kök and Pamir (2003).

The Coats and Redfern method is not the only form of the integral method but it is commonly found in the literature. Other forms of the integral method are some variation of Equation 8, with differing assumptions leading to a variation of activation energies of about 10% (Popescu et al., 1992; Popescu C., 1998). For example, Popescu et al. (1998) compiled a table of some 16 techniques that can be classified as differential or integral. Subsequent references in this paper to the integral method will refer to the Coats and Redfern method.

Previous “pencil and ruler” linearized methods allowed for only one set of data to be fit at a time, were developed to make up for lack of computing power, and gave “the solution” without exploring the entire range of possible solutions. These methods also require the researcher to decide which points to include in the analysis. The problem of which points to include is discussed in Section 5.3.

Isothermal and non-isothermal data require different methods to regress the kinetic parameters and within each technique there exist different ways to determine the kinetic parameters. Chapter 3 will focus on a comparison of two traditional methods and a new method developed as part of this work for analyzing non-isothermal kinetic data. This chapter will also present an evaluation of the new method and discuss one reviewer’s comments about this method. The new method utilizes some existing concepts, but the implementation of these concepts is new to this work.

2.2. Kinetic Parameters for Oil Shale

One industry that has relied extensively on TGA work is the oil shale industry where it has been used to determine kinetic parameters for modeling purposes (Granoff and Nuttall, 1977; Campbell et al., 1978; Skala et al., 1990; Williams and Ahmad, 1999; Shuyuan et al., 2001; M. Abu-Qudais, 2005). TGA experiments are simple in concept but have several difficulties in practice, especially for pyrolysis experiments. Isothermal analysis in principle starts with zero conversion during the heat up period to the experimental temperature and then proceeds with time, but in reality conversion begins during the heating period (Campbell et al., 1978). It was pointed out by Campbell that the difficulty of isothermal analysis is the result of the initial heat-up period required to reach the isothermal reaction temperature (Campbell et al., 1978). Non-isothermal techniques have also been utilized by a number of researchers as well as seen in Table 1.

Non-isothermal analysis avoids the uncertainty of the initial conditions (Campbell et al., 1978). Non-isothermal analysis starts with the temperature much lower than the reaction temperature. For example, one possibility is to start at room temperature and heat the sample at a constant and known rate through the temperature region of reaction. Then Equation 2 is solved and fit to the mass loss curve.

Table 1. Researchers employing non-isothermal TGA (and a few other) techniques to determine the kinetics of oil shale pyrolysis and oil generation. Notice the spread in the reported values. "~" means not a distributed model.

Author(s)	Sample	Experimental Setup	Heating Rate(s) (K/min)	A (s-1)	E (or Eavg) (kJ/mol)	σ (kJ/mol)
Abu-Qudais et al.(2005)	Attarat (Jordian) Oil Shale	TGA	3,5,10,20,40		79.2–91.7	~
Ahmad and Williams(1998)	Kark and Salt Range (Pakistan) Oil Shale	TGA	20		68-110,58-93	~
Avid et al.(2000)	Khoot (Mongolian) Oil Shale	TGA	92		96.28	~
Benbouzid and Hafsi(2008)	Bitumen	TGA	5,10,20	1.00E+03	37-97	~
Braun(1992)	GROS*	Pyrolysis TQ-MS	1,10	5E+13	221	Not available
Burnham(1991)	GROS	Pyromat II	0.033,2	1.1E+15	241	5.8
Campbell et al.(1980)	Green River (USA) Oil Shale	TGA	2		149	~
Dogan and Uysal(1996)	Turkish Oil Shale	TGA	20		12.5-43.4	~
Jaber and Probert(2000)	Ellujjun and Sultani (Jordan)	TGA	20,30,40,50	-1.00E-5 to -1.93E-3	39-68	~
Kök and Pamir(2003)	Can, Mengen, and Himmetoglu (Turkish) Oil Shales	TGA	10		24-57	~
Kök and Iscan(2007)	Can, Mengen, and Himmetoglu (Turkish) Oil Shales	TGA	5		13.1–215.4	~
Li and Yue(2003)	Chinese Oil Shale and GROS	TGA	5		160-200 (dominant rxns)	~
Linder et al.(1983)	Swedish Oil Shale	TGA	3.5-21.3		130	~
Rajeshwar(1981)	GROS	TGA	5,10,20	9.80E+10	116-209	~
Shih and Sohn(1980)	GROS	TGA	1-5	5.63E+11	197	~

* GROS means Green River Oil Shale

Non-isothermal experiments are generally shorter and have fewer initial condition problems than the isothermal experiments (Abu-Qudais et al., 2005). One major problem with the non-isothermal method is the difficulty of the subsequent analysis. The problem arises in determining the solution to Equation 2 due to the Arrhenius form. To simplify the solution many researchers have assumed that n (the reaction order) is ≈1.0 (Dogan and Uysal, 1996; Abu-Qudais et al., 2005). Researchers have also proposed using Equation 4 for parallel first-order reactions (Benbouzid and Hafsi, 2008).

Another proposed non-isothermal solution to the global first order equation mentioned by Campbell (1978) involves the volume of product generated. The model follows a similar form of Equation 2 but has numerically different kinetic parameters owing to the difference between a pyrolysis experiment and an oil generation experiment. The Campbell experiment tracks the amount of product created. The process is more of an oil production process at pyrolysis conditions than a pure pyrolysis process. Campbell’s approach, which tracks oil generation, differs from the more popular solutions involving conversion or normalized mass used by many researchers.

Despite the fact that a 1st order equation is commonly employed to describe the oil shale pyrolysis process, not all researchers have used a first order model. Rajeshwar and Dubow (1982) attempted to show that the kinetics of oil shale do not follow first order kinetics. However, their conclusion is that global first-order kinetic parameters agree quite well with known data. It is most likely true that there is more than one reaction occurring in the pyrolysis of oil shale, but a first order model seems to describe the process well.

2.2.1. Parameter Regression

Many of the researchers mentioned above have utilized a single first order reaction scheme, but the complexity of oil shale decomposition has led several researchers to fit multiple parallel reactions. Each reaction individually utilizes some variation of Equation 2. For example, Li and Yue (2003) used 11 parallel reactions with given activation energies to estimate the amount of sample reacting at each activation energy. If enough parallel reactions are used the model approaches a continuous distribution of activation energies which can be modeled with a Distributed Activation Energy Model (DAEM). A few individual reactivity models including the DAEM are described in the Chemical Reactivity Models Section 2.3.

2.2.2. Mineral Matrix Studies

Oil shale is composed of an organic part that is bound to a mineral matrix. The effect of the mineral matrix on the extraction and processing of the kerogen in the oil shale is not well known. To study this effect the organic portion can be separated from the mineral matrix by a series of acid washes. There have been several variations proposed on how to accomplish the separation (Vandegrift et al., 1980; Karabakan and Yurum, 1998).

The separation of the organic matrix from the mineral matrix allows researchers to identify possible interactions between the two. Some research has shown that the pyrolysis of the organics is catalyzed by the carbonates and inhibited by the silicates (Karabakan and Yurum, 1998). Karabakan and Yurum also report the change in activation energy relative to the amount of demineralization. Ballice (2005) reports that "the removal of pyrites with HNO_3 did not affect the reactivity of the organic material in pyrolysis. However, removal of the material soluble in

HF increased the conversion in pyrolysis reactions" (Ballice, 2005). Winans and coworkers (Vandegrift et al., 1980) demonstrated that the organic portions could be extracted from the oil shale using a combination of benzene and acid washes. Mraz (1984) showed that acid dissolution of the mineral matrix is enhanced by ultrasonic waves. Espitalie and coworkers (1984) showed that some catalytic activity is demonstrated by calcium ions but also stated that the effect may be enhanced because the pyrolysis occurs in an open system at high temperature in the absence of water. Conversely Reynolds and Burnham (1995) concluded that, "derived kinetic parameter and calculated oil generation curves are very similar, between the shale and the corresponding kerogen."

2.2.3. Effects of Pressure

The effects of pressure on the decomposition of oil shale are of interest for in-situ recovery of the organic material since the kerogen rich regions are often 1000 to 2000 feet underground. It has been reported that in a closed system using activated volumes for comparison that pressure has a measurable but insignificant effect on activation energy (Freund et al., 1993). In the same paper the authors admit that their result is different from that of two other researchers and that they cannot explain the discrepancy (Freund et al., 1993). Price and Wenger (1992), in contrast to the results by Fruend, "demonstrated that increasing pressure significantly retards all aspects of organic matter metamorphism, including hydrocarbon generation, maturation and thermal destruction."

2.2.4. <u>Particle Size</u>

Particles size should have little effect on intrinsic kinetics, but will affect mass transfer in larger particles. Many studies on the effect of particle size compare oil and gas yields from various particle sizes (Ekstrom and Callaghan, 1987; Dogan and Uysal, 1996; Ahmad and Williams, 1998; Torrente and Galan, 2001). There is some disagreement in the literature about the influence of particle size on oil yields and kinetic parameters. The results determined by various researchers fall into one of the three possible conclusions: increasing particle size lowers apparent activation energies, increasing particle size increases apparent activation energies, or particle size has no effect on apparent activation energies. One researcher who concluded that increasing particle size lowers apparent activation energies explains this conclusion by stating that the lower apparent activation energy is "perhaps reflecting increased porosity and surface area for the larger particles during the pyrolysis process." (Ahmad and Williams, 1998) The particle diameters considered by Ahmad are around 1 mm and show an increase in activation energy with size. The research contained in this dissertation will utilize particle sizes separated by three sieves to show whether or not the apparent activation energies are affected by mass transfer and thus demonstrate whether or not this range of particle sizes has an effect on activation energy. The three sieves were a 38 μm sieve, a 75 μm sieve, and a 150 μm sieve; therefore the size ranges were 0-38 μm, 38-75 μm, and 75-150 μm.

2.3. Chemical Reactivity Models

Researchers have modeled kerogen both with a representative physical model and a chemical structure-based predictive model. The first type of model represents a hypothetical compound that captures the chemical moieties and the bulk structures. The second type of model predicts how the compound will act chemically when subjected to some external stimulus such as heat (Charpenay et al., 1996). Because of variation among oil shale types these models are for a specific oil shale. The construction of these models generally includes data from various experiments including TGA, FTIR, elemental analysis, extraction, pyrolysis, oxidation, X-ray, and NMR (Charpenay et al., 1996; S. R. Kelemen, 2006; Freund et al., 2007). Each analytical technique adds new information that can be used to construct a working model of the kerogen.

Kerogen models are not the only organic macromolecule models. Coal has been modeled as well. One example of a coal devolatilization model developed by Fletcher and coworkers (Grant et al., 1989; Fletcher et al., 1990; Fletcher et al., 1992) is named the CPD model. This model predicts the devolatilization of the coal based on structural parameters such as those obtained from ^{13}C NMR. Because of the extensive existing work in coal, the theory developed for coal will be applied in part to kerogen. Decomposition models of kerogen pyrolysis are briefly reviewed here.

2.3.1. 1st Order

The first order model (Equation 2) is a very popular model for oil shale pyrolysis kinetics (Braun and Rothman, 1975; Campbell et al., 1978; Shih and Sohn, 1980; Burnham et al., 1983; Ahmad and Williams, 1998; Li and Yue, 2003; Abu-Qudais et al., 2005). The popularity of the model does not stem from a theoretical correctness but rather empirically it has performed well in describing global oil shale kinetics.

2.3.2. DAEM

The Distributed Activation Energy Model is seen as a series of reactions proceeding from those of lower activation energies to those of higher activation energies. A normal or Gaussian activation energy distribution can be modeled according to Equation 9

$$\frac{d}{d_{\max}} = \frac{1}{\sqrt{2\pi \cdot \sigma^2}} \int_{-\infty}^{E} \exp\left\{ -\frac{1}{2} \cdot \left(\frac{E - \overline{E}}{\sigma^2} \right)^2 \right\} dE \qquad (9)$$

where $\overline{E}$ is the mean activation energy, $d/d_{\max}$ is the ratio of the distributed variable to its maximum, and σ^2 is the variance. This model was used by Fletcher and coworkers in the development of the CPD model to describe the bridge-breaking and gas-release steps (Fletcher et al., 1989). Burnham (1991) used a Gaussian and a discrete activation energy model to describe the pyrolysis of oil shale. The distributed variable (activation energy) can be determined through an algorithm (Scott et al., 2006b) or tabulated (Fletcher et al., 1989).

2.4. Chemical Structure Work

2.4.1. Pyrolysis

Early work in kerogen pyrolysis looked at simplified mechanisms for decomposition describing reaction schemes like the one conceived by Franks and Goodier (1922) that kerogen is made of two components, an oil forming component and a coke forming component. As analytical techniques grew and progressed, so has the understanding of kerogen. Despite advances in analytical techniques, pyrolysis has remained a major tool in studying kerogen structure. One of the reasons for this is that there are very few analytical techniques to analyze macromolecules. Several techniques exist to convert the kerogen into smaller parts which can be analyzed by a broad range of analytical techniques. These techniques range from pyrolysis (Hubbard and Robinson, 1950) to oxidation (Boucher et al., 1991).

Pyrolysis works much like a sledge hammer or a big pair of molecular scissors to break the macromolecule into analyzable pieces, and as is pointed out by Yen, “it is thermodynamically impossible to synthesize by purely thermal means, long-chain alkanes from other hydrocarbon configurations” (Yen and Chilingarian, 1976). This means that the pieces were some how part of the original structure though Yen (1976) also points out according to some unpublished work that the structures found in the pyrolysate may not relate directly to the parent structure but rather are those structures that are thermodynamically stable components at the pyrolysis temperatures. Despite the possibility that the pyrolysate may not directly relate to the parent material, many researchers (many more than listed here) have used pyrolysis to generate fragments for study (Campbell et al., 1980; Van de Meent et al., 1980; Silbernagel et al., 1987; Chakravarty et al., 1988; Boucher et al., 1989; Ahmad and Williams, 1998; Avid et al., 2000; Ballice, 2002b, a, 2003; Freund et al., 2007). According to Durand (1980) there exists an analogy between pyrolysis and geological transformation of the kerogen. Both cases involve transformation in a non-oxidation environment and the transformation is principally due to temperature (Durand, 1980).

2.4.2. Mass Spectrometry

Mass spectrometry is a popular technique for kerogen analysis. Mass spectrometry is not suited for direct analysis of the kerogen but allows researchers to examine products from pyrolysis, oxidation, or chemical reactions. Huizinga and coworkers (1988) used pyrolysis mass spectrometry (py-ms) to look at the nature and distribution of products of kerogen pyrolysis.

Huizinga and coworkers performed pyrolysis experiments on an immature Green River sample from the Red Point mine in Piceance, Colorado. The experiment included pressures of 100 psi (6.8 Bar) of helium over a mixture of the sample and water. The sample was collected and analyzed in a mass specrometer. Huizinga found that the pyrolysis products included n-alkane/alkene pairs with a preference for odd carbon numbers. They also concluded that these pairs may have come from the degradation of ester-bound fatty acids and alcohols, respectively, but that C-C bond cleavage and free radical interactions could have also contributed (Huizinga et al., 1988). A chromatogram is shown in Figure 1 of their pyrolysate. The major peaks are pairs of alkanes/alkenes that vary by one carbon starting from the indicated n-C_{15} and range from ranges from C_7 to the upper C_{20}'s. The longer chains had an increasing retention time. Huizinga and coworkers (Huizinga et al., 1987a; 1987b) have also worked on analyzing the role of minerals on the production of hydrocarbons by using mass spectrometry. They mixed the kerogen with various minerals and reported the hydrocarbon yields.

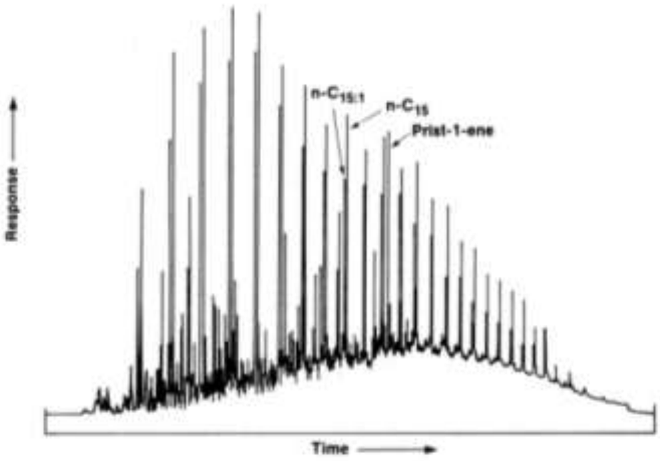

Figure 1. Chromatogram of pyrolysis products of Green River Kerogen adapted from Huizinga (1988).

Another method to use mass spectrometry is to perform an on-line detection of the pyrolysis products. This method was utilized by Reynolds and coworkers (1991) to analyze the gas evolution and species for pyrolysis conditions. This on-line detection method described by Reynolds and coworkers utilizes a triple-quadrupole mass spectrometer to separate the gas species and monitor for select species. This is necessary since multiple species will be generated simultaneously throughout the experiment. A sample of the results is shown in Figure 2 for several lighter hydrocarbons. The peak production of these lighter hydrocarbons is seen at around 465 °C. This temperature corresponds to near completion of pyrolysis at the heating rate used.

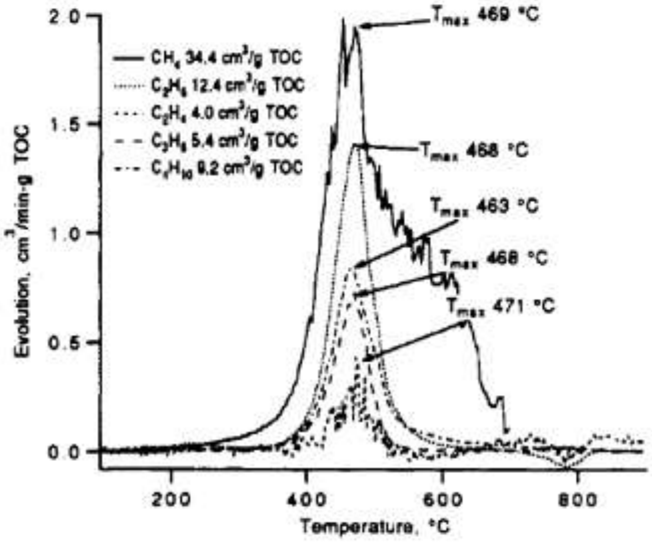

Figure 2. Hydrocarbon evolution for programmed temperature pyrolysis reproduced from Reynolds (1991).

2.4.3. Nuclear Magnetic Resonance Spectroscopy (NMR)

Nuclear magnetic resonance spectroscopy (herein referred to as NMR) is a technique that has seen increased use for solid state organic sample characterization in the past 30 years (Solum et al., 1989). One area that has made use of this analytical tool is in the characterization of large organic macromolecules such as coal. Because of the large size of organic macromolecules many analytical techniques cannot be applied. However, solid-state NMR does not need the sample to be broken apart for analysis, making it a valuable tool for macromolecule analysis. Thus, direct characterization of a macromolecule such as coal or kerogen can be accomplished through solid-state NMR.

Solum and coworkers (1989) used NMR to characterize the Argonne Premium Coals and utilized the 12 structural parameters directly measurable from NMR. These parameters are described here for convenience. f_a is the total fraction of aromatic, carboxyl and carbonyl carbons, which is subdivided into f_a^C, which represents the fraction of carbonyl and carboxyl carbons, and f_a', which represents the sp^2 hybridized carbons found in aromatic structures. The value of f_a' is further subdivided into protonated, f_a^H, and non-protonated, f_a^N, aromatic carbons. The non-protonated aromatic carbons are further split into f_a^P, f_a^S, and f_a^B, which are the fractions of phenolic, alkylated and bridgehead aromatic carbons, respectively. The fraction of aliphatic carbons is measured and represented as f_{al} The aliphatic carbons are divided into the fraction of CH and CH_2 groups, f_{al}^H, and the CH_3 groups which are represented as f_{al}^*. The aliphatic carbons that are bonded to oxygen, f_{al}^O, are also included. Once the NMR parameters are obtained along with the elemental compositions, several derived parameters can be determined such as the number of aromatic carbons per cluster and the molecular weight of clusters and side chains. These parameters are useful in models such as the CPD model constructed to describe the devolatization of coal (Fletcher et al., 1989). The use of NMR to characterize other organic macromolecules is often referenced to coal owing to the extensive literature available and the various similarities in their structure and chemical makeup (Knicker et al., 1996; Kelemen et al., 2002; Kelemen et al., 2007).

NMR has been used to investigate the structure of kerogen. Hagaman and coworkers (1984) used NMR to estimate potential oil yields from shales. They did so by utilizing f_{al} to determine aliphatic content. Hagaman and coworkers (1984) also found that throughout the mahogany zone (the zone of the highest oil per ton of rock) of a Green River oil shale that the aliphatic carbon fraction was nearly constant. Boucher (1989) utilized NMR and a complementary mild oxidation technique on a type II kerogen to demonstrate that,

"The NMR data revealed that the average molecular structure is mainly aliphatic (only 25.8% aromatic carbon) and contains predominantly CH_2 groups in rings or chains, or attached to oxygen. The aromatic species present are protonated (10%) ("benzene"-like), bridgehead or ring junction (8.1%) alkylated (5.8%) and phenolic (1.9%)".

This finding was used to challenge or contrast with a few of the then prevailing models for a type II kerogen. Because of the analytical power of NMR, techniques developed to describe coal (Solum et al., 1989) will be used to describe structural elements for the kerogens and some of the derivatives in this study.

2.4.4. X-Ray Photoelectron Spectroscopy (XPS)

X-Ray Photoelectron Spectroscopy (XPS) occupies a unique niche area in kerogen analysis. XPS is a surface scan technique that detects the shift in absorbance. Each element has a specific spectral range that depends on chemical bonds with other atoms. Even though XPS is a surface technique it is one of the few options for detecting types of heteroatom bonds within the sample. XPS is a relatively inexpensive method and is available in many laboratories, but requires curve fitting of often unresolved XPS scans (Kelemen et al., 2002).

Because of its unique capabilities, XPS has been used by Kelemen and coworkers (1999; 2002; 2007) to determine the types of nitrogen and oxygen bonds on different types of kerogens. Kelemen (1994) first determined the shifts for different model compounds and compared those to the Argonne Premium Coals. These model compounds are seen in Table 2 and show the range of XPS shifts expected for different types of nitrogen. Those shifts were applied to various kerogens as well based on the data from the model compounds. Specifically, Kelemen (2002) used the peaks that corresponded to the pyridinic, amines, pyrrolic, and quaternary types of nitrogen functionalities. The nitrogen curves were resolved using a full width half maximum of ~1.7 eV and a mixed Gaussian Lorenzian distribution curve.

Table 2. XPS nitrogen 1s shifts as determined by Kelemen (Kelemen et al., 1994)

Compound	Shift (Kelemen)	Type of N
phenazine	398.7	pyridinic
poly(2-vinyl pyridine)	398.8	pyridinic
3- hydroxypyridine	398.8	pyridinic
Norharman	398.9	pyridinic
PIB amine	399.1	amine
l-aminopyrene	399.3	amine
Norharman	400.1	Pyrrole
2- hydroxycarabazole	400.2	pyrrole
dibenzocarbazole	400.2	pyrrole
l-hydroxyquinoline	400.3	pyridone
l-methyl-4-pentadecyl 2(1H)-quinolone	400.4	pyridone
6-(2,2-diphenyl-2-hydroxylethyl)-2Z(H)-pyridone	400.5	pyridone
1-ethyl-4methoxypyridinum iodide	401.3	quaternary
pyridinium 3-nitrobenzenesulfonate (pyridinium)	401.4	quaternary
3-hydroxypyridine N-oxide	403	N-oxide
9- hydroxy-3-nitroflourene	405.3	nitro
pyridinium 3-nitrobenzenesulfonate (nitro)	405.8	nitro
l-nitropyrene	405.9	nitro

Similar results to those shown in Table 2 were published by Moulder and coworkers (1995) in the *Handbook of X-Ray Photoelectron Spectroscopy*. Moulder's spectral ranges for carbon are presented in Figure 3, the results for nitrogen are presented in Figure 4, and the results for oxygen are presented in Figure 5. Notice how in the oxygen region there are broad ranges for the various shifts and little separation for the different oxygen carbon bonds. This is why Kelemen used the effect of oxygen on carbon to determine the forms of oxygen in the samples.

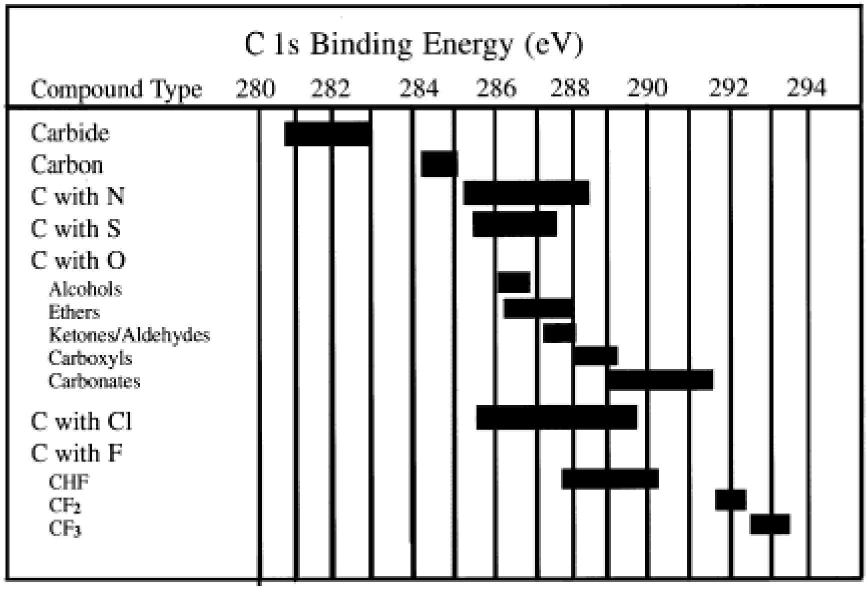

Figure 3. XPS Carbon 1s shifts for various hetero atom configurations. Adapted from Moulder et al. (1995).

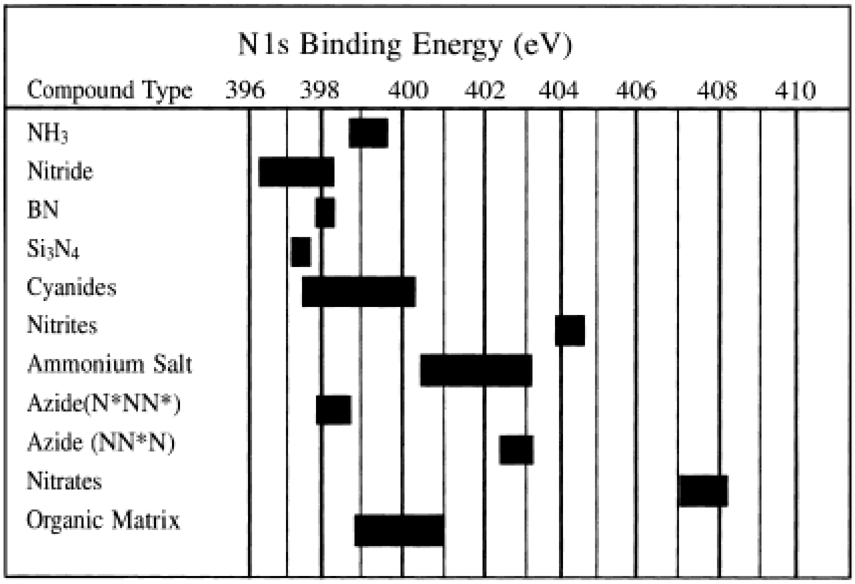

Figure 4. XPS Nitrogen shifts for various nitrogen configurations. Adapted from Moulder et al. (1995).

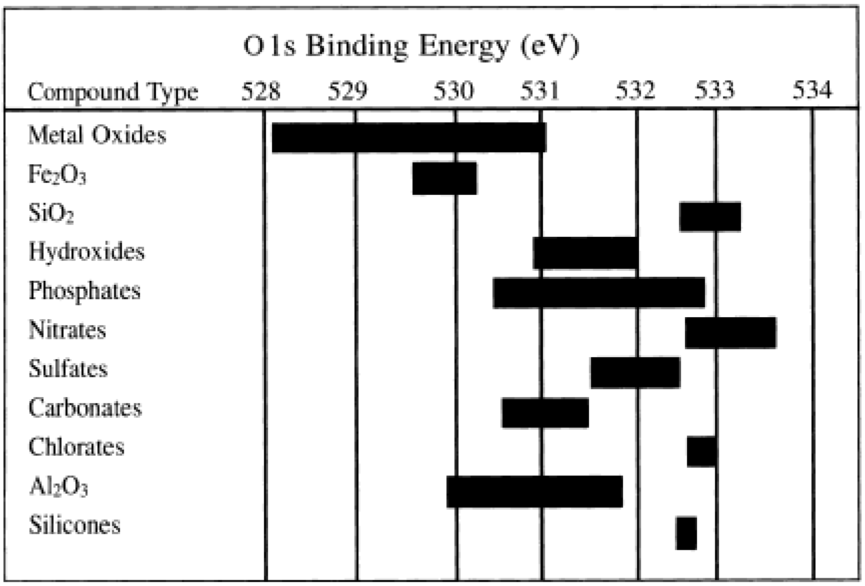

Figure 5. XPS oxygen shifts for various oxygen configurations. Adapted from Moulder et al. (1995).

2.4.5. Structural Models

Structural models for kerogen provide a way to view the chemical features of kerogen but are limited by the size of the model and the amount of experimental data available to construct the model. Structurally kerogen can be seen as a complex polymer that is bound (or in some manner associated) to a mineral matrix. This polymer view has been the basis for generating models of kerogen such as the Schmidt-Collerus Kerogen Structure in Figure 6 (Schmidt-Collerus and Prien, 1974). Here the K's represent connections to other kerogen subunits.

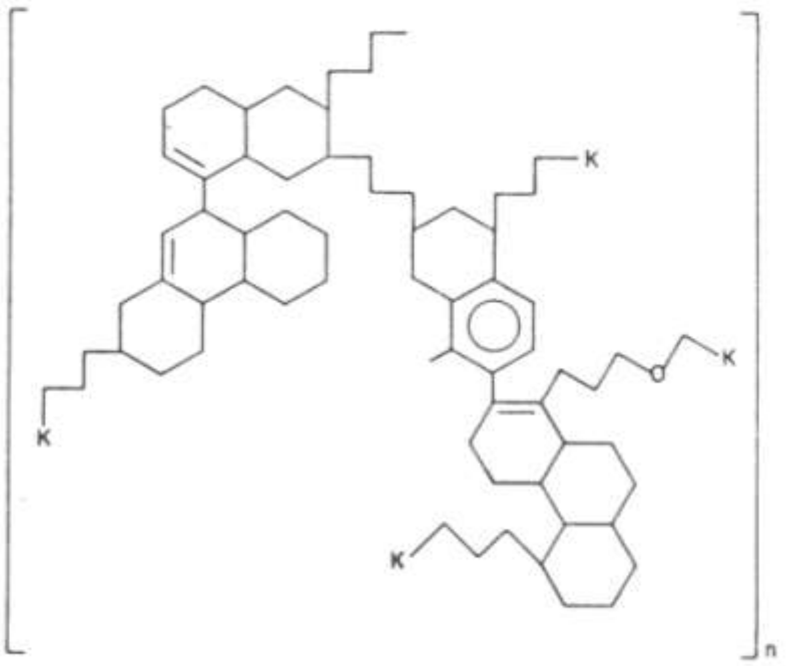

Figure 6. Schmidt-Collerus kerogen sub unit structure from the Green River formation (1974).

The Schmidt-Collerus kerogen sub-structure is a simplified polymer like structure with one oxygen atom and no other hetero-atoms. This sub-structure is part of a larger model that shows the subunits connected by aliphatic chains to other subunits as well as other types of subunits (Schmidt-Collerus and Prien, 1974). This larger model is a “stick figure” model shown in Figure 7 and has been reproduced from Science and Technology of Oil Shale by Yen (1976). “Stick figure” models do not show explicit chemical structures but rather use sticks and boxes to represent general structures.

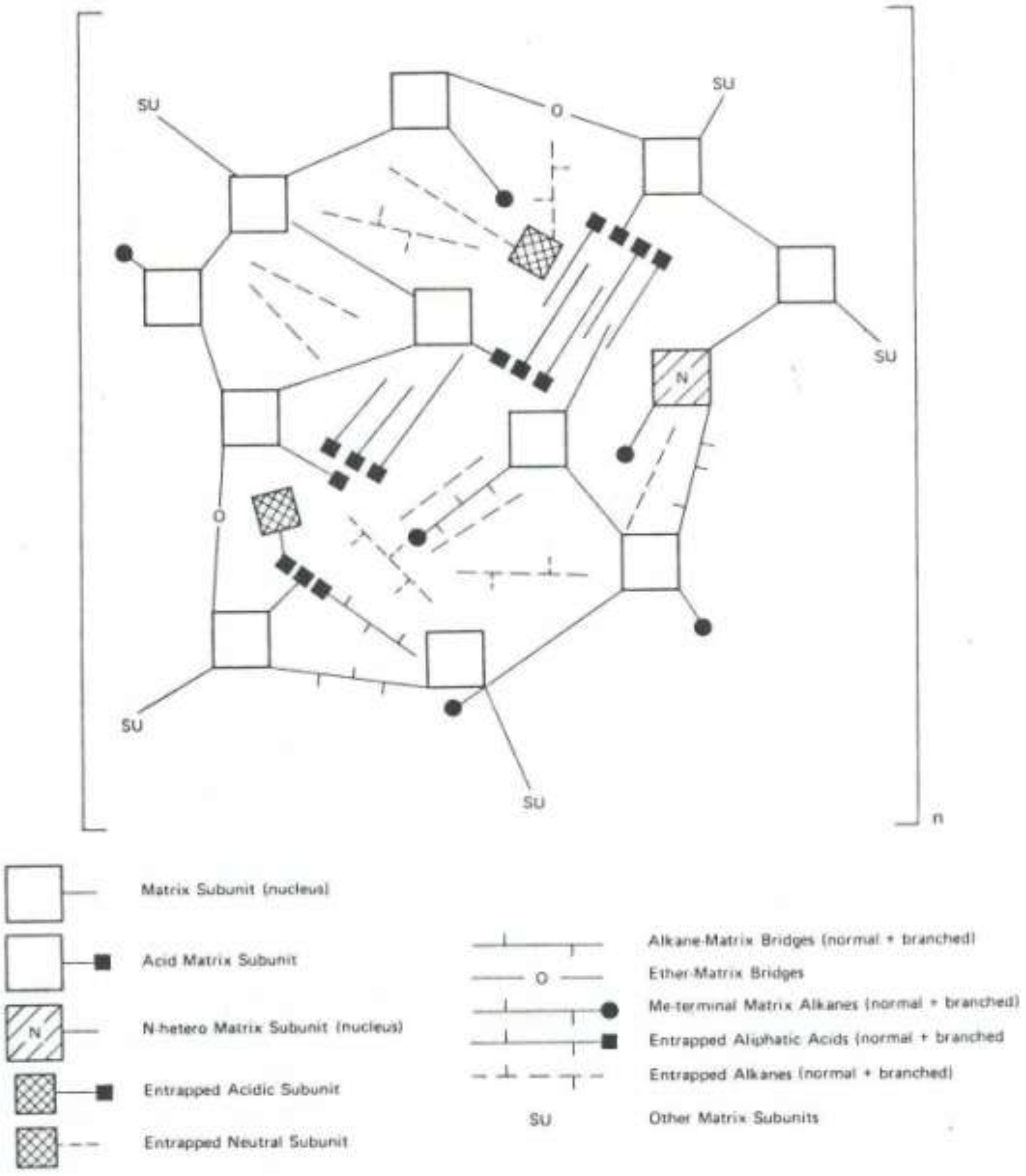

Figure 7. Schmidt-Collerus and Prien kerogen matrix model (1974).

Other "stick figure" models such as the one seen in Figure 8 show a hypothetical structure with the essential components (Yen and Chilingarian, 1976)

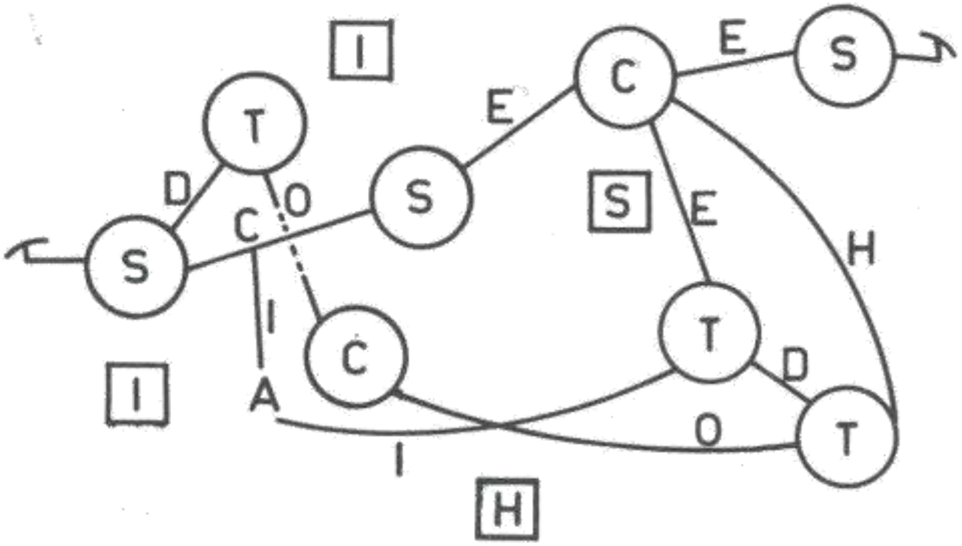

Hypothetical structural model of a multipolymer representing the organic component of Green River oil shale [236]. The circles represent essential components of kerogen; the squares represent molecules trapped in the kerogen network.

I. isoprenoids. **S.** steroids. **T.** terpenoids. **C.** carotenoids. **D.** disulfide. **O.** ether. **E.** ester. **H.** heterocyclic. **A.** alkadiene.

Figure 8. Model by Yen (Yen and Chilingarian, 1976) and reproduced here from figure 10.6 in *Kerogen (Durand, 1980)*.

Other models chose to leave the bulk kerogen represented by subunits but focus on more detailed functional groups and side chains. Figure 9 is one such model.

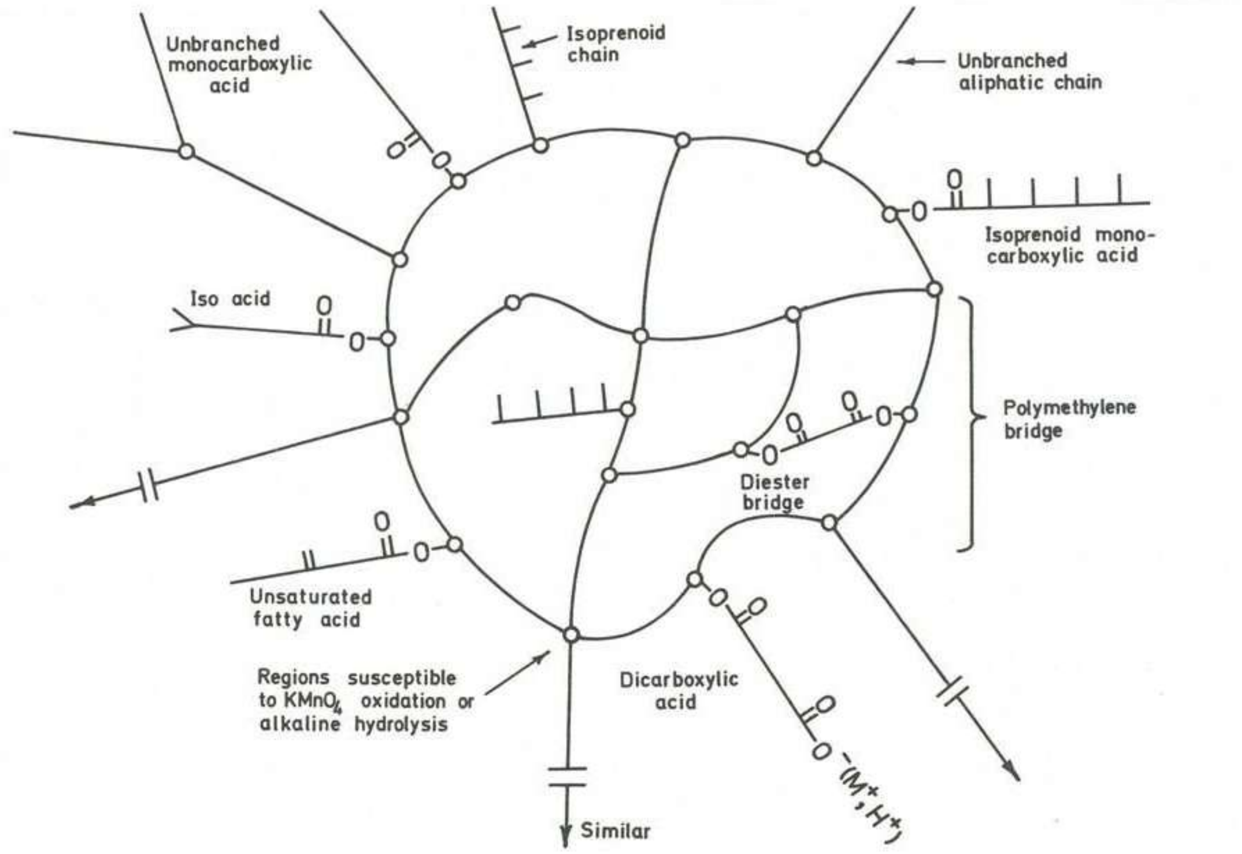

Figure 9. Green River oil shale subunit (Djuricic et al., 1971).

Note how in Figure 9 the authors neither attempt to describe the distribution of side chain lengths nor any specific features other than the functional groups. A similar model by Burlingame et al. (1968) to that presented in Figure 9 does not have the bulk kerogen represented except as a region but similarly has the functional groups displayed attached to the bulk, as seen in Figure 10.

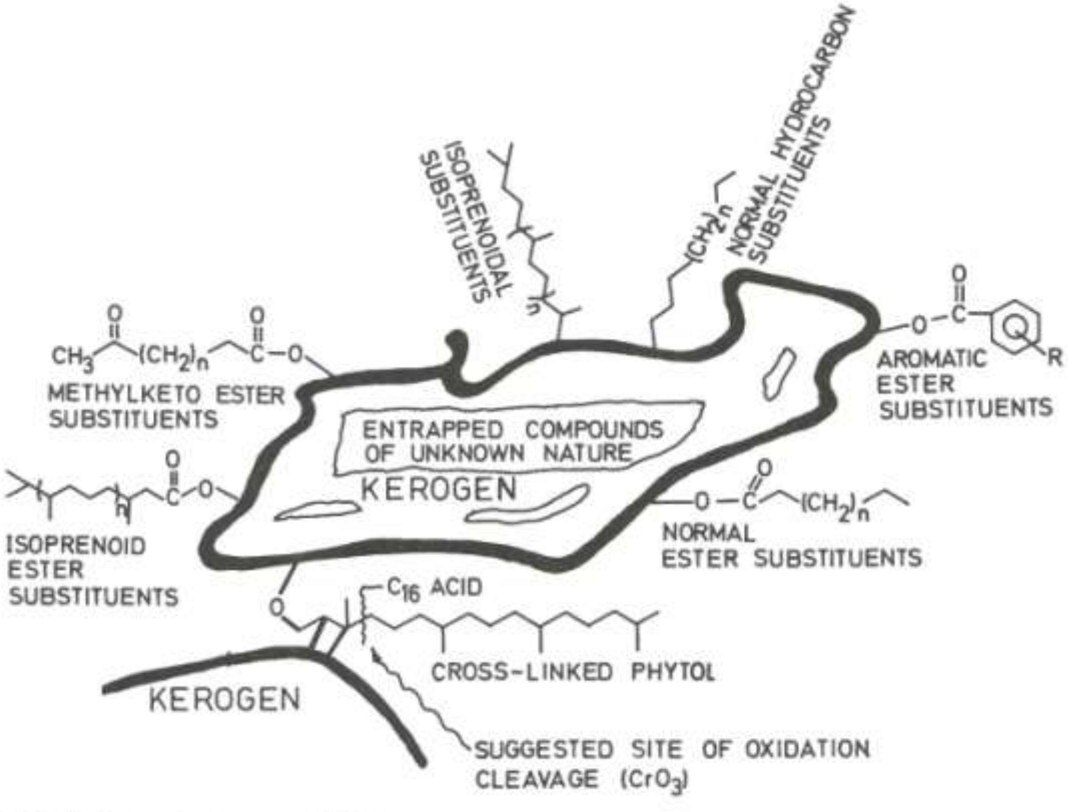

Fig. 22. The substituent structure suggested for kerogen.

Figure 10. Burlingame model (Burlingame et al., 1968) of Kerogen reprinted from Durand (1980) .

More complex models have been proposed ranging from a model that fits nicely on a page and shows a distribution of side chains and other features such as the Siskin model (Siskin et al., 1995) to models containing tens of thousands of atoms in the kerogen matrix such as the model of a wide range of kerogen types reported by Kelemen and coworkers (2007). The Siskin model shown in Figure 11 has a distribution of heteroatoms, side chain and bridge lengths, aromatic core structures, and free floating molecules.

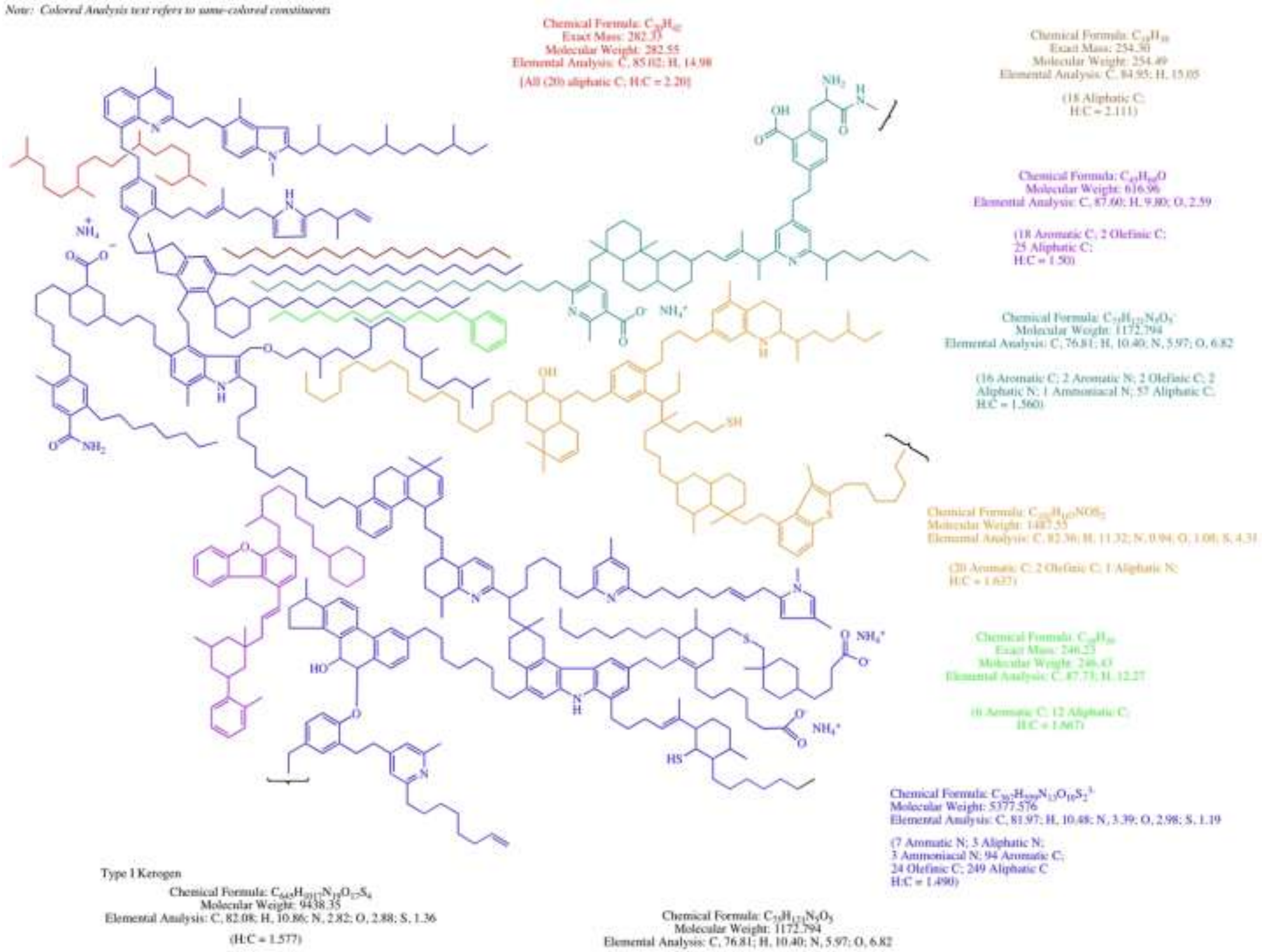

Figure 11. Siskin Model of Green River Oil Shale (1995).

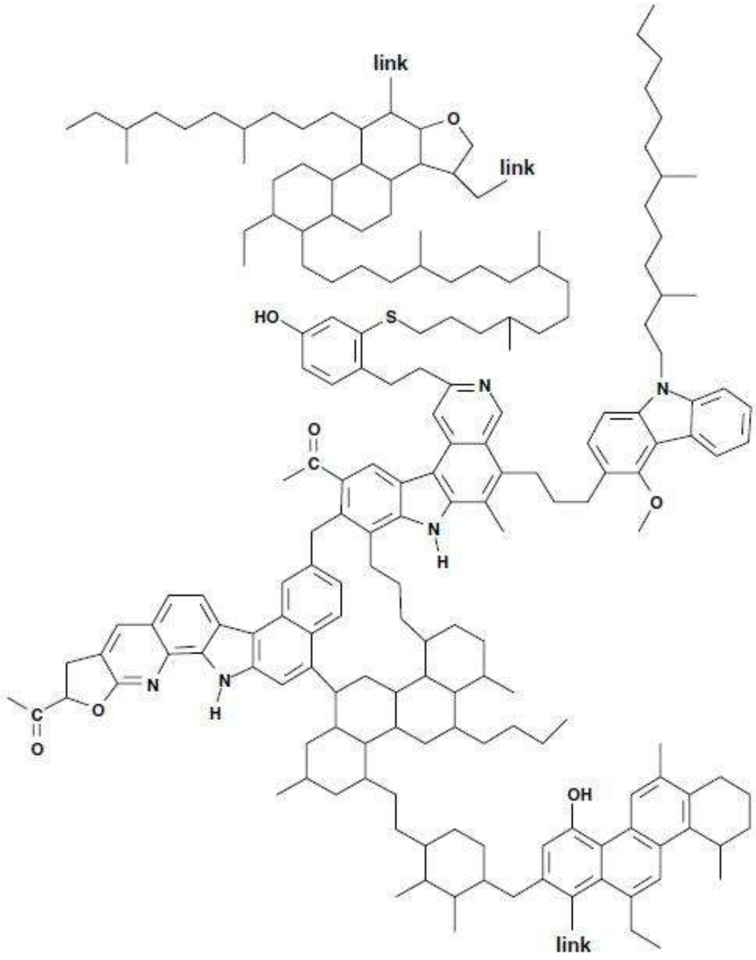

Figure 12. 8 of 10,000 Cores in the Kelemen Model illustrating the varying ring sizes, chain lengths, and heteratom configurations of a type I kerogen (Freund et al., 2007).

The Fruend model shown in Figure 12 is a snap shot of a small fraction of their model. They define a core as an aromatic/aliphatic ring cluster. The model shown in Figure 12 is 8 cores of a 10,000 core model. The model is built by allowing a computer to assemble the model based upon statistical distribution of structures and atoms such as types of nitrogen (pyridinic, pyrolic, and quaternary). As computing power and analytical techniques have grown, additional complexity has been added with subsequent models until they no longer fit conveniently on a page (Freund et al., 2007). All of the previously discussed models are 2-D; one area of future research will be to create a 3-D model that can help researchers determine the pore structure and migration of molecules within that structure. It is not within the scope of this dissertation to create a complete chemical model, but the research presented herein can be used either to validate existing models or to create a more sophisticated model.

2.5. Summary

There has been tremendous amount of work put into unlocking the secrets of oil shale and kerogen. This work began as early as the late 1800's and has continued to today with much of this work performed prior to 1995. One area that has had many studies is in the pyrolysis kinetics of oil shales. A survey of the literature reveals that the methods used to determine the parameters generally make some simplifying assumptions that have become generally accepted but are not strictly correct. The literature shows almost no statistical work on the confidence regions surrounding the kinetic parameters of oil shale. Likewise conflicting research is found about the effects of extent of extraction and the effects of pressure on activation energy, and hence more research is needed in these areas.

Chemical structural modeling is limited by the availability of analytical chemistry techniques and computing power. As more analytical chemistry techniques become available and as computing power increases there will be more complex models constructed. There is an ever increasing need for additional analytical chemistry results to guide the construction of these models and to verify the existing literature results. These models will assist researchers in understanding the oil shale resource and methods of recovering that resource for the good of human kind.

3. **Objectives**

One objective of this work was to develop a model of kerogen pyrolysis capable of predicting temperature and heating rate effects on mass release. This work utilized TGA equipment coupled with mass spectrometry, NMR, and other chemical analytical methods to conduct pyrolysis experiments performed at different heating rates. Experiments in this work were designed to measure pressure effects on the pyrolysis of specific oil shales. During the course of this project it became necessary to develop a method to analyze the non-isothermal TGA data with non-linear regression to obtain reaction rate coefficients. A secondary objective was to measure the effect of the mineral matrix on the kinetic parameters describing oil shale pyrolysis. The experiments on the effects of mineral matter were performed on kerogen samples that were produced at various stages of demineralization. A third objective was to collect chemical structure data on kerogen. Mass spectrometry and NMR spectroscopy were used to determine the nature of the pyrolysis products produced in the pyrolysis experiments. The data collected were provided to a third party for use in developing a chemical structure model. Specific tasks are listed below.

3.1. Tasks

Task 1. Measurement of Pyrolysis Data

a. Reconstruct the high pressure TGA (Thermogravimetric Analysis) facility at Brigham Young University.

b. Collect TGA pyrolysis data on two oil shales and one demineralized sample.

Task 2. Kinetic Modeling

a. Develop a non-linear method to regress 1st order (or higher order model) kinetic parameters.

b. Identify whether pressure affects the first order kinetic parameters determined from task 2a for the decomposition of the samples.

c. Identify how (or if) the stage of demineralization affects the kinetic parameters for the decomposition of the shale.

d. Evaluate the use of a Distributed Activation Energy Model (DAEM) for Oil Shale Pyrolysis and Compare with 1st Order Model.

Task 3. Determination of an Approximate Green River Oil Shale Chemical Structure

a. Use mass spectrometery, NMR, and other chemical analyses in conjunction with pyrolysis to determine structural aspects of oil shale for samples provided on this project.

b. Repair a donated mass spectrometer and use it to look at lighter decomposition products from the effluent of the TGA and a similar pyrolysis reactor developed as part of this project.

c. Identify how the structure of the shale changes as it decomposes.

d. Propose chemical structural aspects that need to be present in a model of the organic material in the shale.

3.2. Approach

Task 1. Pyrolysis Experiments

Task 1a. Reconstruct the high pressure Thermo Gravimetric Analysis facility at Brigham Young University

The high pressure TGA facility at Brigham Young University shown in Figure 13 on page 44 was purchased in the early 1990s and was described by Clayton (2002). This TGA is capable of pressures up to 100 bar and internal temperatures of about 1200 K. This TGA was designed to perform pyrolysis experiments in an inert atmosphere, oxidation experiments, and gasification experiments. The TGA could be temperature programmed to allow for combinations of linear heating rates and isothermal experiments. This facility functioned well until a few years ago when the controlling computer failed. Attempts to contact the original equipment manufacturer revealed that the TGA portion of the company had been closed and that the company could not assist in the repair of the equipment. The first task for the project was to replace the old computer control system (the interface of which was written in German) with a new English-based modern control system. A Labview© system by National Instruments was selected because of its ease of use, cost (the University already has a license), and availability of support.

Task 1b. Collect TGA data on oil shale samples and demineralized samples

The project included looking at both raw oil shale and the kerogen at various stages of demineralization. The assumption was that the demineralization process would not significantly affect the organic structure. The only affected portion of the organic matter was assumed to be the bonding to the mineral matrix. Therefore, when pyrolyzing the demineralized sample, slightly lower activation energies might be observed, proportional to the strength of the interactions with the mineral matrix. The demineralization process for the A-3 and A-7 samples were carried out by a research team directed by Dr. Ron Pugmire of the University of Utah. A previous demineralization process was documented by Winans and coworkers (Vandegrift et al., 1980) and sample GRK-W is from that procedure. A similar process based on toluene instead of benzene was developed by the team at the University of Utah. Table 3 contains a description and name for the samples used in this work.

Table 3. Sample naming convention for samples used in this study.

Names	Descriptions
A-0	Raw Shale
A-3	3rd Stage of Demineralization of the A-0 sample
A-7	7th Stage of Demineralization of the A-0 sample
R-150	Samples of a Second Raw Shale that are between 75μm and 150 μm
R-75	Samples of a Second Raw Shale that are between 38μm and 75 μm
R-38	Samples of a Second Raw Shale that are smaller than 38μm
A-0.1600	Raw Shale same as A-0 sample from 1600μm to 800μm
A-7.PRO	Professionally demineralized sample A
M-OC	Out Crop Sample Used in preliminary research
GRK-W	Demineralized Kerogen provided by Randy Winans for preliminary research

Low heating rates were used in the TGA so that mass transfer effects did not obscure the intrinsic kinetic data. A series of experiments was performed using a wide range of heating rates (1 to 60 K/min) to determine heating rates where mass transfer effects became important.

Task 2. First-Order Modeling

Task 2a. Develop a non-linear method to regress kinetic parameters

Traditional kinetic data are collected isothermally and a plot of ln k vs. 1/T is constructed. Several experiments at different temperatures conditions are conducted. The kinetic equations are then linearized, and activation energies are determined from a linear fit of the data. Isothermal experiments assume a constant temperature throughout the reaction period and neglect any reactions that occur during the heat up period. However, pyrolysis reactions generally occur during the heating period, so that a non-isothermal approach is a better suited analysis technique. Once the data are obtained there are several methods to regress kinetic parameters, but most traditional methods involve linearized forms of the solution to Equation 2. The more common methods can be classified as approximate integral methods or the derivative method. The integral methods are approximations because there is no analytical solution to Equation 6.

At least four motivations exist to introduce a new method for data regression: (1), the somewhat arbitrary decision as to what points to include in the traditional analysis; (2), the errors associated with linearizing an equation; (3), the problems that arise from extrapolating to determine the natural log of the pre-exponential factor; and (4), linear methods were developed for computational ease which with the advent of computers is no longer necessary. A new method was proposed for this task that numerically calculates a solution to Equation 6 and couples it with Equation 2 to solve for the kinetic parameters and avoids the aforementioned problems. Non-linear statistics based upon the F-statistic were used to provide a confidence region for the parameters.

Task 2b. Identify whether pressure affects the first order kinetic parameters determined from task 2a for the decomposition of the samples

The method for regression of kinetic parameters determined in Task 2a was used to determine the change in activation energy as a result of pressure. These experiments included both oil shale and demineralized organic matter. The pressure effects might be due to a vapor-liquid-gas equilibrium process or some change in the reaction mechanism. It was not the explicit goal of this task to determine the change of mechanism due to pressure, but rather this goal was to demonstrate whether or not pressure had an effect on the kinetic parameters for the oil shales in this study. The conditions selected for the experiment were representative of a sample under pressure from the overburden of rock at *in-situ* conditions. The pressure used in this task was 40 bar.

Task 2c. Identify how (or if) the stage of demineralization affects the kinetic parameters for the decomposition of the shale

The method for regression of kinetic parameters determined in Task 2a was used to determine the change in activation energy between oil shale and the demineralized organic matter. This information was used to determine the strength of the interaction between the organic matter and the mineral matrix. It was initially hypothesized that the activation energy would decrease for the extracted organic matter because the bond between the mineral matrix and the organic matter would not be present.

Task 2d. Advanced Modeling – Evaluate the use of a Distributed Activation Energy Model (DAEM) for Oil Shale Pyrolysis and Compare with a 1st Order Model

The first order model from Task 2 is sufficient for a global engineering standpoint but a more sophisticated model will describe the kinetics better. This task was to combine the regression method previously outlined with the Distributed Activation Energy Model (DAEM) instead of that derived from Equation 2. The approach to the DAEM used in this work was a sequential set of reactions rather than the commonly used parallel approach. This sequential approach is an approximation similar to that of the CPD model. This task required modification to the code written to accomplish Task 2. In the limit as the distribution value, σ, approaches zero the DAEM collapses into the 1st order model.

Task 3. Determine necessary Green River oil shale chemical structure elements

Task 3a. Use mass spectrometer, NMR spectroscopy, and other chemical analyses in conjunction with pyrolysis to determine structural aspects of oil shale for samples provided on this project

An understanding of the chemical structure is important to modeling the decomposition of oil shale. This work used mass spectroscopy to analyze the decomposition products and NMR spectroscopy to determine aspects of the chemical structure. XPS is another chemical technique that can provide information about the sample. XPS analysis was used to determine the type and relative abundance of nitrogen and oxygen compounds in the kerogen, and what forms were left after pyrolysis. FTIR was also used to analyze pyrolysis products. The chemical structure information was then provided to a group assembled by industry for use in chemical structural modeling.

Task 3b. Repair a donated mass spectrometer and use it to look at lighter decomposition products from the effluent of the TGA or other pyrolysis reactor

This project included using several analytical chemistry techniques as explained in Task 3a. One of these techniques includes a donated mass spectrometer that was in need of repair. The repairs were partially accomplished through a third party technician. Once the equipment was repaired it was used (along with another similar facility) to look at the gaseous and condensable decomposition products. The gaseous products were collected and analyzed by one of three methods. The first method was to perform on-line analysis of the gases. This required a self-constructed interface from the TGA to the mass spectrometer. The difficulty was that the TGA operated at pressures from 1 bar to 100 bar while the mass spectrometer operated at high vacuum. It was shown that the effluent from the TGA could be split and a portion passed through a capillary tube to the mass spectrometer. The capillary tube provided enough pressure drop so as not to overload the turbo pumps on the mass spectrometer. The mass spectrometer was a TSQ 7000 mass spectrometer made by Thermo-Fischer, with a triple quadrapole unit with a m/z range from 10-4000. The mass spectrometer was connected to a Varian 3400 gas chromatograph (GC).

The second method was to collect the entire gas effluent for a period of an experiment in a special gas collection bag. A sample was then drawn from that bag to use in analysis in the FTIR. This method may have had some atmospheric contamination of the sample. There were difficulties in ensuring that the portion of the effluent was a representative sample of the products.

Task 3c. Identify how the structural aspects of the shale change as it decomposes

Task 3c was to conduct experiments to determine the structure of the organic matrix. One experiment was to heat a sample in an inert atmosphere at a constant heating rate using a pyrolysis reactor (detailed in section 4.1.3) and analyze the products. Because the mass trace vs temperature was already known from previous TGA experiments the sample in this reactor was heated to a given extent of conversion and then removed from the heat. The light gases were sampled just prior to the removal from the heat and analyzed in a mass spectrometer in Task 3b while the generated chars and/or tars were analyzed by techniques such as NMR and XPS. These experiments were carried out at 20%, 40%, 50%, 60%, 80%, and 100% conversion. The tar analysis was conducted by collecting the tar in a cold trap and then making a solution to be analyzed in the mass spectrometer.

Task 3d. Propose chemical structural aspects that need to be present in a model of the organic material in the shale provided for this project

The organic matter in oil shale is dependent on the shale being studied. Despite the diversity of the organic matter there are some common traits throughout a formation allowing for chemically accurate estimations of the kerogen. These estimations or models attempt to represent the chemical moieties and other traits such as aliphatic vs. aromatic carbons. These approximations are common for coal, and several researchers have also constructed specific models of oil shale for various formations world wide. At the present time there is some uncertainty whether the Siskin model, shown in Figure 11, is an acceptable representation of the samples of this project. This work will contribute to a larger model using NMR data and other data collected in task 3a.

4. **Experimental**

4.1. Equipment Descriptions

This section details the various experimental apparatuses and techniques used in this work. Section 4.1 describes each piece of equipment and section 4.2 describes the specific methods and techniques used in this work. A few of these experimental setups and methods were developed for this project and a few are direct use or adaptations of methods commonly used. This section also details the new control system installed in the high-pressure thermogravimetric analyzer.

4.1.1. Thermogravimetric Analyzer (TGA)

The oil shale pyrolysis data for the kinetic parameter analysis were acquired in a Deutsche Montan Technologie (DMT) high-pressure thermogravimetric analyzer (HPTGA) rated to a maximum pressure of 100 bar and maximum reactor temperature of 1100°C. The maximum reported achievable heating rate is 100K/min (Clayton, 2002). Pressures in the reaction vessel are achieved via a constant flow rate of gas into the reactor and a pressure valve on the outlet. Pressure is controlled to an accuracy of ±0.5% at 40 bars.

The TGA is electrically heated which allows for good control of the temperature. Temperature ramp rates of 10K/min are achieved with an R^2 value of 0.999999 if a graph of the temperature vs time is fitted with the slope being equal to 10.0 K/min. The flow rates are maintained via three mass flow controllers that have ranges of 0.1 to 10 L/min. One flow meter maintains a purge on the micro balance while the two other controllers mix flows upstream of the reactor allowing for mixed gas flows to be used as a reacting atmosphere.

The physical portion of the equipment has been described in detail in a dissertation by Clayton (2002) and a schematic of the apparatus from that work is shown in Figure 13.

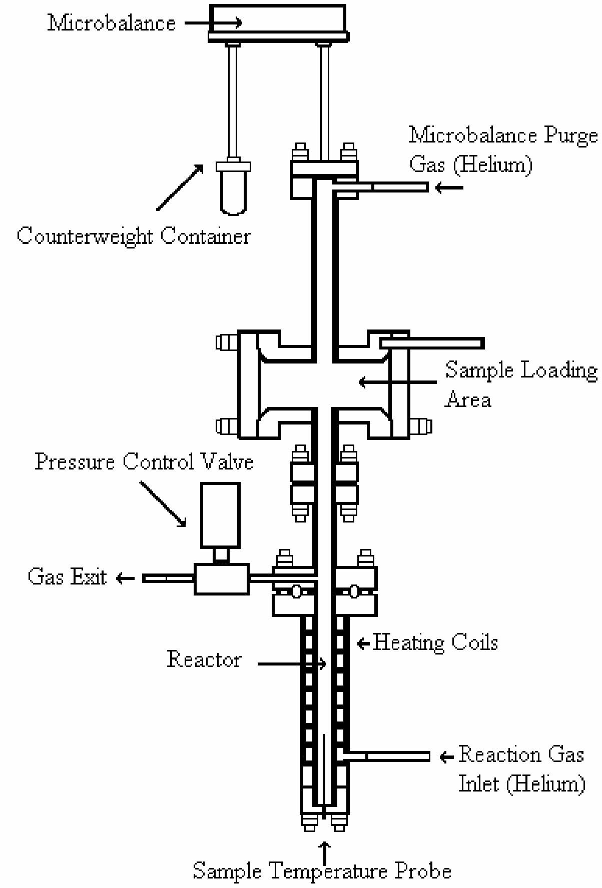

Figure 13. Schematic of the TGA Picture from Clayton (2002).

The original data acquisition system had to be replaced because of control equipment failures prior to any collection of data for this project. The archaic system was designed and implemented by DMT and included the standard component communication CAN-BUS at the time of equipment manufacture (the early 1990's). The computer program that controlled the equipment and recorded the data was primarily written in German and required translation to navigate the features. This system functioned well enough for about a decade until an integral controller card with a programmed logic chip failed. The original equipment manufacturer revealed that no possible support could be obtained. The decision was made to replace the entire control system with a new system. The new control system chosen was driven by the Labview® software, a product of National Instruments. The resulting system is compatible with current computing hardware and software and the source code is available for future modifications as necessary.

The new system was based upon the National Instruments SCXI system. In this system the data acquisition and control were accomplished by a connection between a computer and a control chassis. This chassis contained slots for up to four modules. The specific chassis used was a SCXI-1000 with SCXI-1112 to read the thermocouples, a SCXI-1161 to control the switching of relays, and two SCXI-1302 used in conjunction with SCXI-1180 units to read and control the analog signals in the system. Two SCXI-1302 units were needed because only two analog out channels were available per unit and three channels were needed for the three flow meters. The switching of power to the heaters provided a challenge because of the high voltage required for the heaters. Another difficult challenge was that the pressure valve was controlled by two relays. When relay A is on, the valve opens, and when relay B is on the valve closes. If both are off then it stays steady and if both are on then the valve cycles between full open and full close. The valve also presented a difficulty in that it required 30 seconds to open completely from a completely closed position. Finally the valve had a return signal to indicate percentage open. Using this signal and modified PID controller the new system was capable of pressure control within 1% of the set point.

The control of the heaters necessitated a second relay used in conjunction with the National Instruments relay system. This second relay handles the high voltage (208 V) and high currents required to power the heaters. Because of the nature of the heaters, control was a straight forward PID control with parameters similar to those used in the original system. The new equipment controller allowed for better control, more flexibility, and the software interface was in English.

4.1.2. Oil Shale Retort

A benchtop oil shale retort was used because of its increased sample load capacity compared to the TGA. This retort had a batch capacity of approximately 1 kilogram. The retort was heated by a clam shell heater while the retort was rotated for heat transfer purposes. The gases and tars were passed through a filter while still hot to remove dust from attrition of the sample. The tars were removed in a single stage condenser immersed in an ice water bath. Because of pressure drop in the system, the reactor was at 2 psi gauge. Pressure was maintained around 2 psig for the duration of the test by manual adjustment of a vacuum downstream of the system. Figure 14 shows a schematic of the bench top oil shale retort used. For reference, the reactor length was about 30 cm.

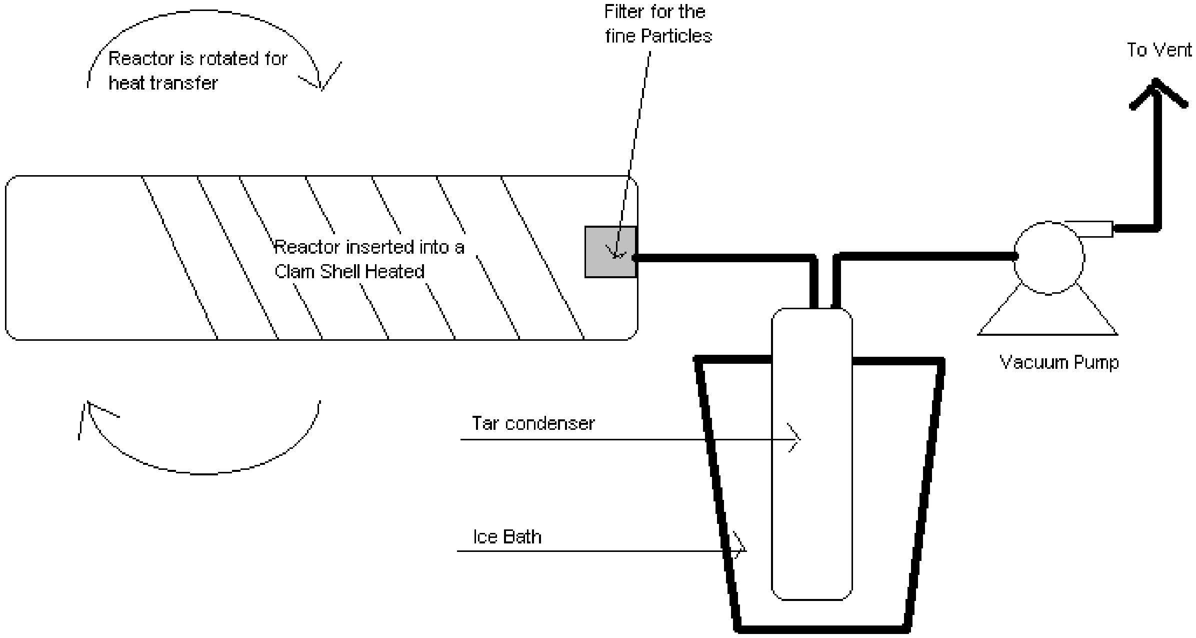

Figure 14. Oil shale retort schematic.

4.1.3. Kerogen Retort

A separate reactor was built to collect char and tar data from kerogen and will be herein referred to as the Kerogen Retort. A schematic of this retort can be seen in Figure 15.

The construction of the kerogen retort was necessary because the capacity of the TGA was insufficient to measure gas species and tar yields and the minimum required sample for the Oil Shale retort described in section 4.1.2 exceeded available sample. The kerogen retort was designed to mimic conditions found in the TGA experiments. The retort was made from ¾ in. stainless steel tubing bent into a U-like shape as seen in Figure 15.

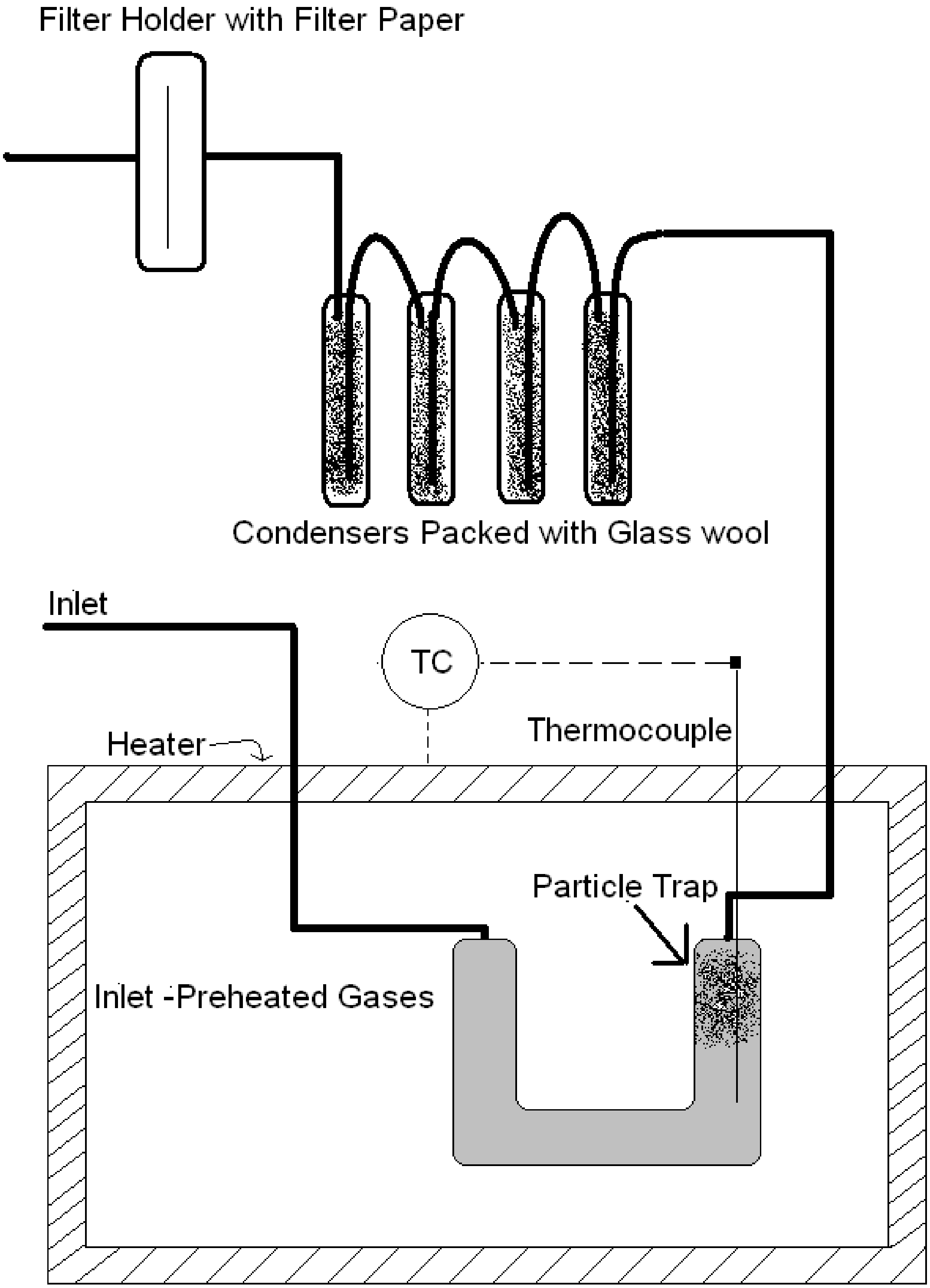

Figure 15. Schematic of the kerogen retort used for generating chars and tars.

The inlet was 3 ft of ¼ in. copper tubing wrapped in a coil inside the heater and additional tubing outside of the heater connected to a gas source. The inlet tubing inside of the heater served to preheat the gases. The outlet of the heater was designed to allow for thermocouple access and was made of ¼ in. stainless steel tubing. The kerogen particles were very light and easily entrained in the gas, so a glass wool plug was included in the outlet region of the reactor to prevent particles from becoming entrained and traveling into the condensers, while allowing the tars and other gases to freely travel down stream out of the furnace. The condensers were constructed by packing a fine glass wool into a test tube and using a rubber stopper to close the top. The cork had two holes drilled into it through which ¼ in. stainless steel tubing was tightly fitted. The inlet to each condenser was long enough to reach the bottom while the outlet was short. The gases entered and passed through the glass wool before exiting. The four condensers were immersed in a cooling bath to aid condensation. By cooling the condensers the tars collect on the glass wool and were easily extracted via a dichloromethane wash. A filter holder with filter paper was included down stream of the condensers to verify that tars did not travel down stream. The filter turned brown in experiments where improper packing or insufficient packing of the glass wool. Generally the exit gases were vented into a fume hood ventilation system, though in some experiments the outlet gases were directed into a collection bag for gas analysis.

4.1.4. XPS

X-ray photoelectron spectroscopy (XPS) experiments were performed courtesy of the BYU chemistry department on a Surface Science SSX-100 instrument with a monochromatized Al Kα source and a hemispherical analyzer.

4.1.5. GC/MS

The GC/MS equipment was acquired as a donation from the Chevron-Texaco corporation. The GC/MS was not in working order when it arrived at BYU. As part of Task 3b the GC/MS was fixed with the help of a local instrument repair technician, and operational procedures were developed. The MS was a TSQ 7000 manufactured by Finnigan (now Thermo Finnigan) sometime in the 1990's. This particular model of mass spectrometer was a triple quadrapole unit and was capable of various inputs and ionization methods. The unit was configured to use an electron ionization source and a single mass selector with the other quadrapoles operated to pass the masses to the source. The unit was damaged during a power surge some 5 years prior to donation and had not been used since that time. The main problem was a vacuum control board but there were numerous other small problems and leaks that had to be remedied before the unit was operational.

The inlet for most experiments was a Varian 3400 CX gas chromatograph (GC). This gas chromatograph was capable of cooling columns via liquid nitrogen but those capabilities were not utilized for these experiments. The GC was operated in splitless injection mode utilizing a DB-1 microbore column manufactured by J&W scientific. The column was a DB-1, 20 meter, 0.1 mm I.D. microbore, and had a 0.4 micron film. The column's operating temperature range was from -60°C to 325°C. This column was designed for hydrocarbons.

The GC/MS was controlled by a DEC work station (Unix). One of the problems that had to be overcome was that when the unit arrived it was discovered that nobody at Chevron-Texaco knew the password to the system. A new windows based control system was cost prohibitive and therefore some basic computer hacking skills were learned and employed to discover and reset the password. The Unix based computers were a restrictive factor in the experiments since storage space was limited and the only method to get data off the machines was to burn a CD. The software to interpret the data files was only available on the Unix computers. Once the data were burned to a CD, manual analysis of the data was required. Therefore analysis was performed prior to transferring the data to the CD.

4.1.6. FTIR

The FTIR machine was a Bomem® MB-155 FTIR equipped with a 10 m multi-pass gas cell (Infrared Analysis, Inc). The IR beam source was a Globar IR source. All the spectra were acquired with a resolution of 1 cm^{-1} and a spectral range of 400-4000 cm^{-1} though they are presented with narrower ranges. This piece of equipment was described by Haifeng Zhang in his PhD dissertation (Zhang, 2001). Zhang included a description of the equipment, diagrams, mechanics of operation, and a complete description of the multi-pass gas cell. The detector is liquid N_2-cooled and the detection limit of the FTIR was as low as 50 PPB for certain types of gases (including NH_3, C_2H_4 and C_2H_2) (Zhang, 2001). The detection limits for other gases are generally about 100 PPB.

4.1.7. Low Temperature Ashing

Ashing and moisture tests were accomplished in an electrically-heated furnace. This furnace was capable of alternating constant heating rate and constant temperatures.

4.1.8. CHNS

Elemental analysis was performed using a Leco TruSpec® Micro CHNS machine. This machine utilized IR and thermal conductivity detectors to determine the C/H/N/S and oxygen by difference of the kerogen samples. Sample size capabilities were from 1 to 10 mg.

4.2. Experimental Methods and Techniques

Section 4.1 described the equipment used in this work. This section describes how each piece of equipment was used in this work.

4.2.1. TGA

Experiments were conducted with approximately 10 milligrams of sample in an Inconel basket weighing approximately 400 mg and measuring 0.9 cm diameter and 0.4 cm tall. The basket was suspended from a thin chain attached to a Sartorius 4404MP8 microbalance. The reactor was purged with an inert gas for approximately fifteen minutes prior to any experiment. Any one of several inert gases can be used; however Helium was selected because of its high thermal conductivity and low density. This helped to ensure that heat transfer and buoyancy effects were minimized. The TGA was heated via electric heating elements in the reactor vessel. A thermocouple measured the gas temperature near the sample.

Buoyancy effects are a significant factor at elevated temperatures in the TGA. Buoyancy effects coupled with other instrument effects give a non-linear response function of both temperature and pressure. Clayton (2002) generated an apparent mass loss curve by running an empty basket with an inert material to represent the volume of the sample and recording the instrument response. This approach lumped all buoyancy and other effects into an instrument response curve. This is attractive because it includes any specific instrument effects. An example of such a buoyancy curve can be seen in Figure 16. Mohlen and Sulimma (1986) calculated buoyancy effects from knowledge of the flow rates and temperature.

The buoyancy correction technique used here is a modification of the Clayton method (2002). Clayton's method was tried first, but there was some variation found in replicates of the blanks. This variation was thought to arise from the orientation of the basket with respect to the flow. Even slight variations could affect the apparent buoyancy. The modification used a blank experiment to determine the form of a correction polynomial but instead of using a global set of polynomial coefficients for each correction the coefficients were estimated from the initial portion of each individual mass trace. This estimate was performed by first running an empty basket to determine the order of the polynomial (e.g., first or second order). The same order of the polynomial determined for the blank was estimated for each experiment by then fitting the first non-reacting portion of the mass trace to the determined polynomial and correcting the mass based on those parameters. The unreacting portion was taken at temperatures from 20 to approximately 200°C and then back to room temperature. Since sample mass loss was noted to be zero for the samples at these temperatures, a baseline could be established. The buoyancy was then predicted to follow the same polynomial fit throughout the experiment. The justification for this method is shown in Figure 16. Note how the blank basket followed the same curve throughout the entire experiment. The TGA used in this experiment produces a near perfect quadratic curve for a He atmosphere at 1 bar as seen in Figure 16.

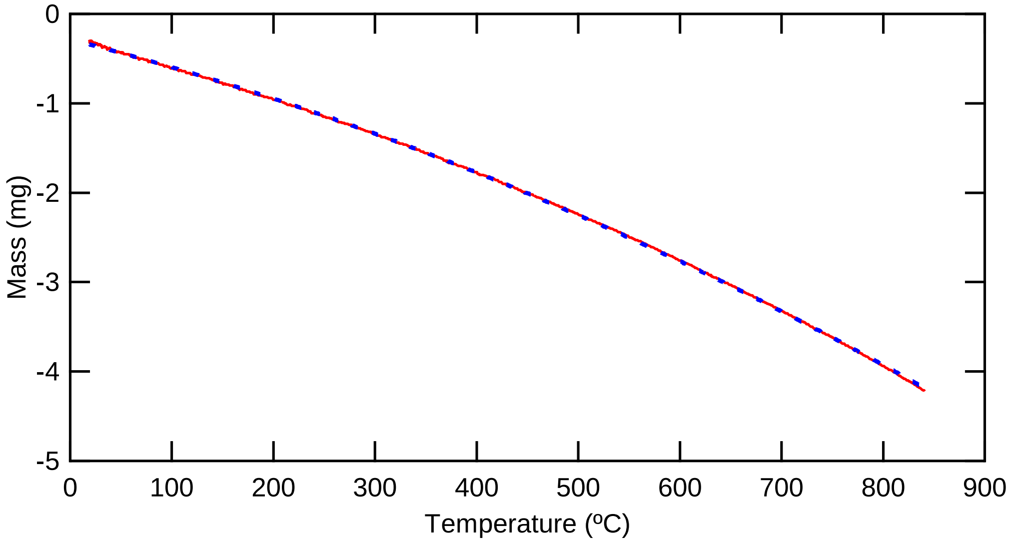

Figure 16. Example instrument response curve in He at 1 bar (solid line) overlaid with a second-order curve fit (dashed line). For this case, m = aT^2 + bT + c, and the R^2 value was 0.9999

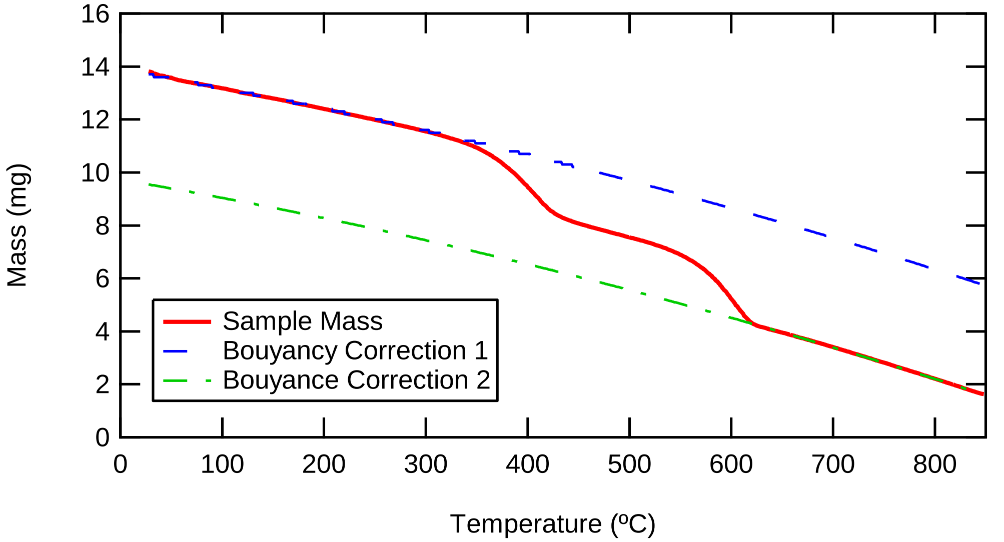

Figure 17. Example buoyancy curves predicted from raw data. Both the polynomial curves have the same coefficients but are shifted vertically by a constant value to show the fits at the initial and final portions of the TGA trace.

Figure 17 shows how the quadratic fits are used to correct for buoyancy throughout a pyrolysis experiment. First the buoyancy curve is predicted from the first 200°C and then extrapolated over the entire temperature range.

A second curve with the same polynomial parameters except a vertical shift is also shown to demonstrate the fit after the reaction has finished. In some cases the temperature region after reactions had finished were also used in refining the buoyancy curve polynomial parameters. The response for the 40 bar condition is closer to linear although the noise is much larger at pressure.

The buoyancy curves were subtracted from the real sample data and then normalized to achieve the final mass curves, as follows.

$$m'_{normal} = \frac{(m' - m'_f)}{(m'_o - m'_f)} \tag{10}$$

where m´ is the buoyancy corrected mass, m'_f is the final mass when reaction has stopped (corrected for buoyancy), and m'_0 is the initial mass (corrected for buoyancy). The result of Equation 1 is to normalize the mass and to make it range from zero to one. In this way it is related to conversion since the normalized mass equals one minus the conversion. Each sample was re-weighed on a separate microbalance after reaction, and the final weight was recorded as a consistency check. After the resulting corrections were applied then the mass shown in Figure 17 became the normalized mass shown in Figure 18.

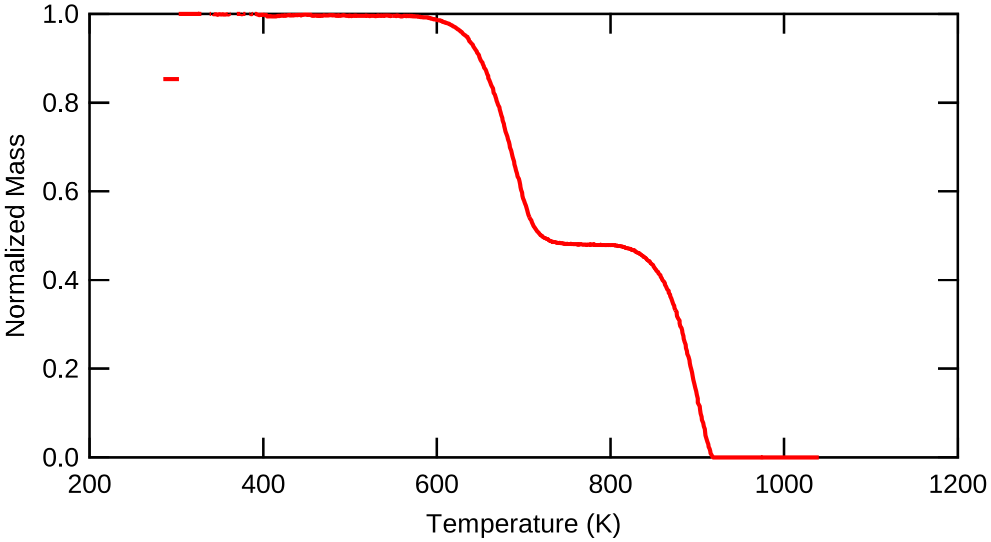

Figure 18. Resulting corrected and normalized mass loss curve from predicted buoyancy shown in Figure 17.

Once the buoyancy correction was applied, a temperature calibration was carried using the Currie point transitions of metals to determine and then adjust for the offset in temperature stemming from the fact that the thermocouple was not in the sample. Curie point temperature is a phenomenon in which a magnetic metal becomes paramagnetic when heated to a certain temperature. The process is reversible and happens very quickly. The metals used and their Curie point temperatures as reported by their manufactures are Alumel® (154.2°C), Nickel (355.3°C), Perkalloy® (596.0°C), Iron (770.0°C), and Hisat50® (1000°C). The calibration is performed by placing a piece of each metal in the basket and positioning it like a normal experimental run. Then a horseshoe style magnet is positioned around the TGA with the TGA (and basket) lying in the magnetic field passing between the ends of the arms. Then the magnet is adjusted vertically until a maximum mass change (to the positive) is observed on the balance. A visual inspection inside the reactor was performed to ensure that the magnet did not pull the basket to be in contact with the side of the reactor. Then the standards are heated under the same conditions as an experiment and the weight loss is observed. Figure 19 shows an example temperature calibration curve with the standards listed and their actual transition temperatures in parentheses (not corrected for buoyancy and without the Hisat50®).

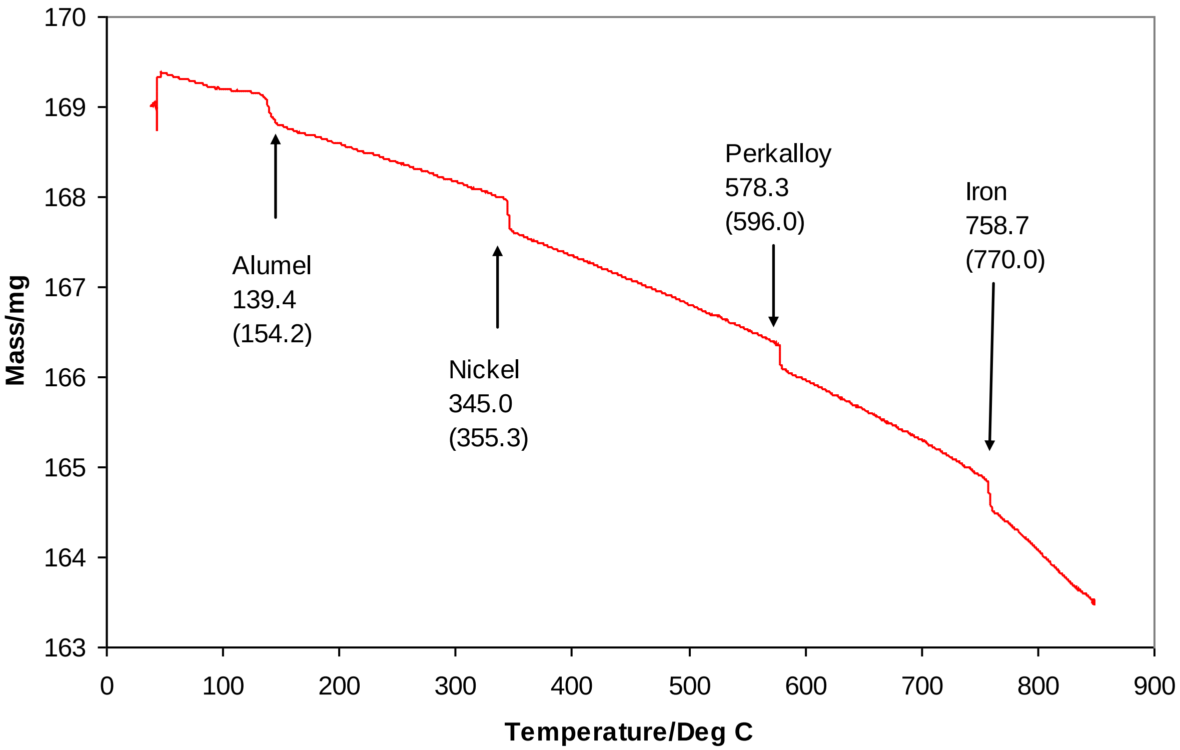

Figure 19. Curie point calibration curve example (1 Bar 10K/min, not corrected for buoyancy). The number directly below the standard's name is the experimental transition temperature in Celsius and the number in parenthesis is the actual transition temperature.

Note how in Figure 19 the temperatures read a bit low so the calibration would be accomplished by shifting the temperatures up that amount. Use of standards (acquired from *PerkinElmer*) provided a multi-point temperature calibration to which a cubic spline was fit and the temperatures were adjusted on each data set accordingly. Temperature calibrations were performed at each heating rate and pressure combination with replicates to demonstrate the reproducibility of the calibrations for the experimental conditions. The 40 bar curve revealed that the temperature needed to be adjusted down by some 50°C through the reaction region of interest but at lower temperatures the adjustment was not so drastic.

The data for these tests were collected at reactor pressures of 1 bar absolute and 40 bar ±1% absolute. For the 1 bar tests, the gas flows used were 1.0 L/min through the microbalance and 1.4 L/min through the reactor. The temperature controllers were set to run from 20 °C to 850 °C (or 950°C for some high pressure conditions) at 1 ° C/min, 4 °C/min, and 10 °C/min. The experimental procedure for the kinetic parameters was as follows:

1. A known mass of sieved sample was placed into a sample basket and introduced into the TGA.
2. The pressure was allowed to stabilize and the TGA purged with an inert gas prior to heating.
3. The sample was heated at one of three heating rates: 1K/min, 4K/min, or 10K/min. The final temperature of 850 °C (or 950 °C for a few cases) was maintained for 5 min at the conclusion of the run and then the sample and reactor were allowed to cool to a safe temperature before removing the sample and weighing the final mass.
4. The relative time, temperature, weight, gas flow rates, and temperature set point for the entire experiment from room temperature until the 5 min dwell time were recorded.

Each run took between two hours and 14 hours, depending on the heating rate. The longer runs were conducted overnight. The equipment has been tested and the appropriate program modifications were made to prevent the system from overheating or exceeding the design pressure of the TGA. Table 4 lists the TGA experiments carried out for this project. Samples M-

OC and GRK-W were for scoping purposes only; Samples R-150, R-75, R-38, A-0, A-3, and A-7 were used in task 2.

Table 4. Test matrix with each X representing two or more replicates.

		1 K/min	**4 K/min**	**10 K/min**	**60 K/min**
M-OC	1 Bar		X		X
	40 Bar		X		X
GRK-W	1 Bar		X		X
	40 Bar		X		X
R-150	1 Bar	X	X	X	X
	40 Bar	X	X	X	X
R-75	1 Bar	X	X	X	
	40 Bar	X	X	X	
R-38	1 Bar	X	X	X	
	40 Bar	X	X	X	
A-0	1 Bar	X	X	X	
	40 Bar	X	X	X	
A-3	1 Bar	X	X	X	
	40 Bar	X	X	X	
A-7	1 Bar	X	X	X	
	40 Bar	X	X	X	

In the experimental procedure, two assumptions were made in order to calculate the pre-exponential factor and the activation energy. The first assumption was that the observed reaction rate is a good approximation of the intrinsic reaction rate due to the low heating rates. This means that reaction rate was not hindered by effects such as mass transfer. Any observed reaction happened in the instant it was observed. The second assumption was that the sample temperature was the same as the gas temperature. This would imply that there were negligible heat transfer effects. In order to ensure that both of these assumptions were valid a few different actions were taken. Approximately 10 milligrams of sample were used in the test. With a basket diameter of 9 mm, this gave a large surface area to volume ratio making it easier for the heat and mass to transfer through the entire sample quickly. Secondly slower heating rates were used, allowing more time for the sample to equilibrate. As the sample was heated at different rates the temperature of highest mass loss rate shifted. The rate coefficient parameters do not mathematically depend on heating rate. Nevertheless the first-order model can describe the shift in the temperature of the maximum rate of mass loss. One obscuring factor is heat transfer effects. To ensure that the heat transfer effects were negligible three different heating rates were used; 1 ° C/min, 4 °C/min, or 10 °C/min. A similar test was conducted at 60 °C/min and the overall shape of the curve differed from the previous three indicating heat and mass transfer effects.

4.2.2. Oil Shale Retort

Sample A-0.1600 for the oil shale retort were size-graded to be between -10 and -20 mesh size (0.853mm < d < 1.60mm). The samples were prepared by crushing the sample to a uniform size. The sample preparation was performed by a different organization but the size-grading was verified at BYU. The sample was divided into 8 fractions using a riffler prior to any experiments. Each division was approximately 450 gram partitions. The experiments were performed by charging the retort with a 450 gram portion of the sample. The reactor was purged prior to and for the duration of each experiment at 9L/min with N_2. The sample was heated at 10 K/min to one of the following final temperatures: 422, 438, 445, 452, 466, or 523 ºC.

Each piece of the retort was weighed prior to an experiment. The reactor was then placed in a heater and the thermocouple measuring the outlet gas was used to control the temperature of the reactor. After the experiment the reactor was removed from the heater and allowed to cool. Each piece was then weighed again and yields were calculated. The resulting char and tar were weighed and the light gases were determined by difference.

4.2.3. Kerogen Retort

Experiments in the kerogen retort were conducted by first weighing the u-shaped portion of the reactor. Second, a quantity of glass wool was fitted to the exit region of the reactor and the reactor was weighed again. Then approximately 1 gram of sample was added to the reactor and the reactor was shaken gently to spread out the sample while covering the entrance and exit. Sample A-7.PRO was the primary sample used but a few experiments with A-0.1600 were also conducted. Then individually the inlet and outlet sections were weighed (without the condensers), since some tars condensed in the outlet section of the reactor. The condensers were prepared by stuffing a few grams of a fine glass wool into a test tube and weighing the condensers. Then the reactor was placed vertically in a clam shell furnace and the condensers were put into place. The filter paper was cut to fit its holder and weighed. The gas lines connecting the gas source to the reactor, the outlet of the condensers to the filter paper, and the outlet to the venting system were attached and gas was allowed to flow. The gas used in this experiment was $N_{2,}$ which differed from the TGA experiments but was the same as that of the oil shale retort experiments found in section 4.1.2. The flow rates were approximately 1 L/min N_2. This decision to use N_2 was one of cost and availability. An additional experiment was conducted with He and the results did not differ from the N_2 experiments.

As the reactor was purged a leak check was performed on all the fittings to ensure no sample leaks. The condensers were then partially submerged into an isoproponal/dry ice bath to aid in condensing. Cooling of the gases was sufficient to cause an ice buildup on the external parts of the tubes that connected the condensers for the duration of the experiment. This cooled gas indicated that the temperature was low enough to condense the tars. After the purging period the furnace programming was started. The heating rate used in these experiments was 10 K/min. The final temperatures ranged from 422°C up to 700°C.

4.2.4. X-Ray Photoelectron Spectroscopy (XPS)

XPS experiments were performed by the BYU chemistry department. Sample preparation was done by first grinding the sample as necessary, and then applying the sample powder to a silicon wafer via non-conducting double sticky tape. The samples were scanned with a general surface scan specifically for the ranges associated with carbon, oxygen, and nitrogen. The samples were run for 40+ hours (a long time for XPS experiments), and scanning was conducted over a large surface area to increase the signal to noise ratio for the relatively weak nitrogen sample. An energy correction was made to compensate for a charged sample using the carbon (1s) peak at 284.8 eV. Originally XPS data were to be collected on all the samples but mineral signal/noise made it impossible to collect good data on part of the samples. XPS data was successfully collected for two extracted kerogens, A-7.PRO and A-7, and the A-7.PRO char. The forms and ratios of those forms of nitrogen and oxygen were then determined by curve fitting a mixed Gaussian/Lorenzian curve with a fixed maximum but a variable area. The resulting area ratios represented the mole fractions of each moiety.

The XPS scan for the oxygen range does not provide adequate separation between peaks, to distinguish between the forms of the oxygen-carbon bonds. As such, a method was reported by Kelemen and coworkers (1995) for the Argonne Premium Coals where oxygen functionality was determined through the effect of the individual oxygen species on the carbon peak. This method was used in this work. The method involved specific XPS shifts of the carbon around the C 1s peak based on the connection to oxygen. Such an analysis is of course sensitive to other heteroatoms that would produce similar shifts around the C 1s peak. Other factors that could influence the analysis are the level of mineral matter and the complexity of the minerals present. It was observed among the Argonne coals that those coals with low levels of minerals exhibited less tendency for non-uniform charging (Kelemen and Kwiatek, 1995). Non-uniform charging is a necessary prerequisite for the method here described. Once the data were collected around the C 1s peak then an analysis of the ratio of the areas gave the mol% of each type of carbon-oxygen bond.

4.2.5. GC/MS

Experiments on the GC/MS system were conducted with the source set at 150 ^{o}C. The temperature program for the GC method started at 50 ^{o}C and 1 minute. Next the column was heated up at 8 ^{o}C/minute to 300 ^{o}C and held there for 15 minutes. The solvent used to bring the pyrolyzate into solution was dichloromethane. This solvent was selected because it dissolved hydrocarbons well and was an acceptable solvent for the GC/MS applications. Analysis of GC/MS traces were performed both manually and with the associated ICIS software compound libraries.

Some experiments were performed with the kerogen retort (described in section 4.1.3) effluent directed directly into the mass spectrometer. The purpose of this equipment setup was to see if reaction temperature could separate the compounds collected. This was different from the aggregate samples collected at different final temperatures. The direct connection was problematic because there were multiple compounds seen at the various temperatures with no separation. The result was an unidentifiable collection of hydrocarbons.

4.2.6. Fourier Transform Infrared Radiation (FTIR)

FTIR experiments were performed to determine the nature of the species in the gas phase. The species of interest were the light hydrocarbons, CO, and methanol. The experiments were carried out by collecting all the effluent gas from the kerogen retort detailed in section 4.1.3 for three specific temperature ranges. These ranges were 200 ^{o}C to 295 ^{o}C, 300 ^{o}C to 395 ^{o}C, and 400 to 495 ^{o}C. These ranges were designed to span the early, middle, and late gas generation phases as seen on a TGA trace. The gases were collected by using a 100L Tedlar® gas sampling bag. The FTIR was prepared by purging the sample cell with N_2. A pump was fitted to the outlet of the cell. The bag was connected to the inlet of the FTIR and the contents were pumped through the gas cell for a period of time to ensure a representative sample was present.

4.2.7. Low Temperature Ashing

Moisture was determined using ASTM standard test D3173. This standard prescribes heating the sample at 108°C and holding the sample at that temperature for one hour. The difference between the mass before the test and the mass after the test is the moisture. Ashing according to ASTM standard D3174 has a final temperature of 750°C for determining the ash content which exceeds the temperature to decompose minerals present in the oil shale and possibly in the kerogen (which can be as low as 550°C). A different ashing test was therefore devised to determine the ash content. This test involved heating the sample to 500°C and holding for 80+ hours or until mass stopped changing. The furnace was swept with air. The total content minus the moisture and ash is defined as the organic content. There is a potential problem with this method in that a few minerals such as Dawsonite will give off water and CO_2 at temperatures as low as 350°C (Huggins and Green, 1973). The amount of the mineral sample that decomposes at lower temperature is assumed to be low. This assumption is verified in subsequent sections.

4.2.8. CHNS

CHNS experiments utilized approximately 2 mg of sample and a sulfamethazine standard to determine sulfur content. Three sample replicates were run and the results were averaged to determine the elemental analysis. Standard deviation values were determined to give an estimate of the spread of the three measurements. Values were corrected to be on a dry ash free basis. The oxygen content was calculated by difference.

5. **Parameter Regression Method**

This chapter describes a new method developed as part of this project to regress first order kinetic parameters (see Equation 2). The new method did not use linearized equations so the pre-exponential factor was not determined by extrapolation. The solution did not neglect any terms, a problem found in the derivation of other integral methods. The problem was further constrained by assuming that the heating rate had no effect on kinetic parameters (at low heating rates), and hence required that the same kinetic parameters fit similar mass curves generated over a small range of heating rates.

5.1. Outline of New Method

The new method proposed here fits the integral numerically and also requires that the mathematically calculated derivative also fit the derivative of the data. Fitting the mass curve directly with the integrated form avoids both (a) the assumptions made by the analytical solutions and (b) the determination of which points to include in the analysis. This new method essentially weights most heavily the portion of the curve where the rate of mass loss is the highest. Many of the techniques used in this new method are not unique, but the combination of the techniques is novel.

The differential equation (Equations 2, 5, and 6 are reproduced below for convenience) is manipulated into the form shown in Equation 5, and then analytically integrated to the form shown in Equation 6. The integral as shown in Equation 6 can easily be evaluated with a numerical integration technique, but requires a numerical optimization method to fit the model to the given mass curves. The optimization method is required because unlike the linear methods these non-linear methods do not have an easily determined slope and intercept from which the kinetic parameters can be determined. Iteration on the kinetic parameters is required to find the best fit to the data.

$$\frac{dm}{dt} = -A \cdot \exp\left(\frac{E}{R \cdot T}\right) \cdot m \tag{2}$$

$$\int_{m_0}^{m} \frac{dm}{m} = \int_0^t - A \cdot e^{-E/R \cdot T} dt \tag{5}$$

$$m = m_0 \cdot \exp\left(\int_0^t - A \cdot e^{-E/R \cdot T} \ dt\right) \tag{6}$$

5.2. Optimization Techniques

The determination of a non-linear set of parameters requires some form of numerical search. The optimization program OptdesX® was used here (Parkinson and Balling, 2002), but any program with the necessary optimization routines can be used. OptdesX® requires that the fitting and objective functions be provided through a C or FORTRAN subroutine and can be run on a Linux machine. Functions were programmed to fit and minimize a sum squared error of the differences between (a) the measured non-isothermal TGA traces, (b) calculations using Equation 2, and (c) calculations using Equation 6. In the analysis, the error for both the integral and derivative associated with each data point versus time was scaled to normalize their respective weight in calculating the error. This was accomplished by dividing the error from each point by the total number of points in the trace to which it belongs. This scaling divides the error in half for the individual points belonging to traces with twice as many points as those with half as many points. The weighting also allows for adjustment of the relative weight of fitting the mass traces to the relative weight of the peaks fit of the derivative curve. Fitting two replicates of each of the two heating rates (1K/min and 10K/min) with their derivatives required less than three minutes. The majority of the time was spent in the simulated annealing portion of the analysis.

The optimization algorithm used here was the simulated annealing (SA) method followed by the generalized reduced gradient (GRG). Simulated annealing was so named because it mirrors the annealing process found in nature. A brief overview of SA is included here for convenience; an analogy between annealing and simulated annealing as well as further information about SA can be found in the work of Liu (1990). Heating a solid to a liquid state and then cooling it slowly to a solid generally allows the atoms to assume a minimum energy state. Likewise a minimization system is started at a “high energy” state and random perturbations are made to the parameters. The solution using the new parameters is compared with the current solution. If the new solution has a lower sum squared error it is automatically chosen; but if the sum squared error is larger, the program probabilistically decides, according to the Boltzmann factor, between moving to the state with a higher sum squared error and staying in the current state. This is repeated for 1000 cycles until the program brings the system from an arbitrary initial point chosen by the user, to a point that is as least as good as the starting point. The end point is almost always a much better fit based on sum square error. With each cycle the system is “cooled,” meaning the probability of accepting a worse set of parameters decreases just like in the annealing process where the molecules of a solid slowly lock into place. When the SA optimization is completed, a generalized reduced gradient algorithm finds the nearest local optimum. If a generalized reduced gradient (GRG) numerical method were used alone then it would merely find the nearest local optimum without any hope to find the global optimum. Simulated annealing gives more hope of being in the region of the global optimum.

5.3. Mathematically Generated Data

Validation of this method was carried out mathematically by generating mass loss data from two parallel first-order equations with different activation energies. Randomly distributed noise of up to ± 0.2% was added to each data point. The noise is important because it is one of the many mechanisms that causes the linearized methods to mispredict the kinetic parameters. At each point, “real” data points are some function of the kinetic parameters and error in the measurement.

$$m_i = f\left(E, A, m_{i-1}, T_i\right) + \varepsilon_i \tag{11}$$

Equation 11 shows the general situation that the mass at the ith point is some function (such as what can be represented with a first order model) plus some error in measurement, ε. The noise levels chosen are similar to levels of noise observed in this research. These simulated measurement errors are also the source of the curvature, seen in Figure 20 at the temperature extremes of the derivative curves, and the jagged features at the low temperature region of the integral curves (Figure 20). The source of the difficulty in choosing which points to include in the analysis is a combination of the noise and deviation from a first order model.

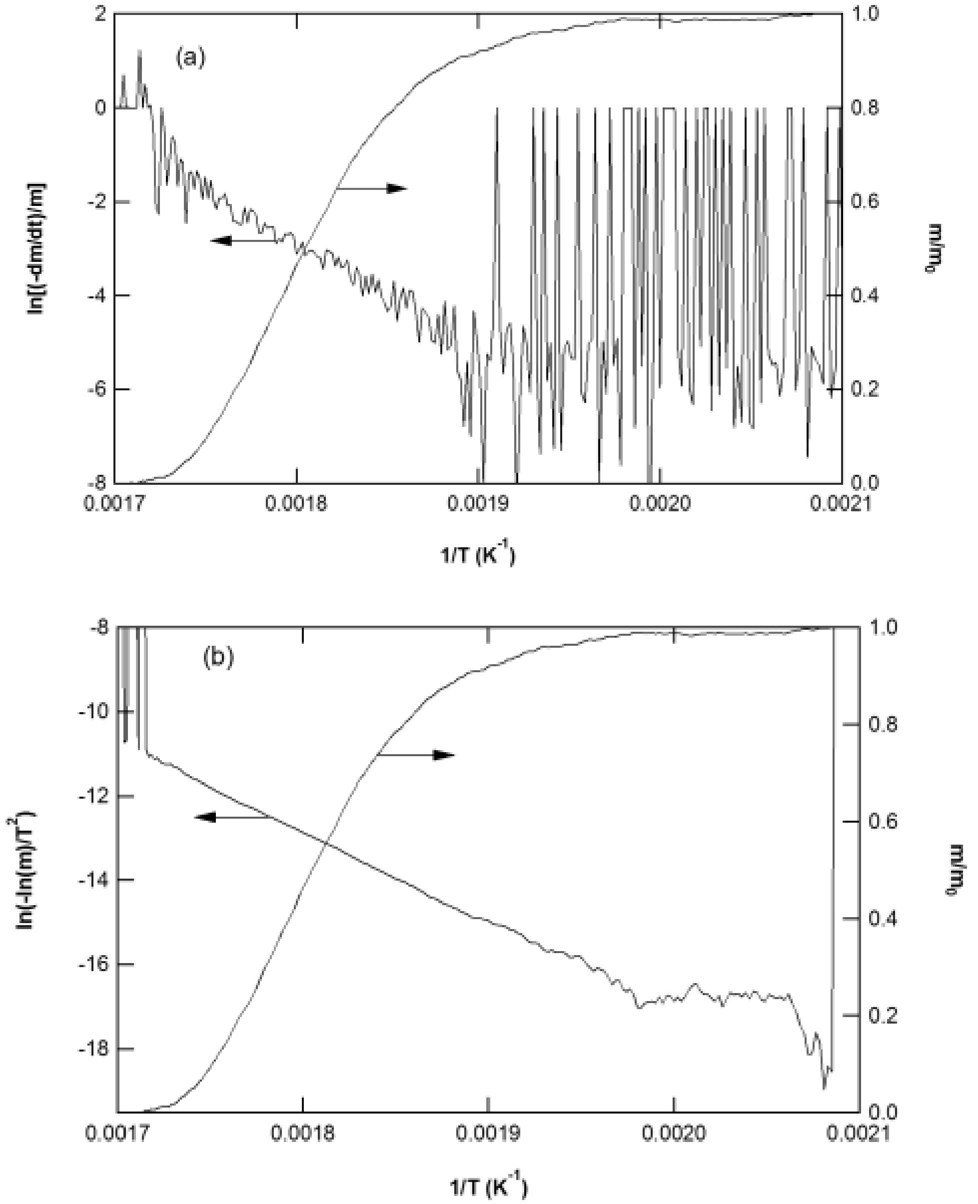

Figure 20. (a) Derivative and (b) Integral reduction of the same mathematically generated data (with noise).

Linearization of the rate equation affects the statistical treatment for the resulting parameters. Equation 11 shows the form of the error of the rate equation if the integral method is used. Once linearized, Equation 11 leads to Equation 12. Note how the error is now inside of the natural log term and hence, instead of a normal error, it is now a form of log normal error.

$$\ln(m_i) = \ln\left(f\left(E, A, m_{i-1}, T_i\right) + \left(\varepsilon_i\right)\right) \tag{12}$$

The error means a traditional statistical analysis based on the central limit theorem is no longer valid.

Four validation experiments were performed, with kinetic parameters shown in Table 5. Each validation experiment consisted of four separate mass traces: simulated data were generated at heating rates of 1 and 10 K/min, with a replicate at each heating rate. The replicate data sets had random noise, and hence were slightly different from each other. Two sets of kinetic parameters (two pairs of A's and E's) were generated by an undergraduate research assistant and not made known until after the optimal kinetic parameters for that experiment were determined. A sample of the generated data is shown in Figure 21.

Table 5. Kinetic parameters selected for the validation experiments.

	First Reaction		Second Reaction	
Experiment	**A (1/s)**	**E (kJ/mol)**	**A (1/s)**	**E (kJ/mol)**
1	1.59E+15	175	1.45E+12	250
2	1.32E+09	175	1.78E+08	219
3	2.35E+17	225	4.03E+02	85
4	7.20E+10	150	7.20E+10	225

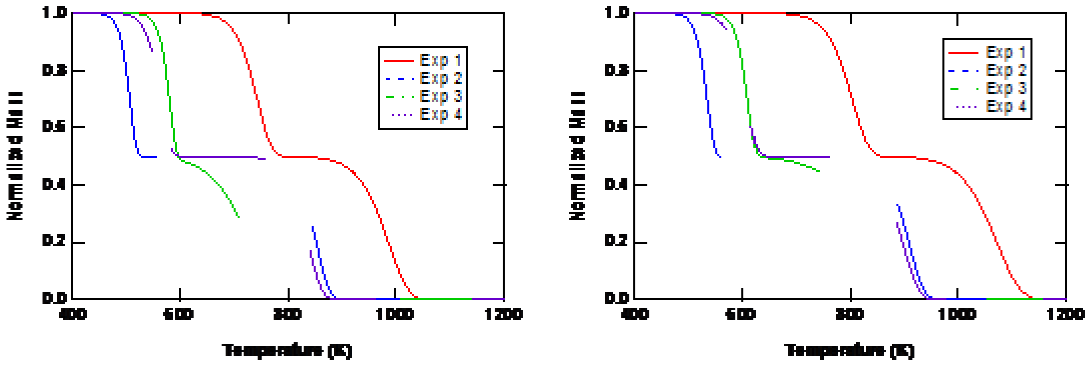

(a) Mass vs. temperature at 1 K/s (b) Mass vs. temperature at 10 K/s

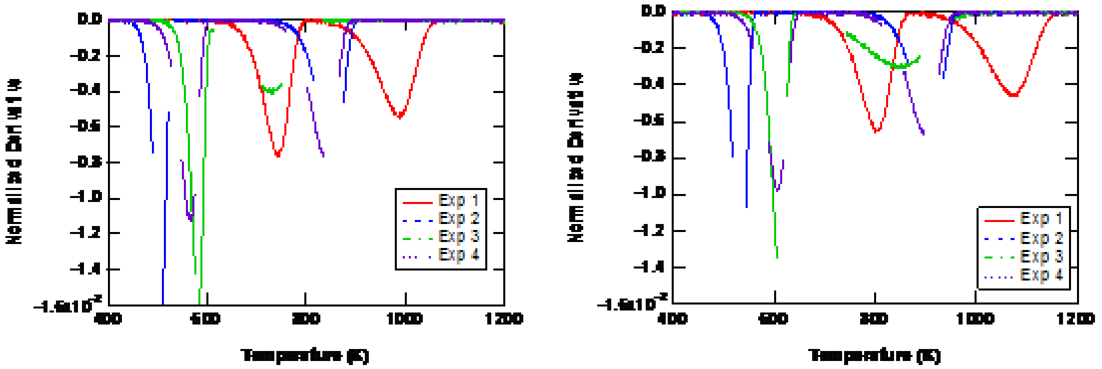

(c) Derivative vs. temperature at 1 K/s (d) Derivative vs. temperature at 10 K/s

Figure 21. Sample data at two heating rates with randomized noise. The kinetic coefficients used to generate data for the different experiments are listed in Table 5.

The optimization procedure described in this chapter was then applied to determine the kinetic parameters. The integral and derivative methods were also applied to each validation experiment.

Numerical experiments were conducted on each data set to determine if the number of points included in the integral and derivative methods affected the predicted results. These experiments were conducted by selecting a set number of points to include, centred on the point of maximum mass loss in the first of the two reactions, and then including all points whose value of the derivative was at least 10% of the maximum rate of mass loss. The number of points is reported here as the number of points on each side of the maximum; for example, “10 points” means 10 points on each side or a total of 21 points. The amount of “all the points” varied somewhat between each case but was always above 100. The numbers of points were chosen to considered the sections of curve where the rates of mass loss were approximately 8%, 15%, 30%, and 90% of the maximum mass loss. The actual choices are less important but this shows that changes in the values of the kinetic parameter will result if left to an experimenter to decide which points to include.

The pre-exponential factor (A) for the linearized integral method, as shown in Equation 2, is dependent upon the temperature and will vary a few percent depending on the temperature selected for the analysis. This analysis used the temperature at the highest rate of mass loss to determine the pre-exponential factor in the integral method. The temperature range of 298 K to 1223 K (25°C to 950°C) was the same in all experiments. This temperature range and the activation energy range for the first reaction are similar to pyrolysis reactions for organic material such as coal, and the second reaction is similar to mineral decomposition such as would be found in organic geochemistry reactions.

5.4. Results of Mathematical Experiment

The optimization program used all four mass traces generated at different heating rates for a given set of parameters to determine coefficients for each of the experiments listed in Table 5. Traditionally the integral and derivative methods used only one mass trace. The use of one mass trace comes from the “pencil and paper” days (pre computer). Likewise here only one mass trace is used for the linearized integral and derivative methods. Therefore, only the first of the four mass traces was used for the linearized methods; the trace had a heating rate of 1 K/min.

The results from the point selection experiments (where kinetic parameters were shown to be dependent on which points were included in the analysis) are shown in Figure 22–Figure 25. Figure 22 is a good example of why the integral method has persisted as a favorite method across the past decades. Note how the activation energy values using the integral method agree quite well with the actual value. The poorest agreement for integral values of E in Figure 23 occurred when all the points were included in the analysis. The derivative method obtained lower activation energies for the same experiments. For the derivative method there was some compensation in the pre-exponential factor, especially when all the points were included in the derivative analysis though the activation energy was only 32 kJ/mol different.

A simple calculation reveals that at the activation energy values in Figure 22 (Experiment 1) an increase of 10 kJ/mol requires an order of magnitude increase in the pre-exponential factor at 500K to result in the same Arrhenius rate coefficient (k). Shown in Figure 22–Figure 25 are demonstrations of how the number of points selected can alter the predicted kinetic parameters. The derivative method is more sensitive to the point selection problem though the integral method also varies at least 5 kJ/mol between that predicted for the 10 points on each side case to that predicted for all the points. These figures also show that the integral method gives a better estimate than the derivative method. Therefore if a researcher is deciding between the integral and derivative method the better choice is the integral method. However, of the three methods compared, the new method proposed in this research most nearly matches the mathematically generated data in every case.

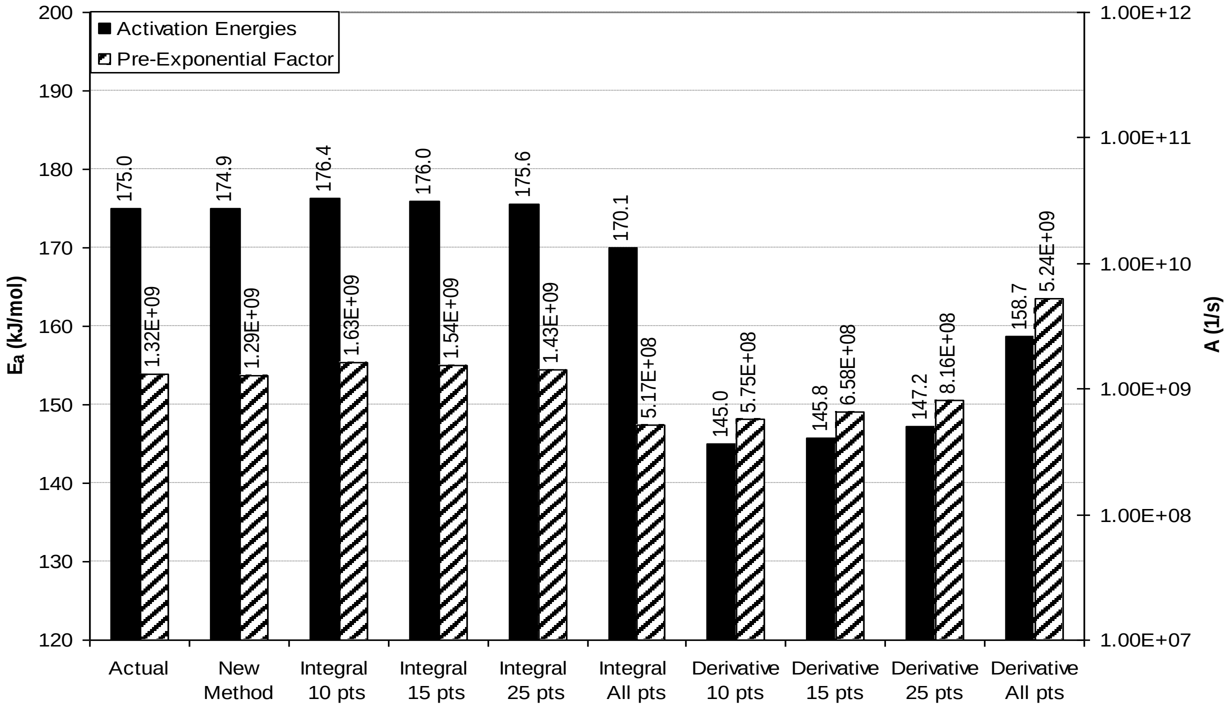

Figure 22. Kinetic parameter results from fitting of mathematically generated data for experiment 1. Corresponding pre-exponential factors included for convenience.

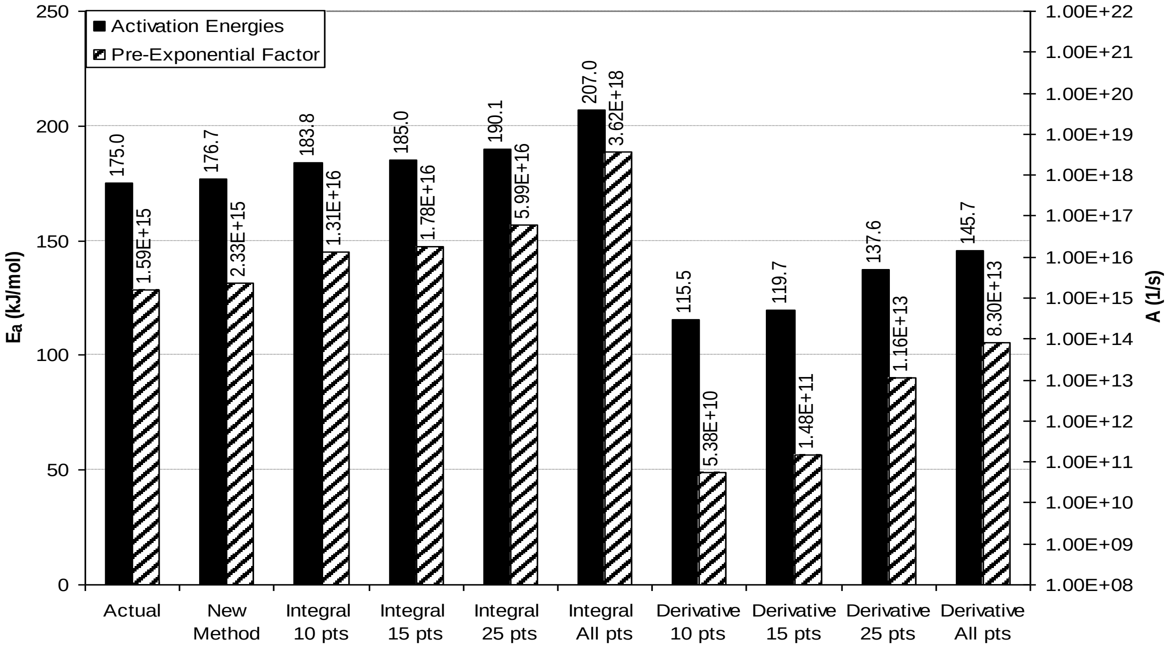

Figure 23. Kinetic parameter results from fitting of mathematically generated data for experiment 2. Corresponding pre-exponential factors pre-exponential factor included for convenience.

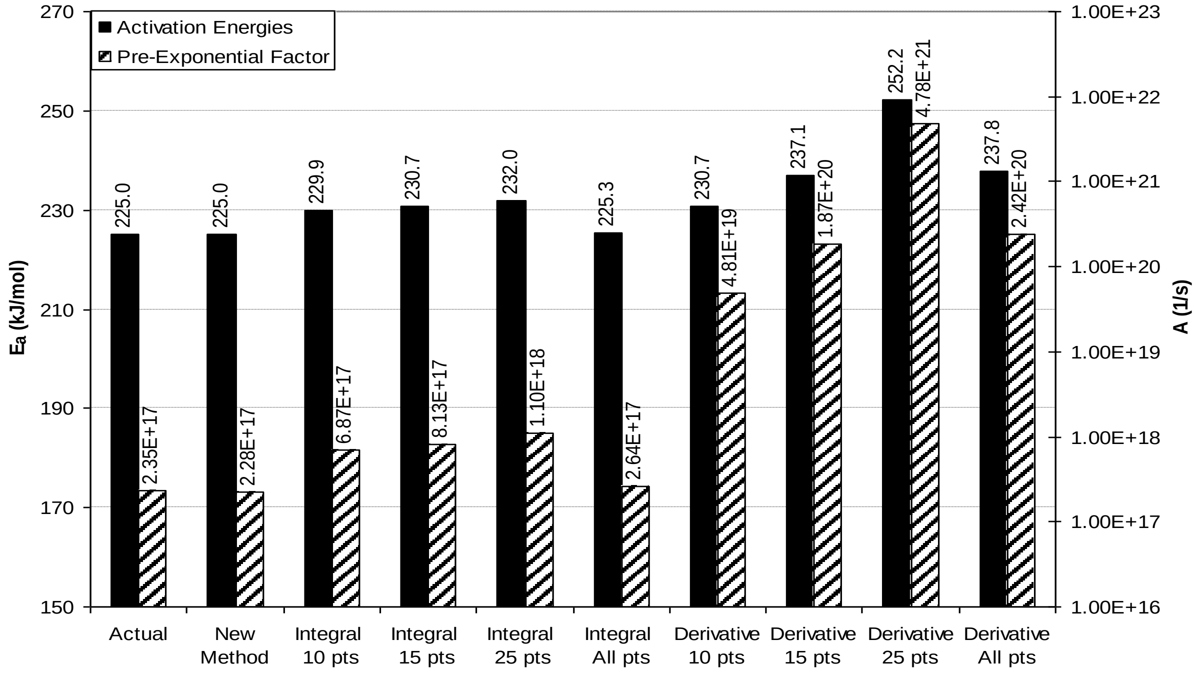

Figure 24. Kinetic parameter results from fitting of mathematically generated data for experiment 3. Corresponding pre-exponential factors pre-exponential factor included for convenience.

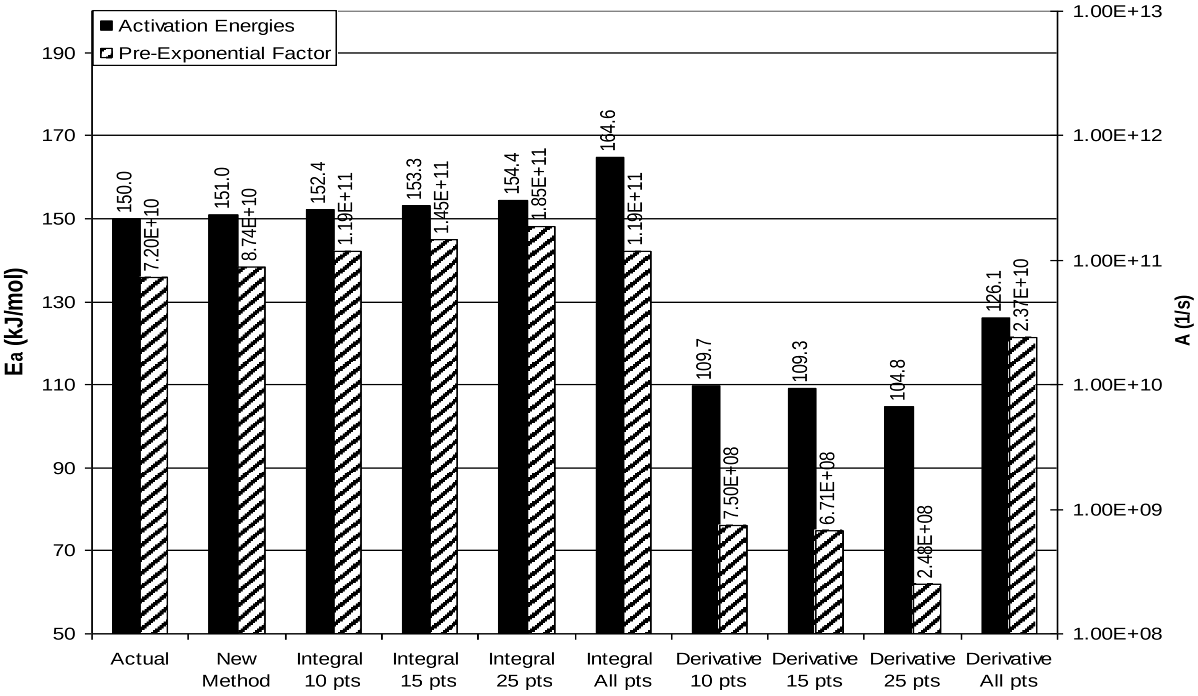

Figure 25. Kinetic parameter results from fitting of mathematically generated data for experiment 4. Corresponding pre-exponential factors pre-exponential factor included for convenience.

Because E and A are correlated, a comparison was made of the calculated values of k at temperatures representative of each peak. The temperatures selected were 500 K for the first reaction and 600 K for the second reaction. The values of E and A were taken from the curve fit using all of the data points, shown in Table 5. The comparison of k values is presented in Table 6. The error was calculated according to Equation 13.

Table 6. Comparison of k values at (or near) temperature of maximum reaction rate for each reaction in a two parallel reaction system.

First Reaction at 500 K			Second Reaction at 600 K		
		Error*			**Error***
Experiment 1	Actual	0.00%	Experiment 1	Actual	0.00%
	New Method	-2.67%		New Method	-2.15%
	Integral	3.04%		Integral	12.21%
	Derivative Method	5960.29%		Derivative Method	23530.43%
Experiment 2	Actual	0.00%	Experiment 2	Actual	0.00%
	New Method	-0.50%		New Method	-6.84%
	Integral	28.04%		Integral	-65.48%
	Derivative Method	20095.95%		Derivative Method	17457.67%
Experiment 3	Actual	0.00%	Experiment 3	Actual	0.00%
	New Method	-2.70%		New Method	-0.73%
	Integral	5.58%		Integral	-37.80%
	Derivative Method	4607.10%		Derivative Method	5986.69%
Experiment 4	Actual	0.00%	Experiment 4	Actual	0.00%
	New Method	-4.12%		New Method	4.77%
	Integral	-95.10%		Integral	19.97%
	Derivative Method	10273.64%		Derivative Method	19774.26%

*Error is calculated according to Equation 13

$$error = \frac{\left(k_{model} - k_{actual}\right)}{k_{actual}} \qquad (13)$$

It can be seen that the error generated from each type of regression method can change the predicted rate constant significantly, which in turn changes the predicted mass versus time curve. As indicated above, these numerical experiments involved generating data with an activation energy and pre-exponential factor initially hidden from the person performing the optimization. Initially, the first reaction of the third experiment gave an error of 32.52% using the new method. The source of this error was that the maximum allowable value for the pre-exponential factor in the optimization routine was not set high enough. Therefore the optimization program was prevented from searching in the area of the correct answer. This problem was rectified by setting the bounds to include many orders of magnitude, using one of the other methods for a first guess, or using some form of existing reaction rate theory. A final error of only -2.70% (shown in Table 6) was obtained when the regression was performed using the enlarged search area.

The new method for obtaining kinetic constants from non-isothermal data works because (1) it does not require extrapolation of the intercept to determine the pre-exponential factor; (2) it does not require a somewhat arbitrary determination of what points will be included in the regression; and (3) it does not require the same assumptions as the linearized integral methods to be made in its derivation. This new method is not limited to using a first-order equation, or to linear heating rates. Any rate equation that describes a system and can be expressed mathematically could be used to determine best-fit parameters.

5.5. Discussion of the Strength of this Method

It is noted that ln(A) and E are linearly correlated or auto-correlated. A paper by Brill (1994) describes a method to compensate for this correlation of variables. This effect was not first pointed out by Brill and has been described elsewhere in the literature (Essenhigh and Misra, 1990). The reason for this effect can be seen from the Arrhenius form rate constant. At a given temperature and increase in the activation energy and a corresponding increase in the pre-exponential factor can give the same numerical value for the rate equation. Another explanation for the observed effect can be seen when a joint 95% confidence region is constructed for the parameters. The shape of the confidence region is similar to a narrow crescent for A vs. E or it is a narrow oval for ln(A) vs. E. The major axis of the oval shaped confidence region is oriented diagonally with a positive slope in a plot of ln(A) vs. E. This gives the apparent linear correlation. Figure 26 shows both the confidence region for the A vs. E and the oval shaped joint region for ln(A) vs. E.

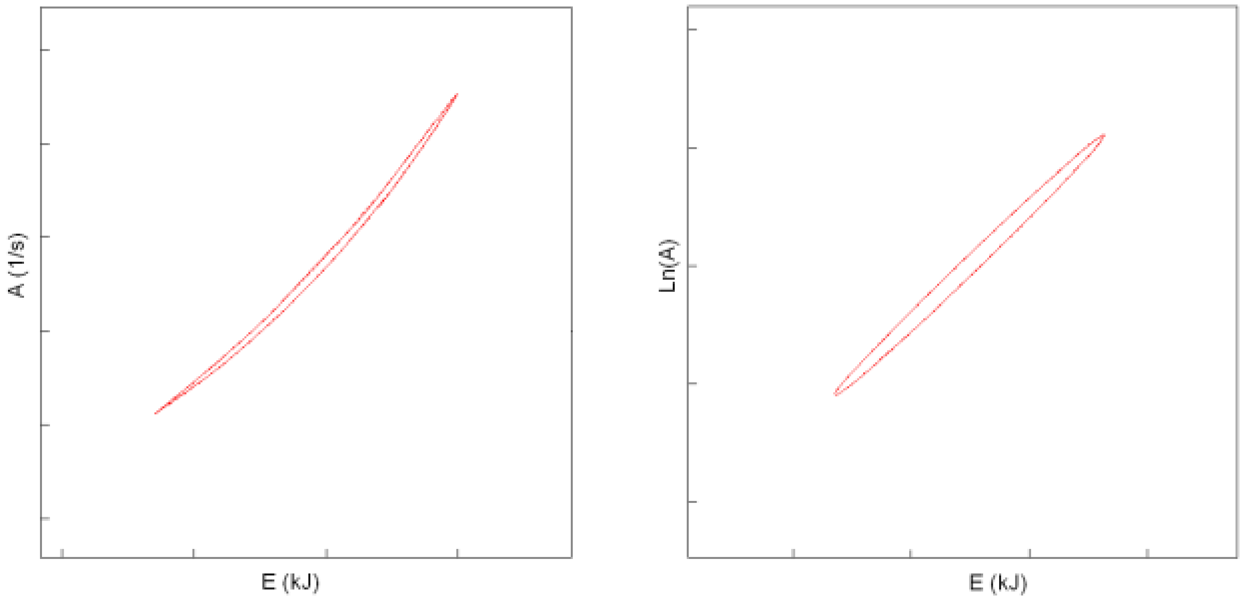

(a)

(b)

Figure 26. Example joint confidence regions (a) is a 95% joint region of A and E (b) is a 95% joint region of Ln(A) and E (note the axes are not on the same scale).

The methodology for constructing a joint confidence region can be found in statistics textbooks such as one authored by Seber (2003) or by Draper (1998). The confidence region includes many seemingly different sets of kinetic parameters but it has an **optimum that can be found**. However, as shown in the appendix section A-1.2, all E and A combinations do not describe the data equally, which is why the Brill method was not used here.

5.6. Conclusion

A new method was proposed to determine kinetic coefficients from non-isothermal data. The method involved using an optimization technique to fit the mass versus time curve as well as the derivative versus time curve. Previous methods have linearized the rate equation in order to make graphical analysis easier. The limitations of the linearized methods comes from both (a) extrapolation to the intercept to determine the pre-exponential factor and (b) the somewhat arbitrary determination of what points are in the linear region of the graph after the data have been linearized. Fitting the entire mass curve and constraining the kinetic parameter to fit the derivative does not depend on either extrapolation nor does it depend upon a decision of where to start and stop the numerical analysis. A set of numerical experiments were performed on simulated data sets using the new method, a common integral method, and a common derivative method. This new method was shown to out-perform the traditional derivative and integral methods in percent error. The integral method was shown to out-perform the derivative method. The result is an improved method for determining the kinetic parameters. This method can in principle be used to fit as many mass traces as desired, but multiple curves at various heating rates are recommended.

6. **Oil Shale Kinetic Parameters**

6.1. TGA Data

TGA data were collected on oil shale and kerogen as described in sections 4.1.1 and 4.2.1. The TGA data were recorded at approximately 0.75 second intervals across the entire experimental run. This gave a total of around 1,500 data points for the shorter experiments and over 65,000 data points for the longer experiments. The experiments were conducted by heating the sample at a constant heating rate to a temperature that exceeded the reactions of interest. The sample was held for 5 minutes at the maximum temperature before allowing it to cool.

6.2. Data Reduction

Each set of data was reduced to approximately 1000 data points by boxcar averaging the appropriate number of points and assuming that the irregularities are the result of random noise. Some additional moving average smoothing was employed for especially noisy data sets. The averaged data and the original data were compared to ensure that no important features of the data were lost. Each TGA trace showed between 1 and 4 distinct reaction regions. The number of regions was consistent with the sample. For example, the demineralization stages eliminated regions of carbonate pyrolysis and other reactions at successive stages of the demineralization.

The size-graded samples each showed the same number of reaction regions. Each reaction was assumed to be a first-order global reaction with an Arrhenius form of the rate constant. A first order reaction with an Arrhenius constant is most likely not the best reaction mechanism for the mineral reaction but since only the organic reaction was of interest no effort was made to find the best model for the minerals. The activation energies were either assumed constant or as a progressive distributed activation energy similar to that used in the CPD model by Fletcher and coworkers (1989).

Once the mass traces were corrected using the method described in 4.1.1 and normalized the kinetic parameters were determined with the method described in Section 5. The method used a non-linear optimization program to match model predictions with measured data. Mass was calculated numerically by integrating differential rate expressions. The method also required that the predicted derivative matched the derivative of the data. The kinetic parameters were determined by an optimized best fit of both the mass curves from three heating rates simultaneously, along with the derivative curves of the mass curves.

6.3. *Chemical Kinetics Models*

The pyrolysis data in this study were modeled using both a first order model, shown in Equation 2, and a progressive Distributed Activation Energy Model (DAEM), shown in Equations 9 and 14.

$$\frac{dm}{dt} = -A \cdot e^{-\left(\bar{E} \pm \sigma\right)/R \cdot T} \cdot m \tag{14}$$

The DAEM was applied in a similar manner to that of Fletcher and coworkers (1989). The method of Fletcher et al. changes the constant E in the first order model into a distributed activation energy described by a mean effective activation energy and a Gaussian distribution, $\overline{E}$ and σ respectively. This distribution is determined as a function of the extent of conversion of the sample. This assumes that material with low activation energy is released first, and that high activation energy material is released last, which seems physically reasonable. Note that when the σ is zero the DAEM becomes the 1st order model. This feature lends itself to a comparison between the models using an F-test.

6.4. *Statistical Theory*

The comparison of two models where one model becomes the second model by setting one or more of the parameters to zero lends itself to an F-test. This test is conducted using Equation 15. In Equation 15 SS(θ) represents the error between the model and the set of parameters for the respective equation. The subscript 1 represents 1st order model and the 2 represents the DAEM, p is the number of estimated parameters in each model, and n is the number of observations. The null hypotheses, H_0, is that no difference exists between the fits of the two models subject to the comparison of F in Equation 15, with critical values as determined from an F distribution.

$$F = \frac{\left(SS(\hat{\theta})_1 - SS(\hat{\theta})_2\right)/(p_1 - p_2)}{SS(\hat{\theta})_2/(n - p_2)} \tag{15}$$

The construction of a joint confidence region can be accomplished by Equation 16. In Equation 15 and Equation 16, $\hat{\theta}$ represents the optimal parameters, F is the inverse distribution as a function of the confidence level, α, and the degrees of freedom. In Equation 16 θ represents the vector of parameters regressed from either Equation 6 or 9.

$$SS(\theta) \leq SS(\hat{\theta}) \cdot \left(1 + \frac{p}{n-p} \cdot F_{p,n-p,1-\alpha}\right) \tag{16}$$

As in Equation 15, n is the number of observations and p is the number of parameters. From observation of Equation 16 there are two methods of shrinking the size of the critical value (i.e., the RHS of 16) used in constructing the confidence regions for a given model at a given confidence level. The first is to increase the number of observations. This affects the portion of the RHS of 16 enclosed in the parentheses. For example, given the 1st order model with an alpha of 0.5 the portion in the parentheses has a value of 3.57 for an n of 6 but falls to 1.23 for an n of 30 and approaches a value of 1.0 for an n of infinity. The other method of decreasing the critical value is to decrease the error associated with the optimal parameters (i.e. collect better data). Better data would either be associated with lower noise and lower measurement errors or in the case of non-isothermal kinetic data it would be to have a wider spread in the heating rates. Higher heating rates often are obscured by other effects such as mass transfer and hence there is an upper limit. Lower heating rates become time consuming and costly. The heating rates for this study were selected (as mentioned above) to span the widest range that would ensure no mass or heat transfer effects at the higher heating rates and to be performed in a reasonable time for the experimental setup at the lower heating rates.

6.5. Results of Models and Parameters vs. TGA Data

The objective of this work was to determine global kinetic parameters for specific samples of oil shale and their derivatives from the Green River formation. Typical mass and derivative curves are shown in Figure 27. Table 7 shows the typical mineral composition of the A-0 sample used in this research.

Table 7. Minerals for Sample A-0 as determined by XRD rounded to the nearest whole percent (except siderite which was rounded up to the nearest half percent)

Minerals	Percent Weight
Ank. or exc-Ca Dol.	30
K-feldspar	15
Calcite	14
Quartz	11
Organics	9
Buddingtonite	6
Analcime	6
Plagioclase	4
Pyrite	1
Siderite	0.5
SUM NON-CLAY	*96*
Di 2:1 Clay	4
SUM CLAY	*4*

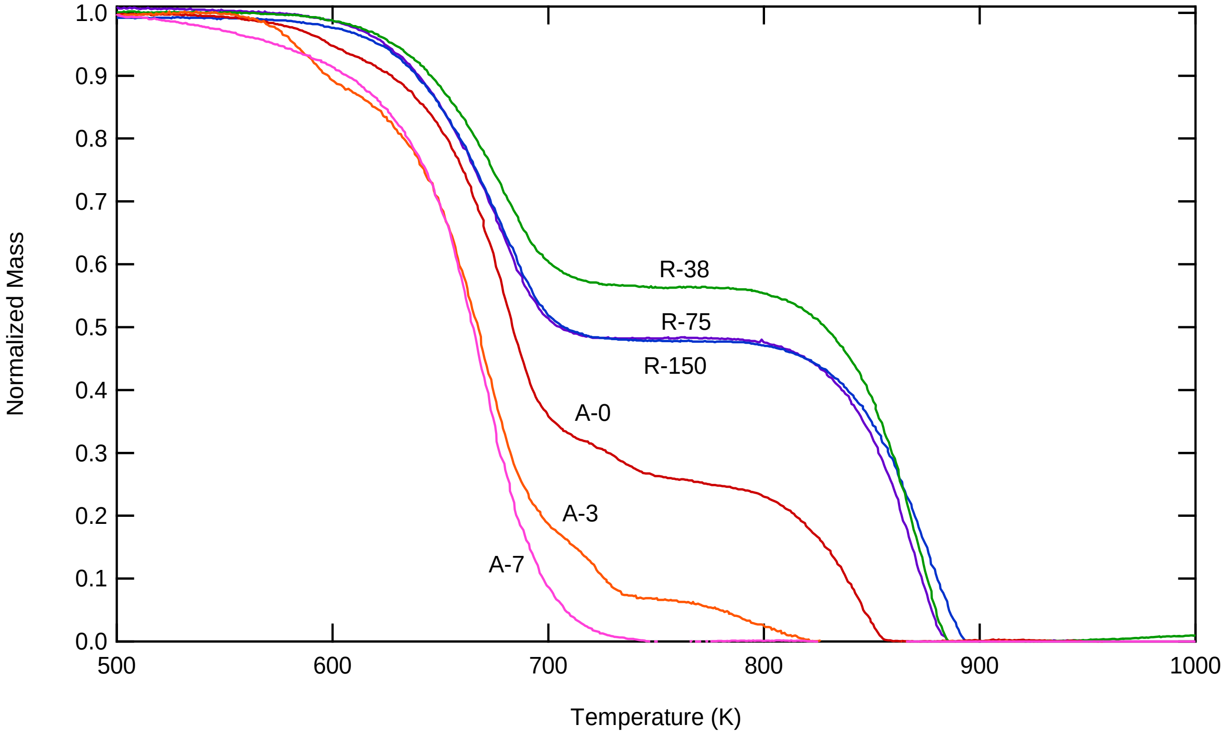

(a) Mass Traces

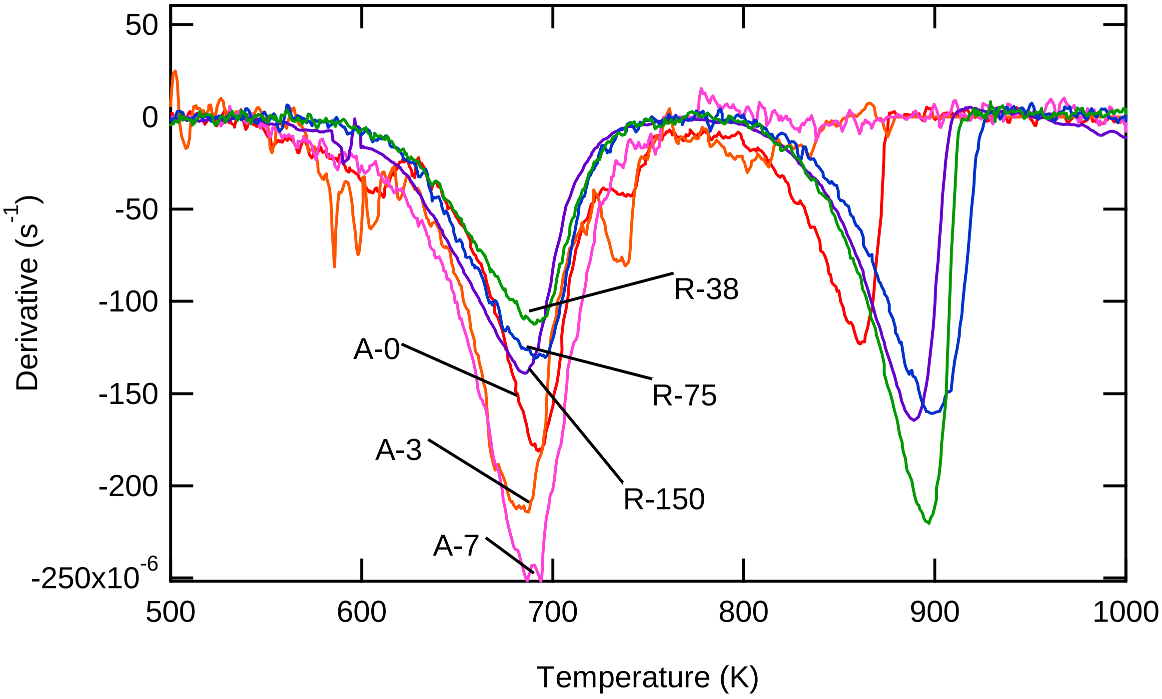

(b) Derivative Traces

Figure 27. Examples of buoyancy and temperature corrected mass data (1Bar, 1 K/min)

Two peaks were observed in the derivative of the mass curve with temperature for samples R-150, R-75, and R-38 while four peaks were observed on sample A-0. The subsequent stages of demineralization show three peaks for A-3 and one peak with a shoulder for A-7. The mineral analysis of sample A-0 is shown in Table 7. The reaction of interest is the pyrolysis of the organic matter in the shale and occurs between about 600 and 800 K. The higher temperature reactions involve primarily the mineral matrix and are not included here.

The parameters in Table 8 were regressed using the method explained in section 5 and elsewhere (Hillier et al., 2010; Hillier and Fletcher, 2011). Parameters were regressed for both first order reaction and distributed activation energy models. A comparison of the first two columns of Table 8 demonstrates how the kinetic parameters were similar at the two pressures for each sample using the 1st order model. A similar comparison of columns three and four lead to a similar conclusion for the DAEM.

Table 8. 1st order and DAEM parameters regressed for oil shale samples and statistical model comparison based on Equation 5

Sample		**1st Order**		**DAEM**	
		1Bar	40Bar	1Bar	40Bar
A-0	A (1/s)	6.99E+12	1.29E+13	2.67E+13	6.33E+13
	E (kJ/mol)	210.0	211.1	220.0	222.2
	σ (kJ)	~	~	2.7	1.7
A-3	A (1/s)	8.21E+12	2.23E+13	2.10E+13	1.87E+14
	E (kJ/mol)	210.0	212.4	213.4	225.6
	σ (kJ)	~	~	1.7	3.3
A-7	A (1/s)	5.04E+12	7.36E+12	2.69E+13	1.35E+13
	E (kJ/mol)	208.8	212.4	218.6	216.0
	σ (kJ)	~	~	2.6	2.4
R-150	A (1/s)	2.74E+10	2.89E+10	2.35E+12	2.53E+12
	E (kJ/mol)	175.9	174.8	202.5	201.8
	σ (J)	~	~	3.2	3.8
R-75	A (1/s)	1.79E+10	3.04E+10	2.01E+12	2.85E+12
	E (kJ/mol)	173.8	175.6	202.4	203.0
	σ (kJ)	~	~	3.8	4.4
R-38	A (1/s)	2.91E+10	2.72E+10	6.73E+12	1.94E+12
	E (kJ/mol)	177.0	176.9	208.8	202.1
	σ (kJ)	~	~	1.9	2.6

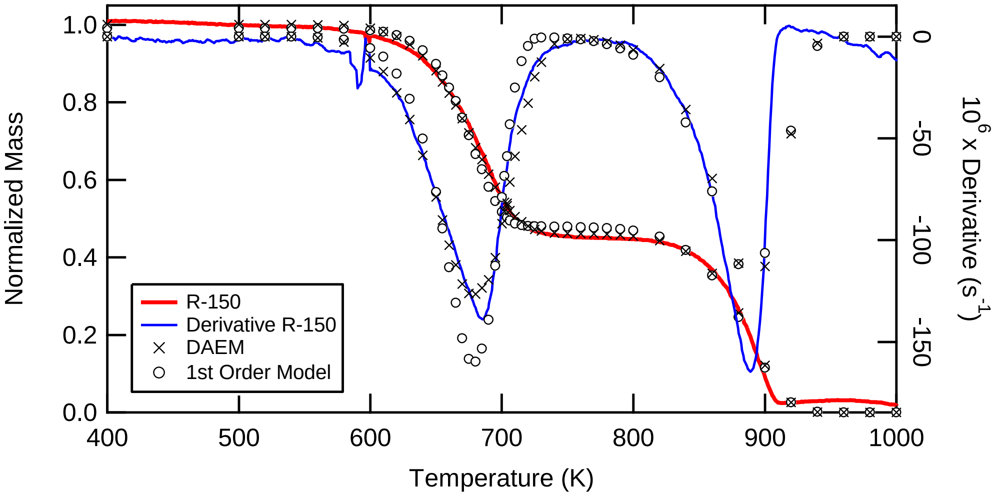

(a) Sample R-150

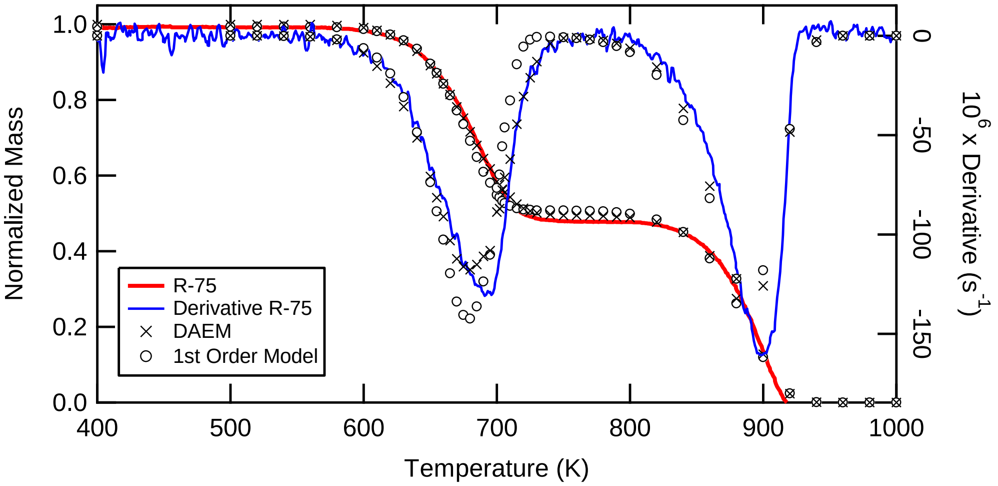

(b) Sample R-75

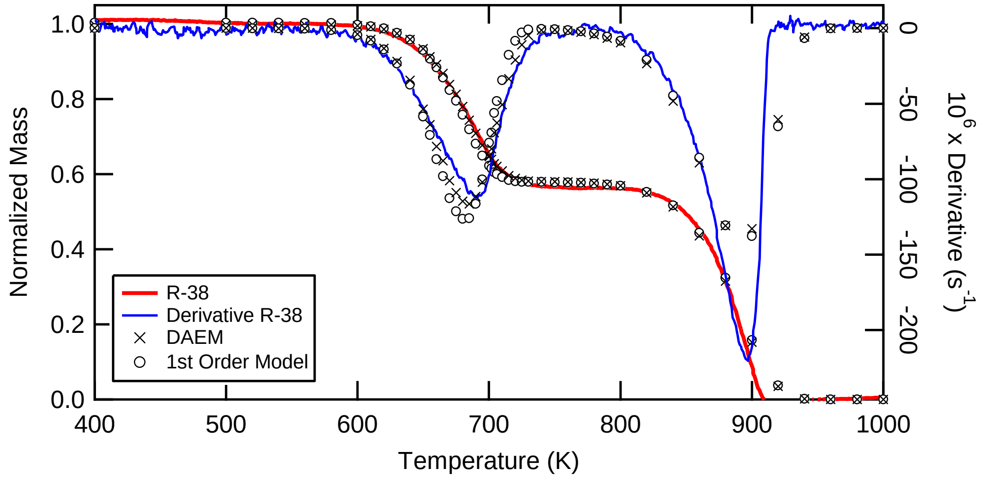

(c) Sample R-38

Figure 28. Comparison of model predictions and experimental data of both mass vs temperature (LHS) and derivative vs temperature (RHS) of each sample at 1K/min, 1 bar conditions.

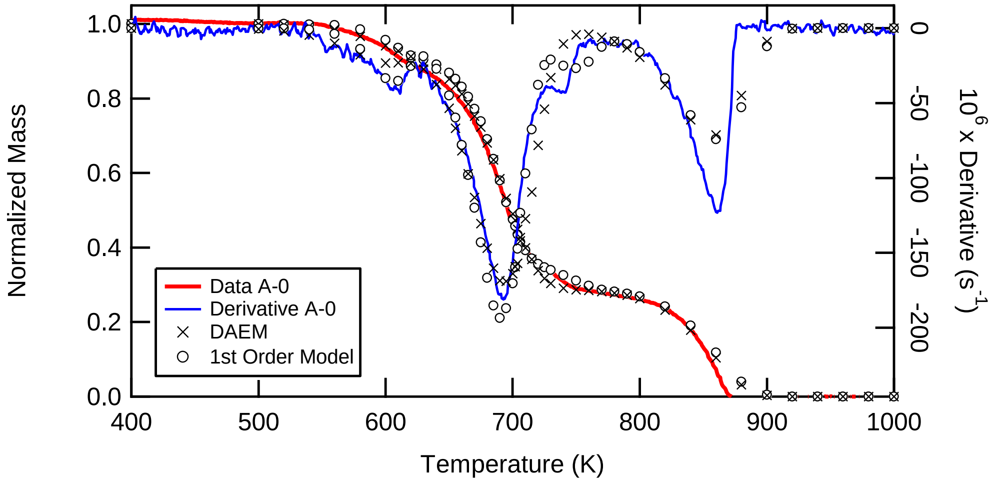

(d) Sample A-0

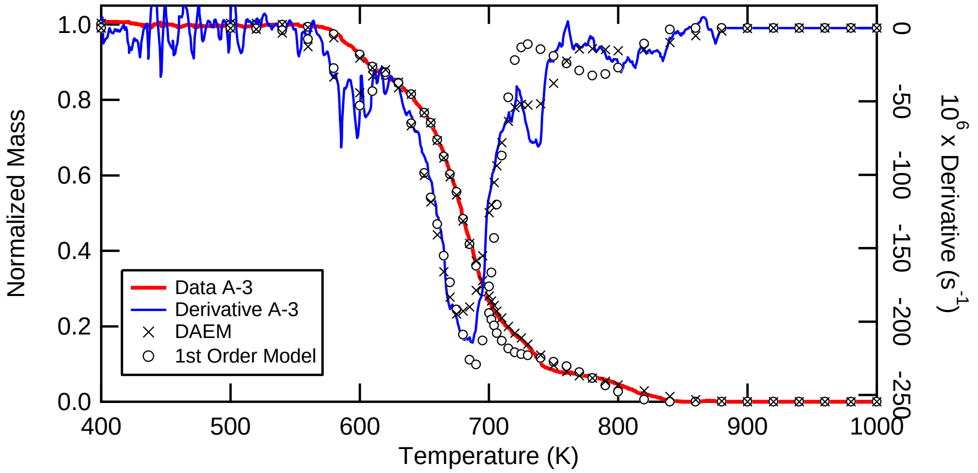

(e) Sample A-3

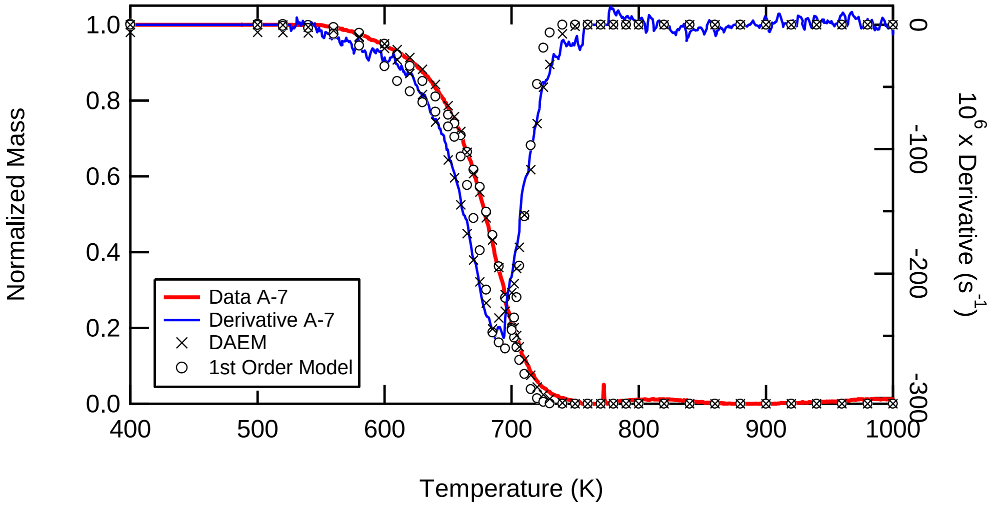

(f) Sample A-7

Figure 28. Continued.

As can be seen from Figure 28 both models describe the reaction that occurs between about 600 K and 800 K adequately but in each case the DAEM model was statistically better according to the F test and Equation 15.

Figure 29 shows the confidence region for the Sample A, the optimal 1st order model parameters determined in this study, and several reported Green River Oil Shale parameters for the same model. The parameters all lie within or very close to the statistical confidence region and would each predict fairly well the pyrolysis and generation of oil shale at heating rates on the order of degrees per minute.

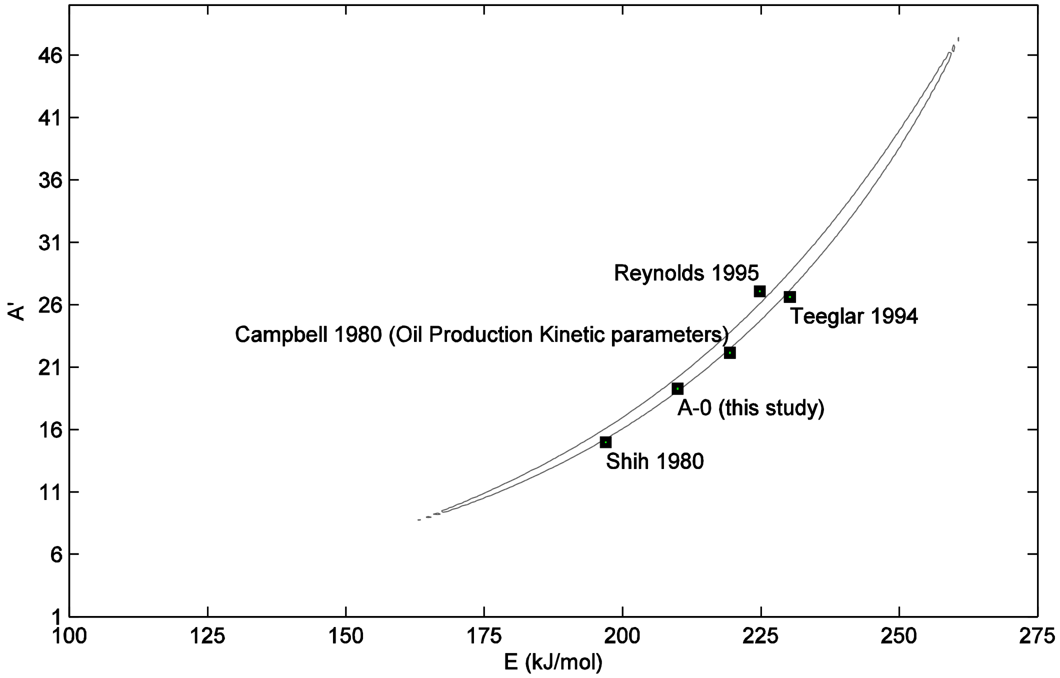

Figure 29. Statistical confidence region for sample A-0 with values from other researchers.

Despite the conclusion that the DAEM is statistically better, note the low magnitude of the distribution parameter, σ, in Table 8. This would suggest that a first order model is indeed sufficient. Figure 30-Figure 32 are plots of the parameters in Table 8 with confidence regions determined around each parameter by Equation 16. The resulting ideal parameters and confidence regions are seen here in Figure 30-Figure 32. For ease of visualization, a normalized value A' is used in these plots, defined as:

$$A'^{10} = A, \tag{17}$$

or

$$A' = 10^{(\log A)/10} \tag{18}$$

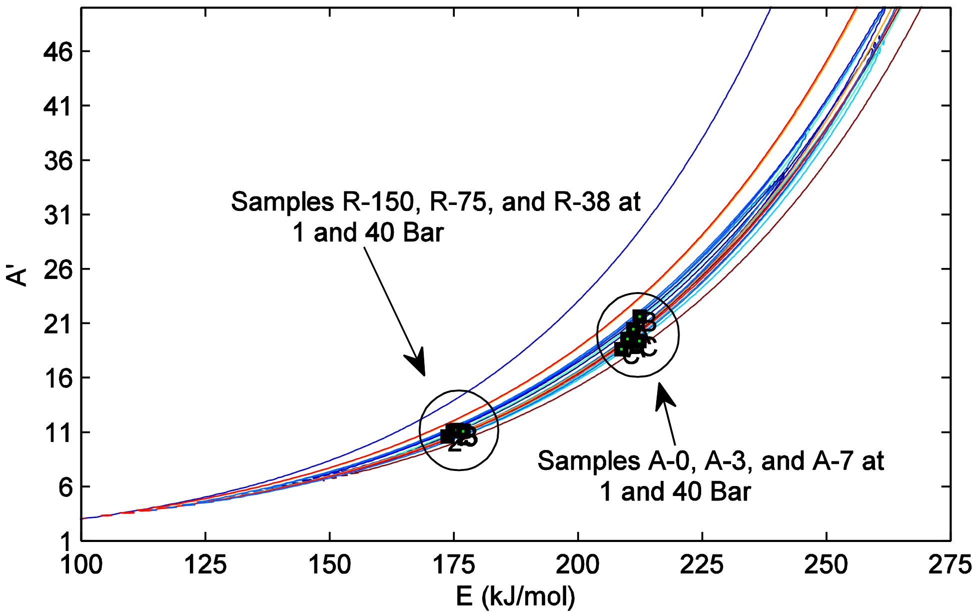

Figure 30. Confidence regions determined for the 1st order model for 1 Bar vs. 40 Bar with optimal points indicated.

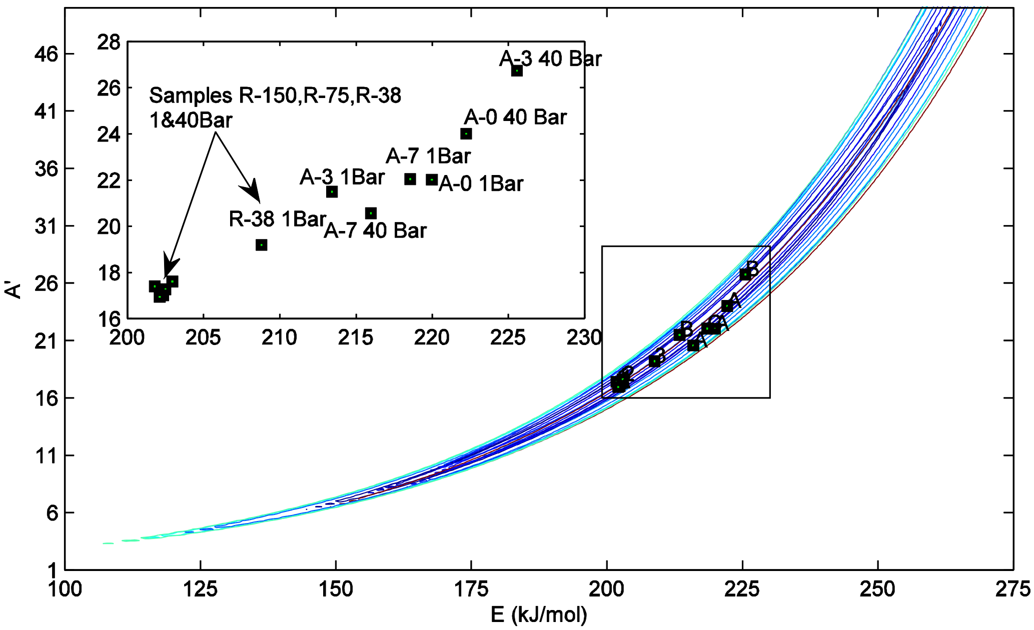

Figure 31. Confidence regions determined for the DAEM for 1 Bar vs. 40 Bar with optimal points indicated.

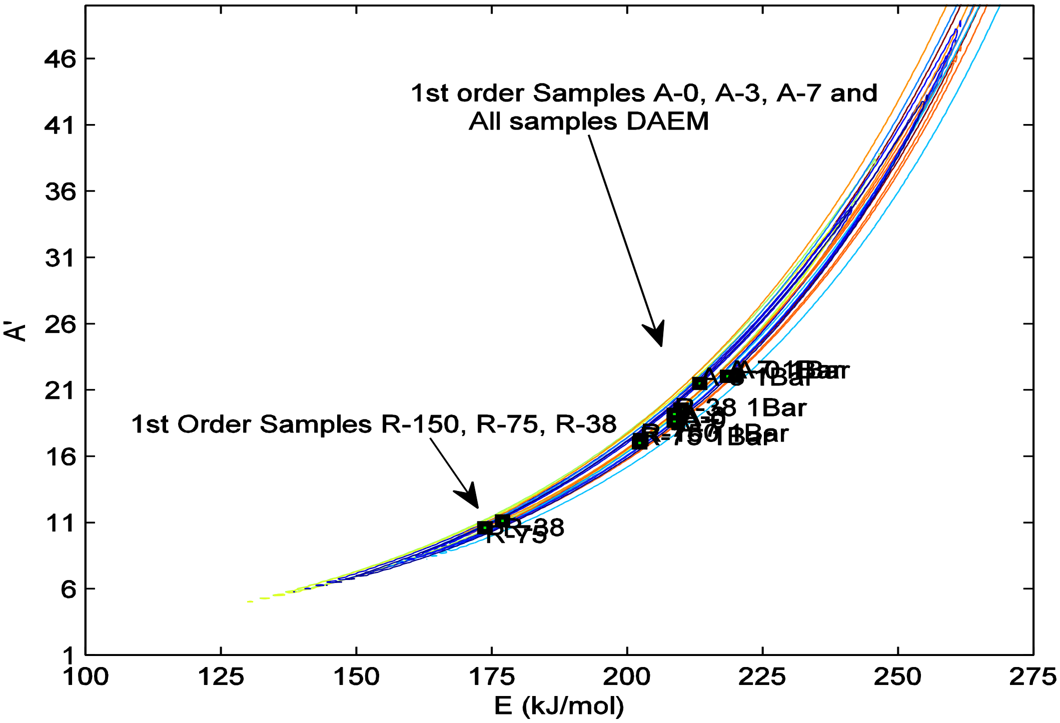

Figure 32. Confidence regions determined for the 1st order model vs. the DAEM at 1 Bar optimal points indicated.

Figure 30 shows the comparison between the six samples at the two pressure levels for the first order model. Note how the 40 bar data have much larger confidence regions. This is a result of the much larger noise in the 40 bar data. Despite the noise the ideal parameters for the different cases lie within each other's confidence regions indicating that the difference in the parameters is not statistically significant. This conclusion comes despite the numerical differences between Samples R-150, R-75, and R-38 and Samples A-0, A-3, and A-7. There is a marked decrease in the magnitude of the kinetic parameters for Samples 1-3. Application of the parameters from Samples A-0, A-3, and A-7 to Samples R-150, R-75, and R-38 visually shows a poorer fit. The fact that they lie within each other's confidence regions could change if additional experiments allowed for smaller confidence regions, as explained above.

Note how the pressure may have a slight but not significant effect (Figure 31) for the DAEM model and really no effect for the 1st order model (Figure 30). This means at pressures expected at geological conditions or in many industrial situations the kinetic parameters determined at atmospheric conditions are sufficient. The stage of demineralization also does not appear to have a statistically significant effect, as indicated by comparing samples A-0, A-3, and A-7 in Figure 30 and Figure 31. This means that demineralization is not necessary for determination of kinetic parameters and that the oil product is not interacting with the minerals. This analysis has shown that the pressure effect is negligible for the organic reaction rate coefficients. Figure 33 shows the TGA trace for the same sample at the two different pressures. The slight difference in the first peak of the two curves is really within the noise range for the 40 bar data and is not significant. It would appear from Figure 33 that the mineral reaction (second peak) was affected by pressure but the mineral decomposition reaction was not studied as part of this work.

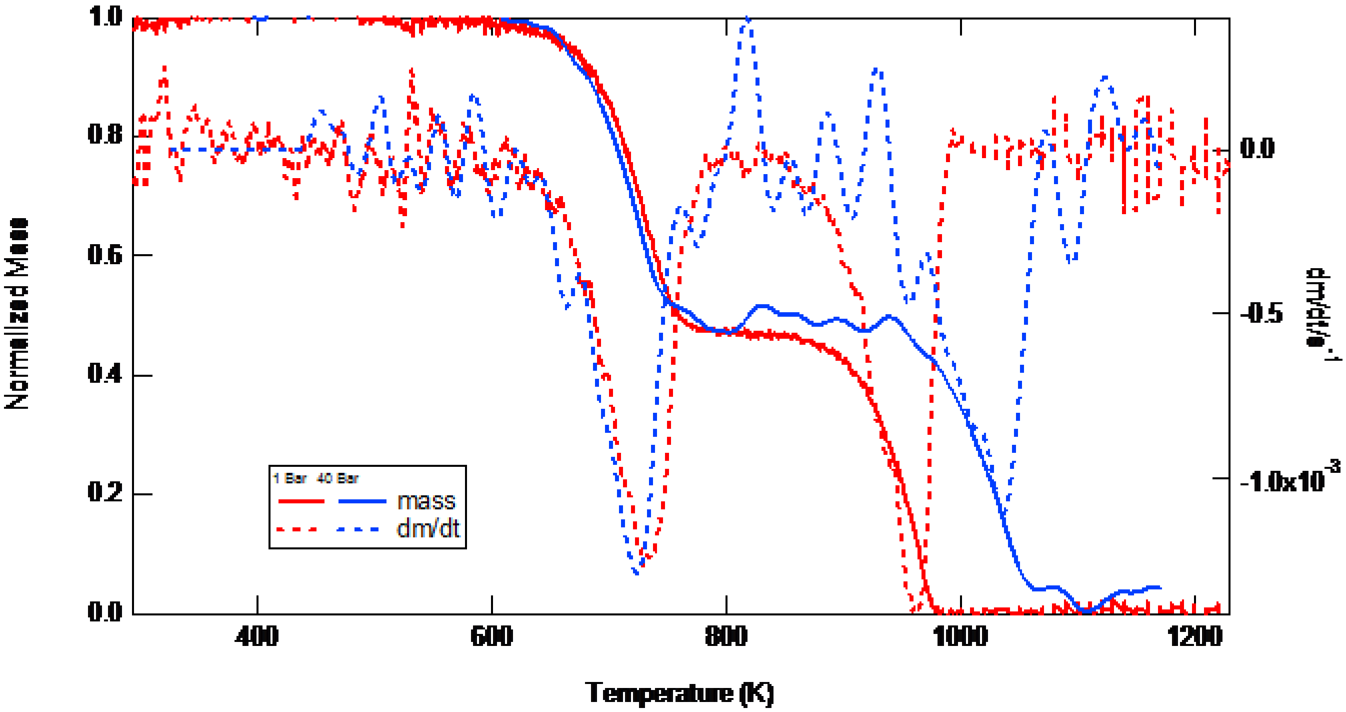

Figure 33. Comparison of mass and derivative traces for sample R-150 at 1 Bar and 40 Bar.

The DAEM becomes a first order model as the distribution approaches zero. The DAEM is statistically better than the 1st order model in most of the cases considered in this work, but the overlap in the parameter confidence regions would indicate that it is only a small improvement over the 1st order model. The result that a 1st order model fits the data is similar to a result determined by Campbell and coworkers (1978) who examined a Colorado oil shale from the Green River Formation. It should be noted that the samples obtained from the surface showed a lower magnitude for the kinetic parameters (approximately 35 kJ/mol lower for the first order model) than those from the core sample. The surface samples also showed a different TGA profile with only two distinct reactions instead of four. This re-emphasizes the fact that kinetic parameters can differ with sample composition and or oxidation. It is possible that differences might occur in the organic matter of the two samples despite both originating from the Green River formation. Despite the differences both the oil shale and the kerogen kinetic parameters show very similar confidence regions and that gives assurance that kinetic parameters obtained from one portion of the formation can be used to adequately represent the larger formation.

The kinetics obtained from the three size-graded samples agreed well with each other. The range for the 1st order on the kinetic parameters was 3.2 kJ/mol for the activation energy, with only a 38% variation in A-0 at atmospheric pressure and about a 10% variation in A-0 at 40 bar pressure. The parameters obtained for the DAEM model showed very little distribution, with σ on the order of 1.9-4.4 kJ. The improvement for the DAEM over the 1st order model was statistically significant in each size-graded case, but visually only showed minor differences. Since the kinetic parameters did not change much for the size-graded samples, it was assumed that mass transfer resistances at these heating rates were small.

The kinetics obtained from the successively demineralized samples also agreed well. The activation energy only spanned 3.6 kJ for this set of experiments. This range of E is within the experimental error, and was compensated by the pre-exponential factor. The improvement by using the DAEM for the demineralized series was much smaller and not statistically significant for Sample A-0 at 1 bar and Sample A-3 and A-7 at 40 bar. The F value determined according to Equation 15 was only barely above the critical F value for the cases where the F-test showed that the DAEM was statistically better for Samples A-0, A-3, and A-7.

6.6. Discussion about Mineral Effects on the Kinetic Parameters

It is possible that the mineral decomposition interfered with the kinetic parameters observed in this study. This interference could be in the form of parallel mass loss from minerals which may have obscured the kinetic results. To explore this effect, the kerogen retort was used to pyrolyze a sample of A-0.1600 and then separately sample A-7.PRO under the same conditions as the TGA. The effluent from the kerogen retort was fed into a mass spectrometer to determine the composition of the gas. Assuming that the CO_2 evolved was due to mineral decomposition, a rough comparison was made between the m/z = 44 and the m/z > 50. This comparison gave a rough estimate of the relative temperatures of the decompositions of the minerals vs. the hydrocarbons and a rough estimate of relative magnitudes of mass loss from each of the two components.

The hydrocarbons were the dominant signal for the A-7.PRO sample and though the measured relative magnitudes were closer for the A-0.1600 sample, when the condensed product is considered then the masses differ by a significant amount. This means any mineral decomposition that occurred in the temperature range would have been a negligible amount compared to the hydrocarbon. Though the comparisons of mineral mass loss to organic mass loss differs by a substantial amount, relative magnitudes could not be accurately determined because there was so much hydrocarbon product that some hydrocarbons had to be condensed that would otherwise have clogged the system. Therefore, most of the heavier products were condensed prior to the gas analysis. Because of the condensed hydrocarbon product, the mass of the hydrocarbon release was in fact many times larger than the amount indicated in the mass spectrometer data.

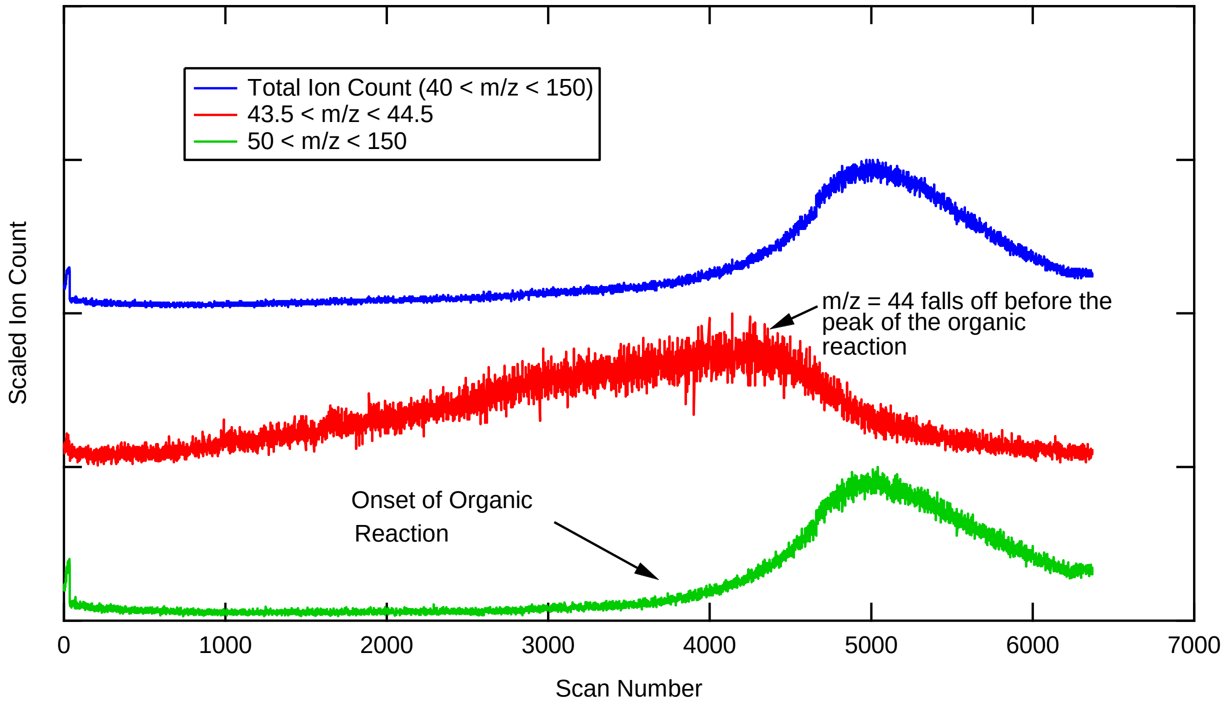

Figure 34. Pyrolysis gases from sample A-7.PRO (the kerogen) with the total ion count on the top, the m/z=44 (CO2) in the middle, and the heavier hydrocarbons on the bottom. Because of a constant heating rate the abscissa can be thought of as temperature.

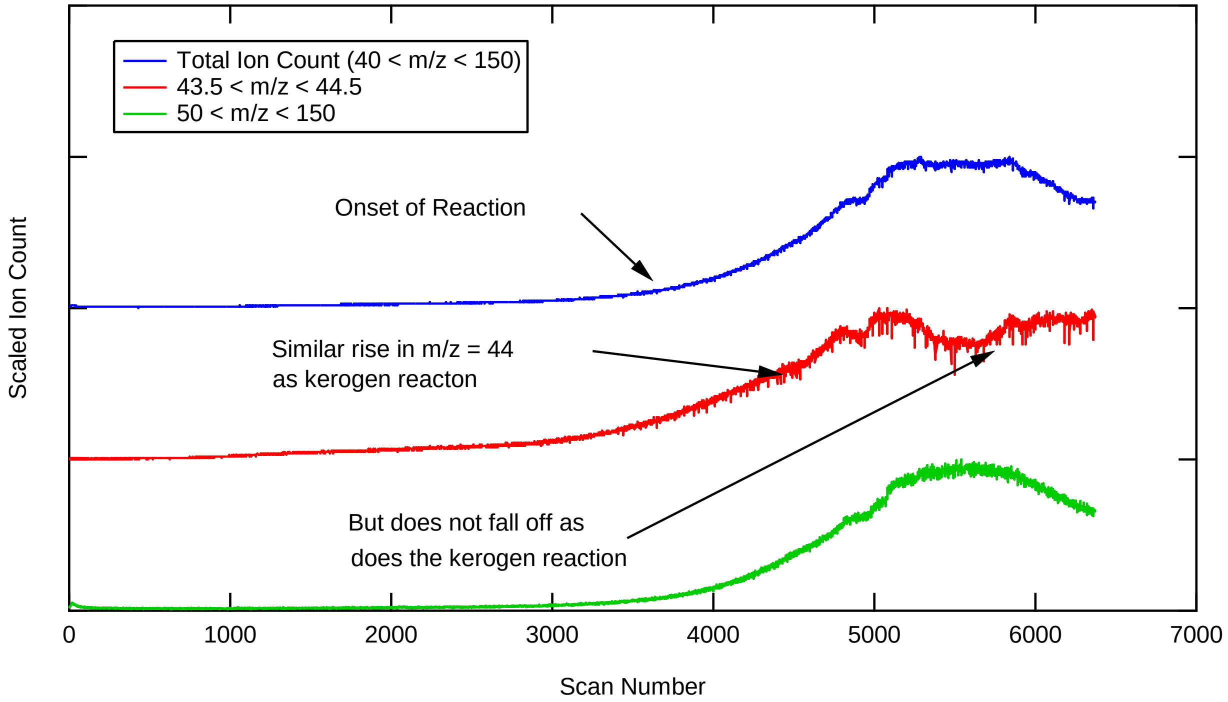

Figure 35. Pyrolysis gases from sample A-0.1600 (oil shale) with the total ion count on the top, the m/z=44 (CO2) in the middle, and the heavier hydrocarbons on the bottom. Because of a constant heating rate the abscissa can be thought of as temperature.

Figure 34 and Figure 35 both show pyrolysis gases with the total ion count on the top, the m/z=44 (CO_2) in the middle, and the heavier m/z (hydrocarbons) on the bottom. Because of a constant heating rate the abscissa can be thought of as temperature though the two are not exactly the same because of when the data recording was initiated. The heating rate was 10K/min and the pressure was atmospheric. The ion counts were scaled both for easy display and because the ratio of the relationship was obscured (most of the hydrocarbons (~60%) of the DAF mass was condensed as a hydrocarbon product). The ratio was not entirely useless because even after the condensation of most of the products the larger ion masses were within an order of magnitude of the CO_2. This means that some of the larger ions were being detected in the same numbers as the CO_2. This is similar to thermogravimetric apparatus evolved gas analysis (TGA-EGA).

The levels of CO_2 were both higher and were sustained through temperatures where the hydrocarbons were released for the oil shale sample. Conversely, CO_2 release during the organic reaction temperatures were not observed for the A-7.PRO sample (Figure 34) though the CO_2 release occurred earlier. Because the kinetic parameters for the oil shale and the kerogen agreed, the effect of the minerals was kinetically insignificant. The insignificance of the minerals may stem from the fact that the relative magnitude of the gas yield from the minerals that react at the same temperature as the organics was indeed very small.

6.7. Conclusion

Crushed samples of Green River oil shale were pyrolyzed at heating rates from 1 to 10 K/min at pressures of 1 and 40 bar and temperatures up to 1000°C. Two major mass release peaks were observed corresponding to kerogen pyrolysis and carbonate decomposition for the size graded sample. The demineralized sample came from a different location in the Green River formation and showed four peaks for sample A-0. Pyrolysis of samples from subsequent stages of demineralization showed three peaks for A-3 and one peak (with a small shoulder) for A-7. The transient pyrolysis data were fit with a first-order model and a progressive Distributed Activation Energy Model (DAEM). An F-test was used to determine confidence regions and compare the kinetic parameters among the oil shale and demineralized samples, between the two pressure levels, and between the models.

The activation energies determined ranged from 173 to 226 kJ/mol, with most values around 200-220 kJ/mol. The kinetic coefficients determined for oil shale and the demineralized samples were statistically the same. Only small differences in kinetic coefficients were seen in the size-graded samples, indicating negligible mass transfer resistances at the heating rates used in these experiments. The difference in the kinetic coefficients for the pyrolysis at 40 bar was small (~3 kJ/mol) and not statistically significant. The first-order and DAEM models were also shown to be statistically different, but a visual inspection reveals that both models performed well. The largest effect observed was between the parent samples. Those samples obtained from nearer the surface showed lower magnitude for the kinetic parameters than those obtained from a core sample. Despite the differences the kinetic parameters for the two sample sources were within each other's confidence regions so there is no statistically significant difference between the two.

7. Analytical Chemistry Results

7.1. Low Temperature Ashing

An estimate of the total organic carbon in the samples was obtained by low temperature ashing. It was necessary to use a low temperature ashing to reduce the amount of minerals decomposed which would obscure the result. This ashing was performed on the oil shale samples and their chars used in the oil shale retort to determine organic matter percentages. Table 9 shows the low temperature ashing results. The A-0.1600 oil shale (labeled 25°C) showed a moisture content of 1.6%, an ash content of 74.0%, and an organic content by difference of 24.4%. As the shale was pyrolyzed at higher temperatures, the ash content increased and the organic content decreased.

Table 9. Low temperature ash tests performed on oil shale (A-0.1600), partially pyrolyzed oil shale from the oil shale retort (A-0.1600) and the A-7.PRO (last column only).

Final T in retort °C	25	422	438	445	452	461	523	25
As Received								*A-0.pro*
Moisture %	1.6%	0.2%	-0.1%	0.3%	0.1%	0.0%	-0.1%	3.4%
Ash %	74.0%	82.0%	85.3%	85.5%	87.3%	90.0%	92.5%	12.1%
Organic % (by difference)	24.4%	17.8%	14.8%	14.2%	12.6%	10.0%	7.6%	84.5%
Dry basis								
Ash	75.2%	82.2%	85.2%	85.7%	87.4%	90.0%	92.4%	12.6%
Organics	24.8%	17.9%	14.8%	14.8%	12.7%	10.0%	7.6%	87.5%
DAF Organic Release	0	34.1%	47.5%	49.5%	56.1%	66.2%	75.1%	

7.2. Oil Shale Retort

The results for the oil shale retort pyrolysis experiments described in section 4.1.2 were used to determine the evolution of the organic matter as a function of temperature. These results can either be viewed on an as received basis or a dry ash free basis as described in 4.2.2. The as received basis is useful for knowing absolute yield values but comparison to the kerogen becomes difficult. Normalizing based on organic content was therefore necessary. Also of note is that due to sample limitations no replicate experimental conditions were conducted; additionally, in two cases (422°C and 445°C) there was additional uncertainty due to sample being lost due to a possible technician error.

Figure 36 shows the yields of char + ash, tar, and light gas from the oil shale retort. The light gas yield was obtained by difference. Note how the gas yield is fairly level while the tar and the char seem to be inversely correlated. This result makes sense since what is called char is really all the unreacted matter, so as char yield decreases the sum of the tar and gas yields should increase. The gas yields were obtained by difference and seem to be constant. The gas yields being constant would indicate that most of the gaseous product was generated before 422°C. The yields and temperature are consistent with TGA traces generated on a related sample (see section 6.1). TGA traces for the A-0 oil shale showed about 6% evolved in the first mass peak. The interesting fact that arises from this result is that only small amounts of gas were generated during the temperature range associated with the evolution of the organics.

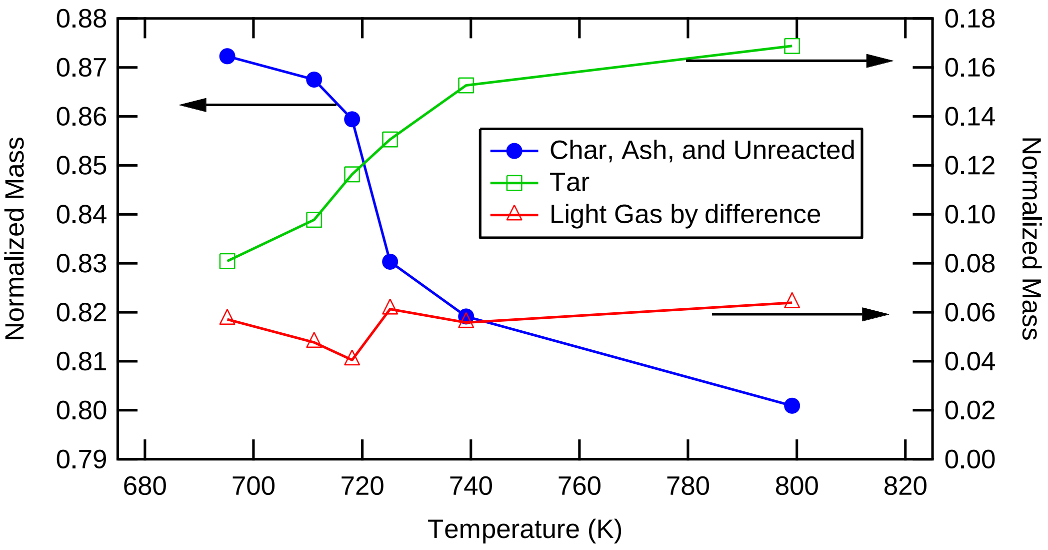

Figure 36. Measured and calculated yields from oil shale retort.

7.3. Kerogen Retort

The method for collecting the data with the kerogen retort was described in sections 4.1.3 and 4.2.3. It is known from ashing the "kerogen" sample that the demineralization process does not remove all the minerals. Therefore, in a similar fashion to the oil shale retort, using the process described in section 4.2.7, the kerogen retort data have been normalized to a dry ash-free basis. The mineral content of the demineralized kerogen was found to be 12.12% and the moisture content was found to be 3.42%.

The process of collecting the tar quantitatively as described in section 4.2.3 was very difficult, and several experiments did not have a reliable tar yield. Several problems were encountered. In a few cases the glass condenser was dropped, invalidating the tar yield even though the char yield was sound. In another case there was a visible and measurable presence of tar on the outlet filter. That case merited the exclusion of the tar data since it was impossible to know how much tar escaped. Both of these cases resulted in exclusion of the tar yield but inclusion of the char yield. A few cases, such as leaks in the system detected by a strong pungent odor in the lab, merited the exclusion of both yields since the pyrolysis data would be suspect if oxidation were allowed to occur. Even for the experiments where a “reliable” tar yield was obtained there was still visible scatter in the data. This scatter is possibly attributed to the error in the temperature measurement or other experimental limitations. The temperature measurements are a point of error because the thermocouple was only measuring the reaction gas temperature just down stream of the sample rather than the actual solid sample temperature. The precision of these measurements also suffered because the experiment had an imprecise method of stopping the reaction. The reaction was stopped (as described in section 4.2.3) by manually removing the retort from the furnace. If the procedure took longer than expected then the temperature would be different than expected. Another difficulty encountered was that at the highest two temperatures the reactor connections began to fuse together and damaged the reactor. Therefore only one experimental run was conducted at each of these temperatures. In the case of the highest temperature experiment a few sections had to be replaced due to connections becoming fused together.

Figure 37 shows the char and tar yields from kerogen retort. Also shown is the 1st order char pyrolysis model using parameters determined from A-7 pyrolysis in the TGA. The excellent agreement between the model and the char data gives confidence that mass transfer was not a major effect in the reactor. This comparison is also a validation of the model. Despite the scatter in the tar data seen in Figure 37 there was still a definite trend that described the evolution of the tar. As the char + amount of sample remaining decreased with increasing temperature the tar yeilds increased. The mass loss from the gas remained relatively constant meaning that the gas was lost early and then it was the tar that was lost at the higher temperatures.

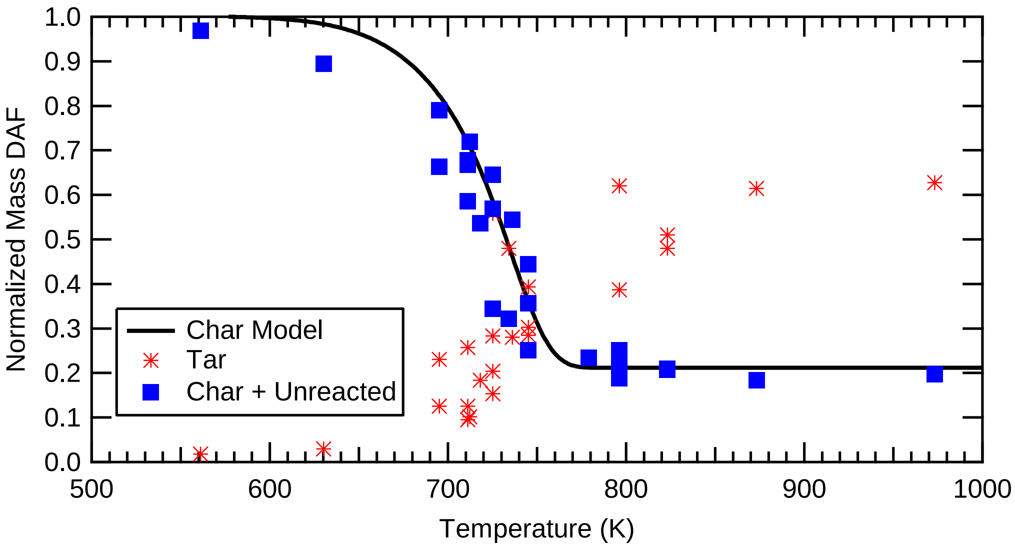

Figure 37. Char and tar yields from kerogen retort sample A-7.PRO with char pyrolysis model using parameters determined from A-7 values.

7.4. Comparison between TGA, Oil Shale Retort, and Kerogen Retort

It is useful to compare the char yields (i.e., un-reacted portions) from the different reactions. The char model determined from the A-7 TGA experiments at atmospheric pressure is compared to the oil shale retort data and the kerogen retort data in Figure 38. Note how the model predicts the aggregate data set quite well. Closer inspection shows that the oil shale retort slope is slightly shallower than the model and most of the points lie on the lower side of the model predictions.

One possible explanation for the shallower slope is that the particles are transport limited. Two transport limited situations could arise, mass transfer limited and heat transfer limited. In a mass transfer limited situation the concentration of the pyrolysis products near the surface will be approximately zero due to sweep gas and other experimental conditions while the concentration will build. This means that as the products are generated but do not escape as quickly. Some of the consequences are that the products will be seen as exiting at higher temperatures, resulting in a shift in apparent reaction temperature or that the products can undergo secondary reactions and re-incorporate into the parent sample. One result of mass transfer is to have an apparent decrease in the slope of the mass vs temperature curve. The shallower slope explanation would have to be coupled with another explanation for why the oil shale retort data were shifted to lower temperatures with respect to the data from the kerogen retort.

Another probable explanation is that there is more time required to cool the oil shale retort than the kerogen retort. Cooling data collected suggest that the kerogen retort was cooled from 550°C to 200°C in less than four minutes while the oil shale retort took a little more than 10 minutes. This means the sample continued to react during the cool down period in the oil shale retort. This continued reaction would have the effect of shifting the oil shale retort mass loss data points down at a given temperature. A third possible explanation is that the temperature measurement inside the oil shale retort (or the kerogen retort) is not an accurate measurement of the actual sample temperature. This is also probable since the reported temperature profile in the oil shale retort is an average of three thermocouple measurements. These measurements can differ by as much as 20°C. For the purposes of this work the cooling time and the temperature measurement inside the oil shale retort explanations are both assumed to contribute to the cause of the slightly lower oil shale retort data with respect to the TGA kinetics and the kerogen retort data.

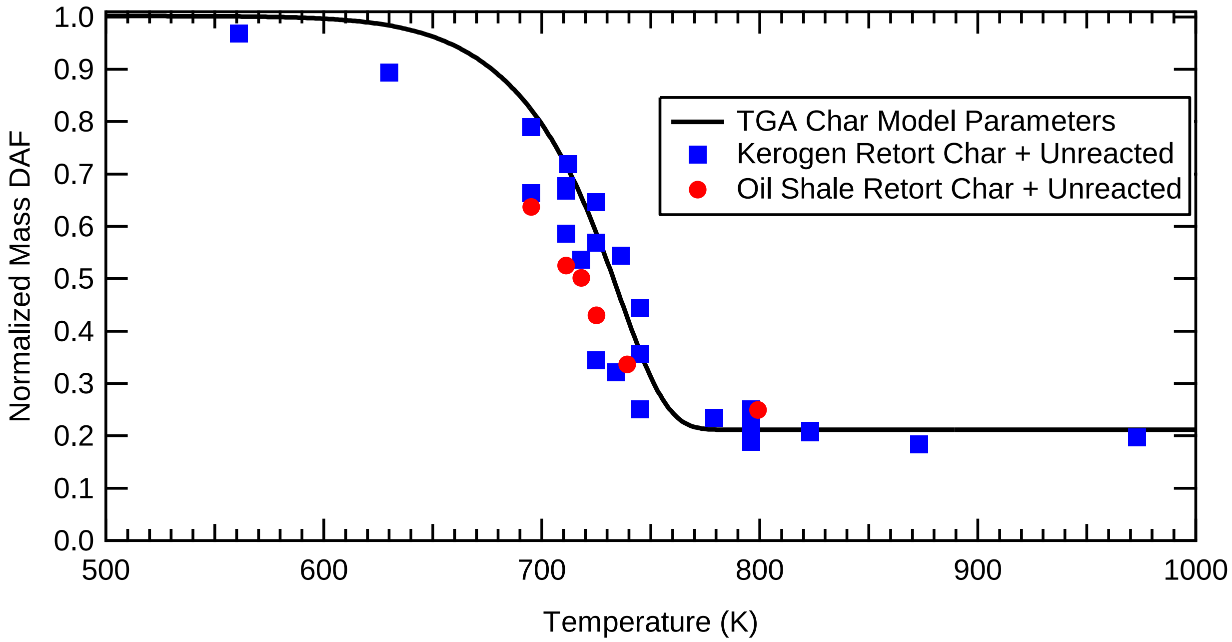

Figure 38. Comparison of kerogen retort, oil shale retort, and kinetics model from TGA. Samples were A-7.PRO, A-0.1600, and A-7 respectively.

7.5. X-ray Photoelectron Spectroscopy (XPS)

X-ray Photoelectron Spectroscopy (XPS) is a surface technique that is useful in determining the forms and relative abundance of certain atoms. XPS is one of the few techniques that can determine the mole fraction ratios of the different forms of heteroatoms, such as whether an element exists in a single bond or double bond. The XPS analysis is used here to determine chemical forms of nitrogen and oxygen. These two atoms appear in several forms and are in moderate abundance in the samples analyzed in this study.

7.5.1. Nitrogen Shifts

Table 10 contains some nitrogen shifts for forms of nitrogen adapted from work by Kelemen and coauthors (Kelemen et al., 1994) who collected the standards and determined the nitrogen shifts for each type of nitrogen found in the Argonne Premium Coals. Table 10 also contains some of the same compounds analyzed in this project at BYU. Shifts are corrected for a 284.8 shift for the carbon 1s peak. The compounds analyzed at BYU shown in Table 10 disagree slightly with those collected by Kelemen and coworkers by varying shifts. Four additional nitrogen compounds sublimated in the BYU XPS machine and could not be compared here.

Table 10. Nitrogen Shifts for various compounds. Table adapted from (Kelemen et al., 1994) with BYU data included.

Compound	Shift (Kelemen)	Shift (BYU)	Type of N
phenazine	398.7		pyridinic
poly(2-vinyl pyridine)	398.8		pyridinic
3- hydroxypyridine	398.8		pyridinic
Norharman	398.9		pyridinic
PIB amine	399.1		amine
l-aminopyrene	399.3	398.0	amine
Norharman	400.1		Pyrrole
2- hydroxycarabazole	400.2		pyrrole
dibenzocarbazole	400.2		pyrrole
l-hydroxyquinoline	400.3		pyridone
l-methyl-4-pentadecyl 2(1H)-quinolone	400.4		pyridone
6-(2,2-diphenyl-2-hydroxylethyl)-2Z(H)-pyridone	400.5		pyridone
1-ethyl-4methoxypyridinum iodide	401.3		quaternary
pyridinium 3-nitrobenzenesulfonate (pyridinium)	401.4	401.9	quaternary
3-hydroxypyridine N-oxide	403	402.0	N-oxide
9- hydroxy-3-nitroflourene	405.3		nitro
pyridinium 3-nitrobenzenesulfonate (nitro)	405.8		nitro
l-nitropyrene	405.9	405.7	nitro

Kelemen collected the data in Table 10 for use with the Argonne coals. In subsequent work Kelemen (Kelemen et al., 2002) applied the same data to oil shales as well. The resulting fits are shown in Figure 39. This particular set of fits gives the distribution of nitrogens for the Green River Oil Shale Kerogen shown in Table 11.

Table 11. Keleman (Kelemen et al., 2002) Green River oil shale nitrogen percentages.

Type of Nitrogen	XPS Shift	Area	Percentage of Nitrogens
Keleman Values (Kelemen et al., 2002)			
pyridinic	398.8		27%
amino	399.4		10%
pyrrolic	400.2		53%
quaternary	401.4		10%

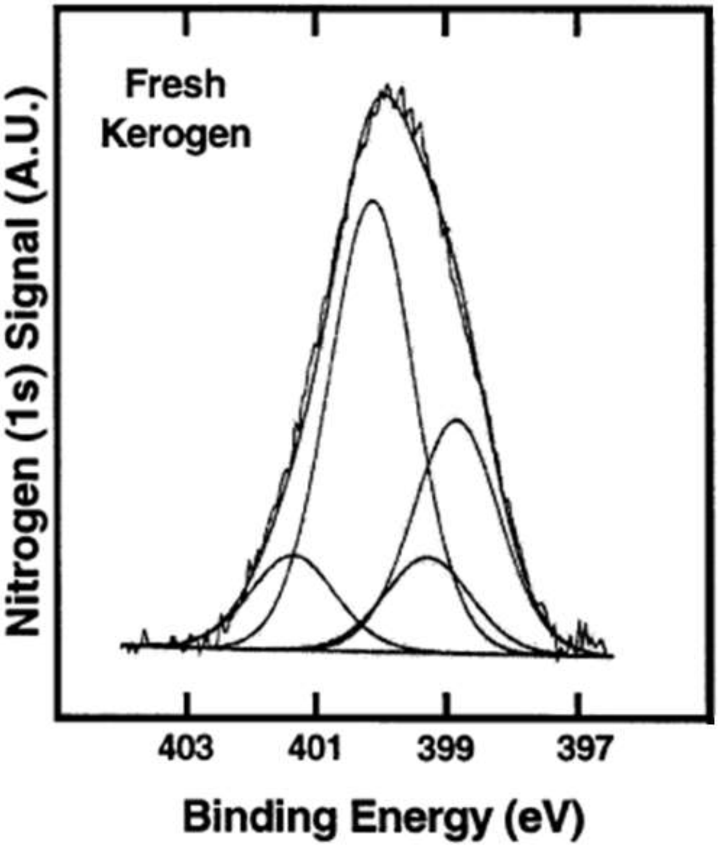

Figure 39. Nitrogen forms in Green River kerogen. Amounts shown in Table 11 and Table 12 (Kelemen et al., 2002).

7.5.2. A-7 and A-7.PRO Results

Utilizing the shifts for the standards listed in Table 10, the forms of nitrogen in a sample can be determined by curve fitting a mixed Gaussian/Lorenzian curve with a fixed shift but a variable area. The resulting area ratios represent the mole fractions on the surface. A solution first requires an a priori decision on the number of different allowable forms of the heteroatom. If that number is greater than one or two and the XPS trace in the shift includes overlapping peaks, generating some difficulty in determining a unique solution. The difficulty arises since the resulting fit is the sum of a few different curves each representing a different form of the heteroatoms. The solution can be constrained using known shifts and fixing a maximum allowable full width half maximum of the chosen reference peaks.

Using shifts similar to those determined by Kelemen and coworkers (2002) nitrogen forms and mole percentages were determined for the demineralized kerogen. The results are presented in Figure 40-Figure 41 and Table 12. The sample was analyzed two times in the XPS with the first run being done at the same time as several nitrogen standards, a few of which sublimated in the XPS vacuum chamber. The sample and the standards were also ground in the same mortar and pestle. It is thought that there was some cross contamination, as seen in Figure 40, which possibly could have come from these sublimated samples or improper cleaning of the mortar and pestle. Note how in Figure 40 there are two shoulders on either side of the sample. These are not observed in published data for Green River Kerogen, nor observed in other geological organic matter like low ranked coals, and are not observed in the subsequent runs shown in Figure 41 or Figure 42.

Figure 41 and Figure 42 show two different possible nitrogen distributions. The first curve fit shown in Figure 41 allowed the FWHM (full width half maximum) to float as an adjustable parameter. This result shows nearly equal parts of pyridinic (398.6 ev) and pyrrolyic (400.2 ev) nitrogen while there is less quaternary nitrogen (401.4 ev). The second distribution possibility shown in Figure 42 fixed the FWHM to be less than 1.8 ev, similar to the result by Kelemen. As shown in Table 12, the resulting curve fit required four nitrogen species to resolve the curve and match more closely the results by Kelemen (2002), as well as what is to be expected from an organic fuel. The results are presented in Table 12.

Table 12. Nitrogen percentages values determined by Keleman (Kelemen et al., 2002) and those for A-7.PRO based on a floating FWHM or a fixed FWHM.

Type of Nitrogen	XPS Shift	Area	Percentage of Nitrogens	Per 100 C
Keleman Values (Kelemen et al., 2002)				
pyridinic	398.8		27%	
amino	399.4		10%	
pyrrolic	400.2		53%	
quaternary	401.4		10%	
Floating FWHM				
pyridinic	398.8	5720	39.7%	0.87
amino	399.2	0	0.0%	0.00
pyrrolic	400.2	5481	38.1%	0.83
quaternary	401.4	3202	22.2%	0.48
Constrained FWHM				
pyridinic	398.8	4583	30.1%	0.66
amino	399.2	1033	6.8%	0.15
pyrrolic	400.2	6581	43.2%	0.94
quaternary	401.4	3021	19.9%	0.43

The kerogen used in this study has similar nitrogen percentages to the distributions determined by Kelemen and coworkers (2002) if the same shifts and full width half maximums were used. If the full width half maximums were not constrained then the distribution showed more pyridinic and no amino nitrogen functionality as seen in Table 12. The constrained peak location and full with half maximum XPS results for the kerogen used in this study are recommended.

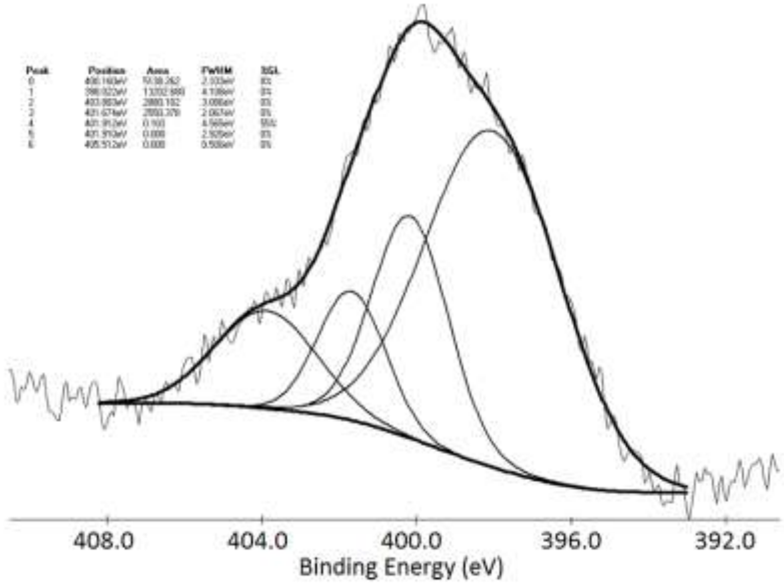

Figure 40. Nitrogen shifts for A-7.PRO collected as a replicate (it is suspected that this sample was contaminated).

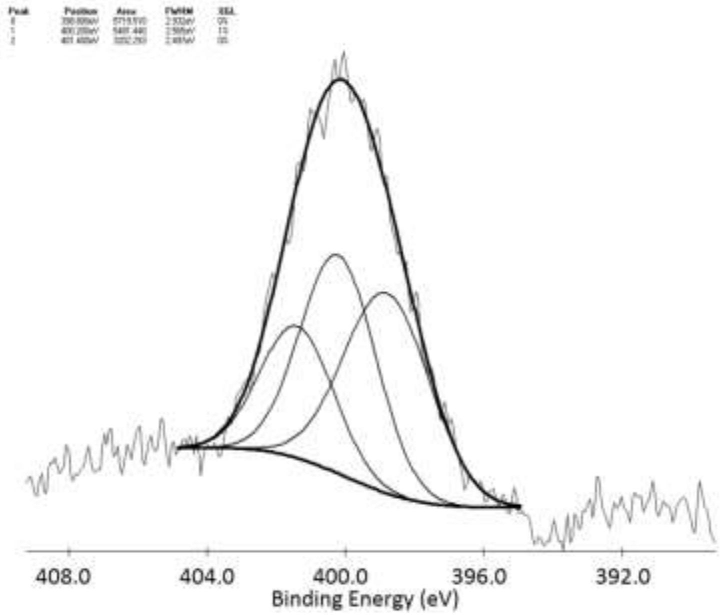

Figure 41. Nitrogen shifts allowing FWHM to float for A-7.PRO sample.

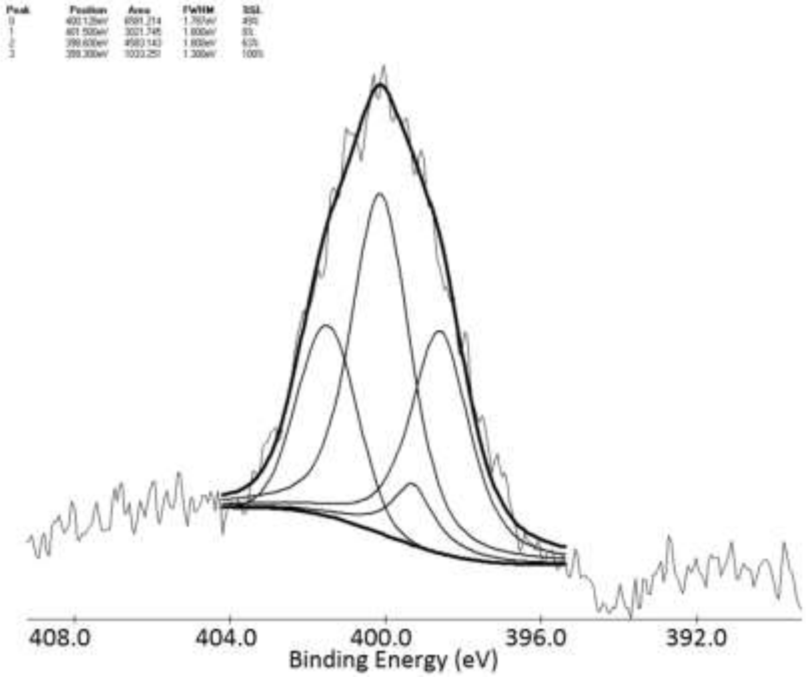

Figure 42. Nitrogen shifts for fixed FWHM values for A-7.PRO sample.

7.5.3. <u>Oxygen</u>

Oxygen functionality can also be assigned through XPS data but it must be done indirectly. This is described more fully in section 4.2.4. The A-7.PRO carbon data showed a peculiar hump on the low binding energy side. This shift (seen in Figure 43) corresponds to carbides, as seen in Figure 3. A quick survey of the literature revealed that this type of carbon bond is not seen in other Green River samples or any samples for that matter. This leads to the conclusion that the carbide sample was most likely artificially introduced. Ignoring the peak centered about 280 ev, this sample gives a distribution as shown in Figure 43. The principal peak corresponds to the C 1s peak centered at 284.8 ev with at least two carbon oxygen bond types. These two shifts are indicative of Carbonyl (C=O, 287.5 ev) and Carboxyl (O-C=O, 289.0 ev) groups. There is a third shift that corresponds to the ether/hydroxyl groups (C-O, 286.3 ev) that is difficult to resolve but can be determined by subtracting the two aforementioned groups from the total organic carbon. The mole percentages for the carbon oxygen functionalities are listed in Table 13.

Table 13. Carbon-oxygen mol percentages as determined by XPS

	Shift (e.v.)	area	mol %
Cabides	280.7	5288	14.1%
Aromatic and Aliphatic Carbon	284.7	29842	79.8%
Carbonyl (C=O)	287.5	972	2.6%
Carboxyl (O-C=O)	289	1289	3.4%

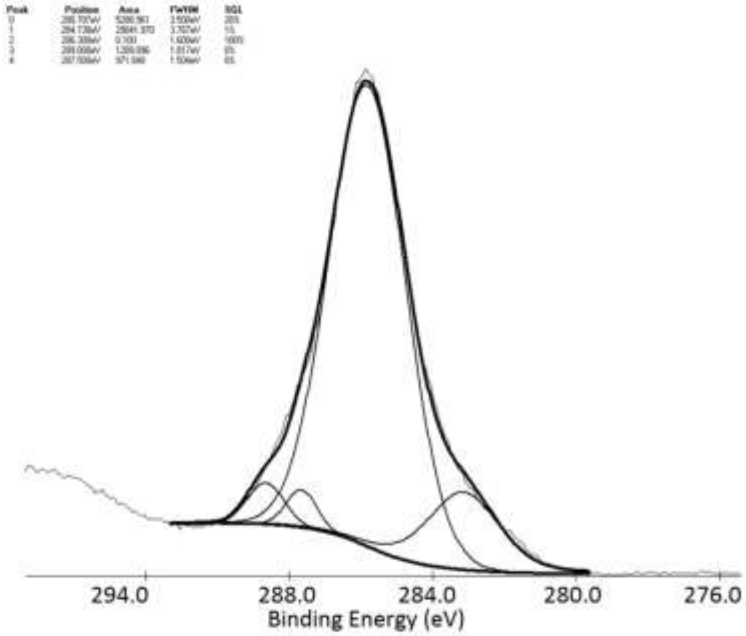

Figure 43. Carbon XPS region for A-7.PRO to determine oxygen functionality.

The presence of carbides was a little surprising and no explanation has been found to adequately describe this result. Carbide is not commonly found in kerogen and related samples.

Until further evidence supports the presence of carbides in the kerogen used in this study it is suggested to not include carbides in models of kerogen.

7.6. CHNS

Determining an elemental composition including total organic carbon is a difficult task because of the mineral matter. As described in section 4.1.8 and 4.2.8 the data were acquired by a Leco® CHNS machine. The average CHNS values for the kerogen and the subsequent chars are listed in Table 14. As expected the hydrogen steadily decreases from the parent coal to the completely reacted sample. The carbon stays approximately equal since the major products as seen in section 7.8 are hydrocarbons while the hetroatoms increase if a comparison is made of the kerogen and the char generated at the highest temperature.

Table 14. DAF CHNS percent values on a demineralized sample and its chars generated in the oil shale retort at six temperatures for an average of 3 replicates with standard deviation included

	C		H		N		S		O	
	Avg.	stdev	Avg.	stdev	Avg.	stdev	Avg.	stdev	Avg..	stdev
A-7.PRO	72.14	0.29	8.66	0.05	2.26	0.01	2.58	0.37	14.36	0.48
A-7.PRO Char 422°C	80.34	0.73	8.04	0.13	2.70	0.01	2.05	0.06	6.87	0.80
A-7.PRO Char 438°C	79.44	0.98	7.74	0.09	2.76	0.02	2.12	0.05	7.94	0.95
A-7.PRO Char 445°C	80.91	1.03	7.83	0.06	2.94	0.09	1.95	0.26	6.37	1.00
A-7.PRO Char 452°C	76.34	0.40	5.68	0.04	3.11	0.02	3.06	0.09	11.81	0.37
A-7.PRO Char 461°C	77.25	1.27	5.88	0.16	3.12	0.02	2.75	0.04	11.00	1.43
A-7.PRO Char 523°C	69.93	0.59	2.51	0.06	3.35	0.02	3.70	0.11	20.52	0.76

7.7. *Comparison of N and O determined from XPS and CHNS Analyses*

The XPS and the CHNS analyses both give estimates of oxygen and nitrogen content. The XPS is a surface technique while the CHNS is a bulk technique. The CHNS analysis gives a nitrogen content for the A-7.PRO of 2.69 nitrogens per 100 carbons while the XPS shows a 2.31 nitrogens per 100 carbons. The oxygen compared on the same basis shows for CHNS 15 oxygens per 100 carbons while the XPS is somewhat higher at 22 oxygens per 100 carbons. This is summarized in Table 15 which was constructed as an average of available repeatable data. The XPS data are an average of two points except the sulfur which is only one data point. All the CHNS data are an average of three points. The CHNS instrument determines the oxygen by difference assuming that there are only five elements (CHNSO), while the XPS is a surface technique only. The CHNS values were dry ash-free (DAF) and the oxygen was determined by difference so minerals were not an issue. The XPS instead determined the oxygen directly and minerals would have contributed some to the oxygen. The CHNS values are recommended as the absolute quantities of each element for use in a model with the approximate distributions of functionalities determined from the XPS. Further research is needed into the sulfur and oxygen percentages.

Table 15. Comparison of XPS and CHNS for A-7.PRO on a per 100 carbon basis

	XPS	CHNS
C	100	100
H	N.A.	143.1
N	2.31	2.69
S	0.59	1.23
O	22.1	14.9

N.A. means not available

7.8. GC/MS

Mass spectrometry (MS) and gas chromatography (GC) were used to collect chemical structural data and confirm which reaction was indeed the organic reaction on the aforementioned kinetic scheme. The equipment and methods are described in sections 4.1.5 and 4.2.5, respectively. Table 16 is a table of selected identified peak for the gas chromatographs of the tars generated in the Kerogen Retort (shown in Figure 44) from the A-7.PRO sample.

Table 16. Selected identified peaks from Figure 44.

Time (min)	Compound	Time (min)	Compound
4.54	Cyclopentanone	19.30	2-tridecanone
5.03	1-octene	19.46	1-pentadecene
5.28	octane	19.63	pentadecane
6.94	2-methylcyclopenatnone	21.10	1-hexadecene
7.31	1-nonene	21.26	hexadecane
7.57	nonane	22.66	1-heptadecene
8.40	trans-2-none-ol	22.81	heptadecane
8.61	4-isopropyl heptane	22.96	Pristine
8.67	mw= 124	24.13	1-octadecene
8.85	phenol	24.26	octadecane
9.22	2-octanone	25.53	1-nonadecene
9.62	1-decene	25.65	nonadecane
9.87	decane	26.86	1-eicosene
11.83	1-undecane	26.97	Eicosane
12.06	undecane	28.13	1-henicosene
13.62	2-decanone	28.23	henicosane
13.91	1-dodecene	29.34	1docosene
14.14	dodecane	29.43	docosane
15.63	2-undecanone	30.54	1-tricosene
15.88	1tridecene	30.64	tricosane
16.00	trans-2-tridecanal	31.86	1-tetracosene
16.09	tridecane	31.97	tetracosane
17.73	1-tetradecene		
17.91	tetradecane		

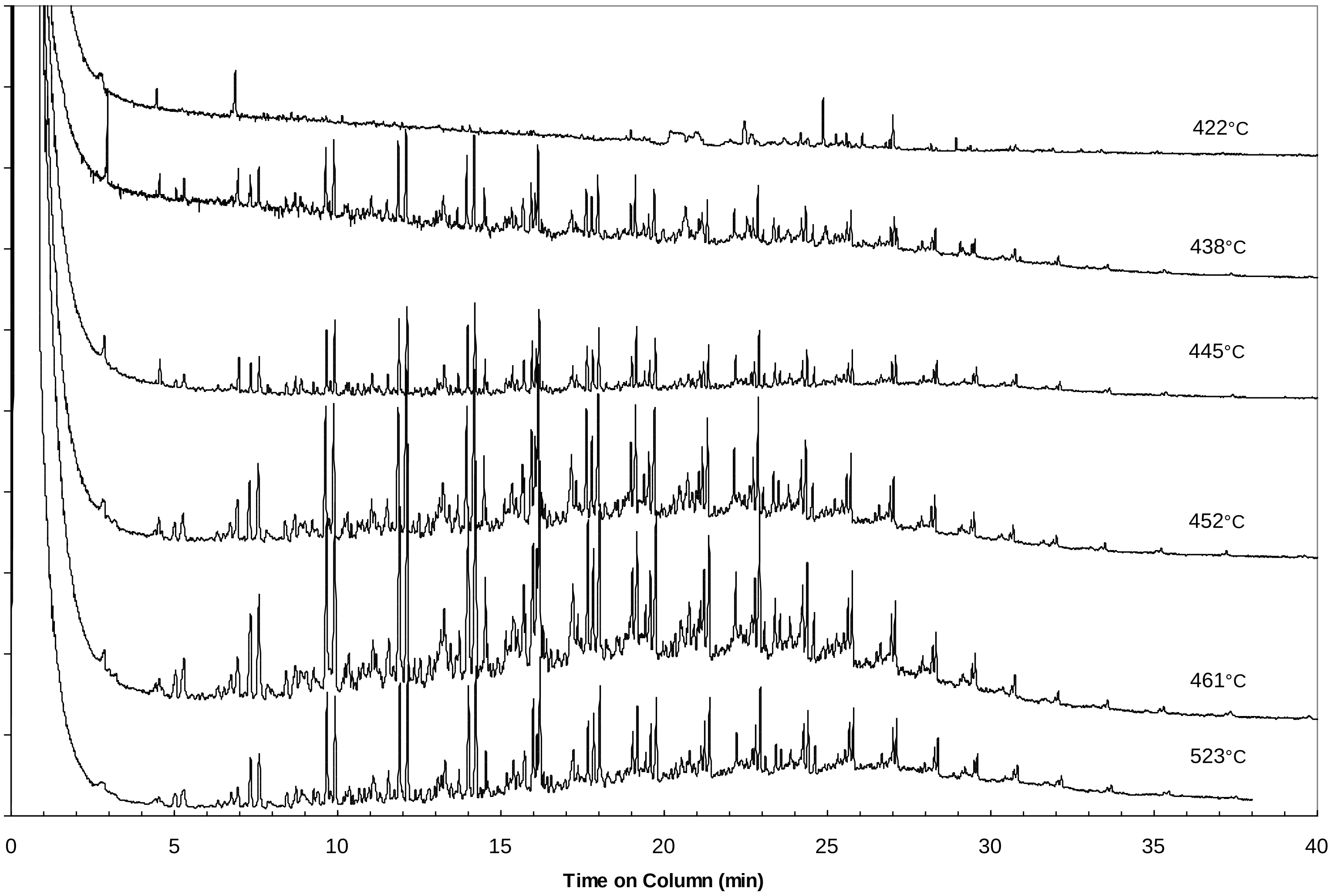

Figure 44. Gas chromatograms of tars from the A-7.PRO kerogen generated using the kerogen retort-ordered by final temperature

Of interest are the similarities between the samples. These tars are collected as a cumulative sample so any compounds generated at lower temperatures would also be present at higher temperature, in addition to the compounds generated at higher temperatures. Therefore, any compounds present in the 438°C sample should also be present in the 523°C sample, but some compounds present in the 523°C may not be present in the 438°C sample. The 422°C sample is shown here has some column bleed but relatively few compounds compared with the others.

The biggest change between the 438°C and the 523°C is the addition of some irresolvable compounds at the higher temperature, but the main peaks are the same. Among the prominent features shown in Figure 44 and listed in Table 16 are 1-alkene/alkane pairs, isoprenoids, some alcohols, and phytanes. The highest peaks and greatest area is involved in the 1-alkene/alkane pairs. These pairs are straight chain normal hydrocarbons ranging from 9 carbons in length to over 20 carbons in length. All the pairs between are also represented. The peaks with the highest areas are in the lower molecular weight range and represent the more abundant species.

Two possible pyrolysis reactions that would describe the source of these alkene/alkane pairs are shown in Figure 45. If the reaction scheme were exclusively an α-elimination then the normal hydrocarbons would be formed by a subsequent hydrogenation reaction. This subsequent hydrogenation would occur before the pyrolysis products left the reactor and entered the condensers and could account for some of the observed n-alkanes. β-elimination produces the n-alkanes directly. Most likely α-elimination and subsequent hydrogenation, as well as some β-elimination, contributes to the observed n-alkanes. These schemes would be valid for both side chains and bridges. The side chains produced by α-elimination that did not further react would explain the 1-alkenes, but there is little evidence in the data collected for this work for di-alkenes which would have come from bridges.

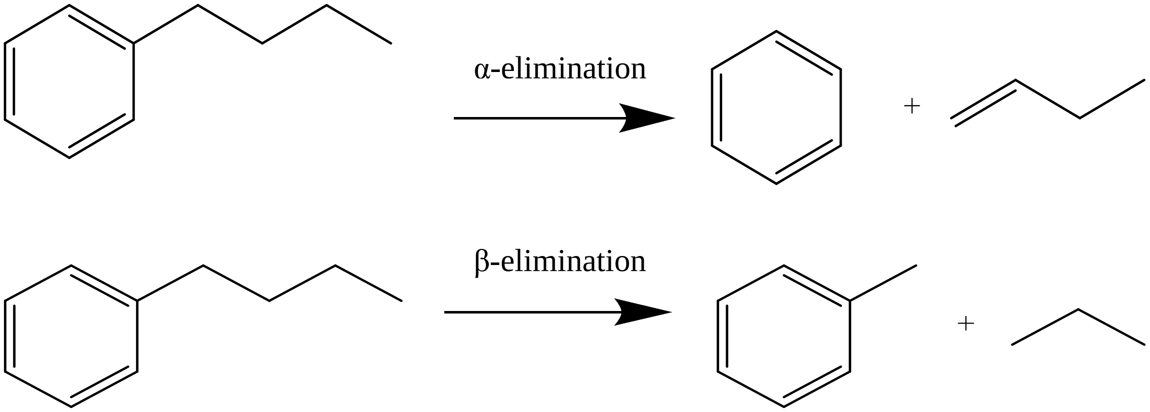

Figure 45. Two possible reaction mechanisms to produce the 1-alkene/alkane pairs observed in the A-7.PRO tars

These two elimination reactions explain the observed aliphatic chains from the kerogen matrix. The lighter products from these reactions then vaporize and are swept into the condensers and are counted as tars. The assumption is that the species generated in an open pyrolysis system (a system where the products are continuously swept from the reaction zone) and found in the tars are relatively unaltered. This thought comes from the fact that the reaction to break a carbon-carbon bond on the normal hydrocarbon side chain is greater than the reaction to break the carbon-carbon bond that connects the side chain to a core or other chain. This means that the side chains break off at a given energy level (temperature) and are swept from the reactor before they can further react.

These alkane/1-alkene pairs show a peak around undecane/1-undecene and dodecane/1-dodecene (around 12 and 14 minutes on the column respectively). This result can be independently verified by experiments using a mild oxidation of the kerogen sample using Ruthenium Tetraoxide. Figure 46 shows work by Boucher (Boucher et al., 1991) on a green river oil shale who determined that the most common straight chain hydrocarbon was C_{11} with C_{10} through C_{13} being the dominant species. The favorable comparison between the Ruthenium Tetraoxide extraction and the pyrolysis products lends credibility to these two results.

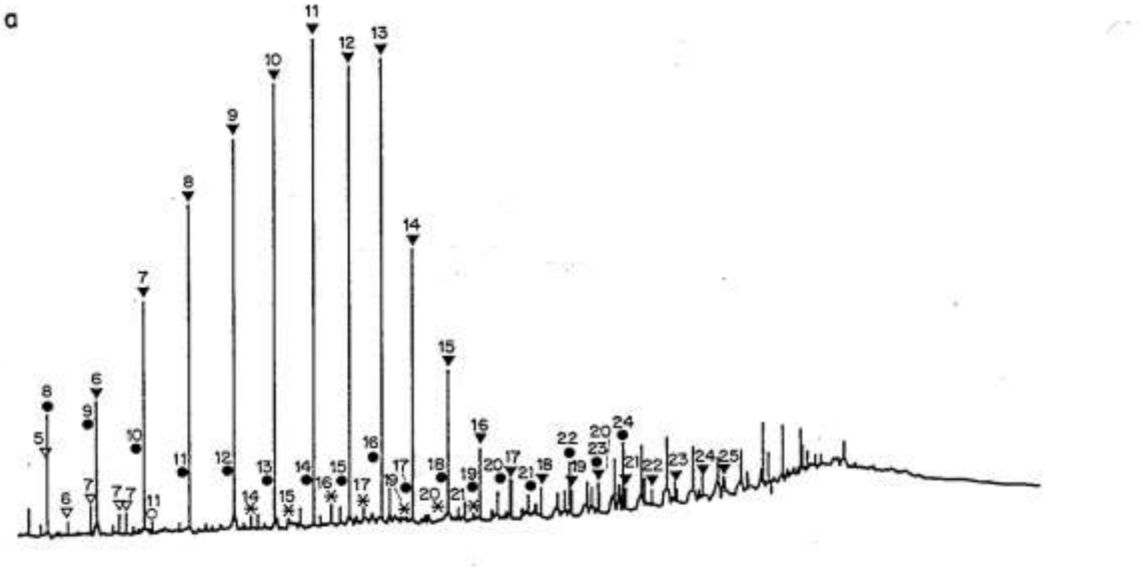

Figure 46. Reproduced figure of a gas chromatogram of esterified products from a RuO_4 mild oxidation. The symbols are as follows: ●, monocarboxylic acids; ▼, dicarboxylic acids; ○, branched monocarboxylic acids; ▽, branched dicarboxylic acids; ★, isoprenoids; □, hopanoic acids (Boucher et al., 1991)

GC/MS is a valuable tool for determining the nature of the pyrolysis products. In this work, the major products were determined to be 1-alkene/alkane pairs with other hydrocarbon chains also present. Two mechanisms were postulated that would explain the source of these products. These mechanisms would involve side-chains. Similar mechanisms would also explain bridges, but little evidence was found for di-alkenes that would suggest an α-elimination mechanism. This is hypothesized to be possible if subsequent hydrogenation reacted the double bonds to a single bond.

7.9. Fourier Transform Infrared Spectroscopy (FTIR)

Fourier Transform Infrared Spectroscopy (FTIR) is a useful technique for gas analysis since it can detect very light molecules in low concentrations. FTIR is also useful compared to GC/MS since in FTIR there is no question if all the samples eluted from the column. The FTIR analysis in this work has primarily been utilized to look for the presence of specific light gases in the effluent of the kerogen retort (section 4.1.3) for kerogen and oil shale samples. Figure 47 and Figure 48 are FTIR spectra of light gases collected from the kerogen retort with wave number (cm^{-1}) on the abscissa and arbitrarily scaled absorbance units on the ordinate. There are three temperature ranges listed, corresponding to the three temperature ranges over which the gases were collected.

FTIR coupled with pyrolysis has answered one major question that puzzled the research group. Pyrolysis is an analytical technique that is not sensitive to the presence of the mineral matrix like the other techniques. This sensitivity to the mineral matrix effects is the driving force to demineralize the sample. The resulting gases from the demineralized sample showed a strong methoxy signal in the NMR data and there was an attempt to add this to the structural model. This methoxy signal was not expected and was attributed to the esterification of acid groups by reaction with the methanol used in the demineralization process.

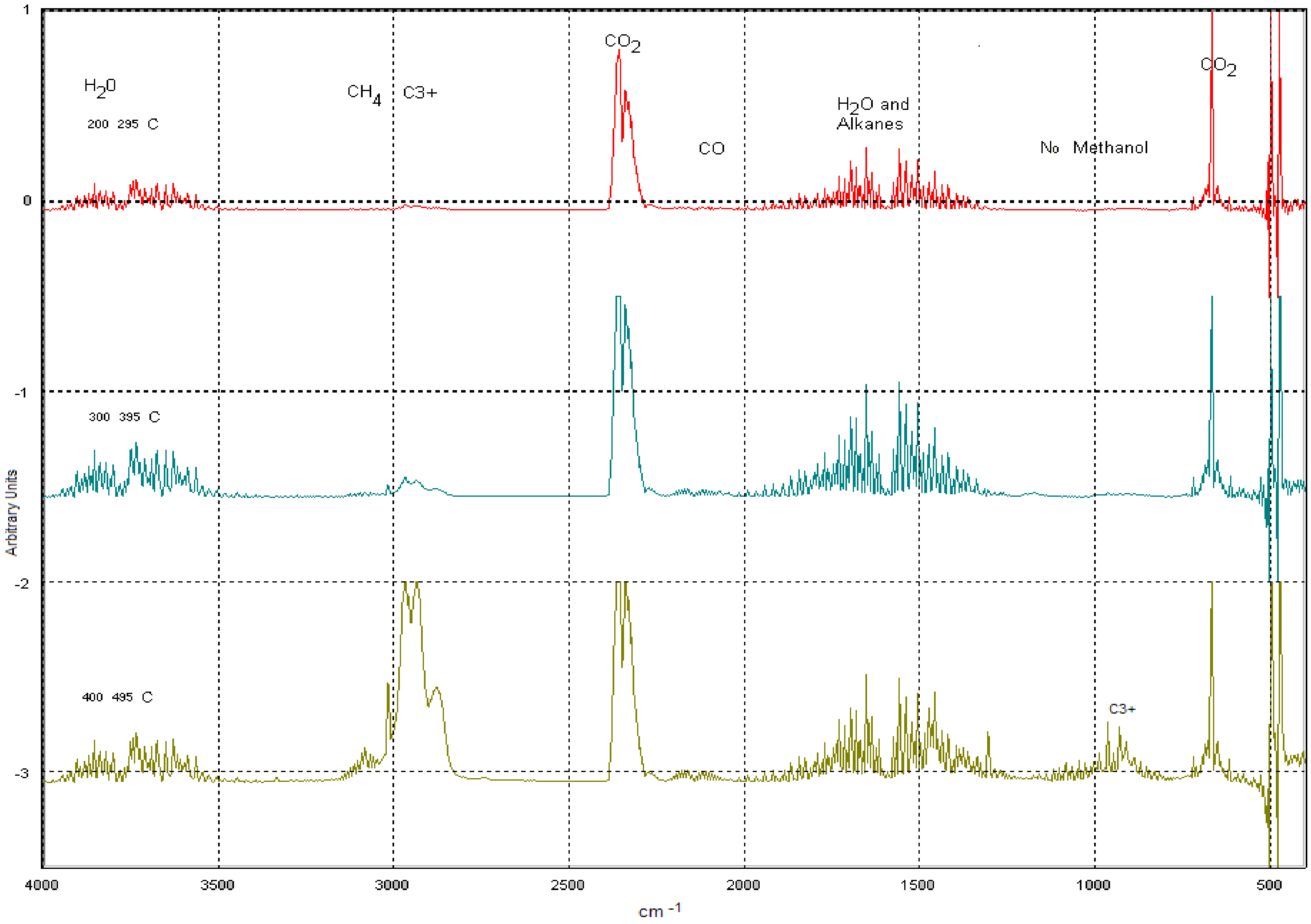

Figure 47. FTIR analysis of light gas collected from oil shale pyrolysis in the kerogen retort at the listed temperatures.

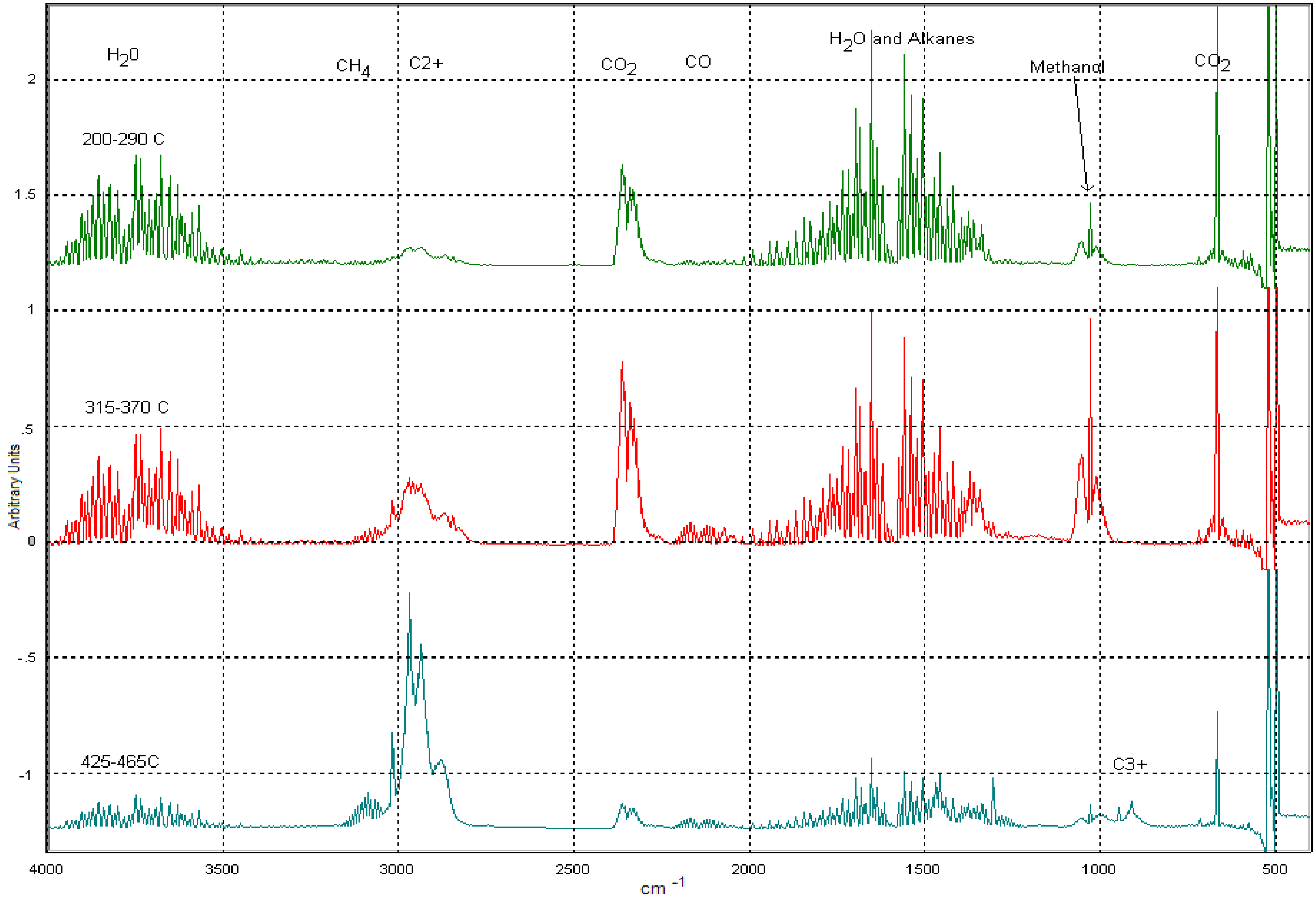

Figure 48. FTIR analysis of kerogen light gas collected from kerogen pyrolysis in the kerogen retort at different temperatures.

Pyrolysis is unaffected by the presence of the minerals, and gases collected from the pyrolysis of the oil shale did not contain methanol (Figure 47, wave numbers 1100 cm^{-1}) while the demineralized sample contained methanol (Figure 48, wave numbers 1100 cm^{-1}). This methanol would explain the methoxy signal present in the NMR spectra. The absence of methanol peaks around 1100 cm^{-1} in the oil shale pyrolysis products (Figure 47) was used to demonstrate that the extraction processes introduced methanol into the sample as previously stated. This is not too surprising since the demineralizing process involves methanol washes, but it was assumed that the vacuum drying would have removed the entire amount of methanol. The introduction of methanol into the sample would have been an impossible conclusion to determine from NMR, XPS, or other analytical techniques since the minerals in the oil shale dominate and obscure the signal from the organic matter.

7.10. Nuclear Magnetic Resonance (NMR)

Nuclear Magnetic Resonance (NMR) experiments were carried out as described in (Solum et al., 1989; Pugmire et al., 1991) courtesy of Ron Pugmire and Mark Solum at the University of Utah. The NMR data are presented in Table 17 with the structural parameters for the kerogen as well as the chars generated in the kerogen reactor by stopping the reaction at the temperatures specified at the top of the table. The raw kerogen had an aromatic cluster size of 8.4 carbons per cluster, and an average number of aliphatic carbons per side chain of 10 as estimated by dividing the molecular weight by the appropriate number of carbons and hydrogens typical of aliphatic chains. The bridges lengths would then be 20 carbons. This value is higher than that expected from the mass spectrometer analysis. The difference between the two is a topic needing further research. The aliphatic carbon f_{al} content decreases with the extent of pyrolysis. Likewise as the pyrolysis reaction progresses the fraction of aromatic carbons increases.

The NMR data also support the findings of the GC/MS in section 7.8 that during the pyrolysis of kerogen the aliphatic portion is lost. This can be seen from Table 17 where f_{al} decreases with extent of reaction; similar data can be seen in Figure 49 where the indicated f_{al}^{H} decreases relative to the aromatic compounds. The f_{al}^{H} represents CH and CH_2 groups that are present in the side chains while f_{al}^{*} represents CH_3 groups or non-protonated aliphatic carbons.

Table 17. Carbon structural parameters determined from ^{13}C NMR spectroscopy for kerogen and char final temperature.

Structural Parameter	Kerogen	442 °C	438 °C	452 °C	461 °C	523 °C
aromatic carbon, $f_a=f_{a'}+f_a^C$	0.29	0.43	0.44	0.57	0.59	0.84
carbonyl, f_a^C	0.08	0.03	0.03	0.03	0.03	0.03
aromatic carbon, carbonyl subtracted, $f_{a'}$	0.21	0.40	0.41	0.54	0.56	0.81
protonated aromatic carbon, f_a^H	0.07	0.15	0.16	0.16	0.13	0.23
nonprotonated aromatic carbon, $f_a^N=f_a^P+f_a^S+f_a^B$	0.14	0.25	0.25	0.38	0.43	0.58
aromatic carbon with oxygen carbon attachment, f_a^P	0.04	0.05	0.04	0.05	0.05	0.06
aromatic carbon with alkyl attachment, f_a^S	0.07	0.12	0.12	0.16	0.16	0.21
aromatic bridgehead and inner carbon f_a^B	0.03	0.08	0.09	0.17	0.22	0.31
aliphatic carbon, f_{al}	0.71	0.58	0.56	0.43	0.41	0.16
aliphatic CH and CH_2, f_{al}^H	0.60	0.49	0.46	0.31	0.30	0.08
aliphatic CH_3 and nonprotonated carbon, f_{al}^*	0.11	0.08	0.10	0.12	0.11	0.08
aliphatic with oxygen attachment, f_{al}^O	0.06	0.03	0.03	0.02	0.02	0.01
number of carbons per cluster, C	8.4					
total attachments per cluster, $\sigma + 1$	4.4					
bridges and loops per cluster, B_C	0.0					
side chains per cluster	4.4					
fraction of intact bridges per cluster, P	0.00					
molecular weight per cluster	720					
molecular weight per side chain	140					

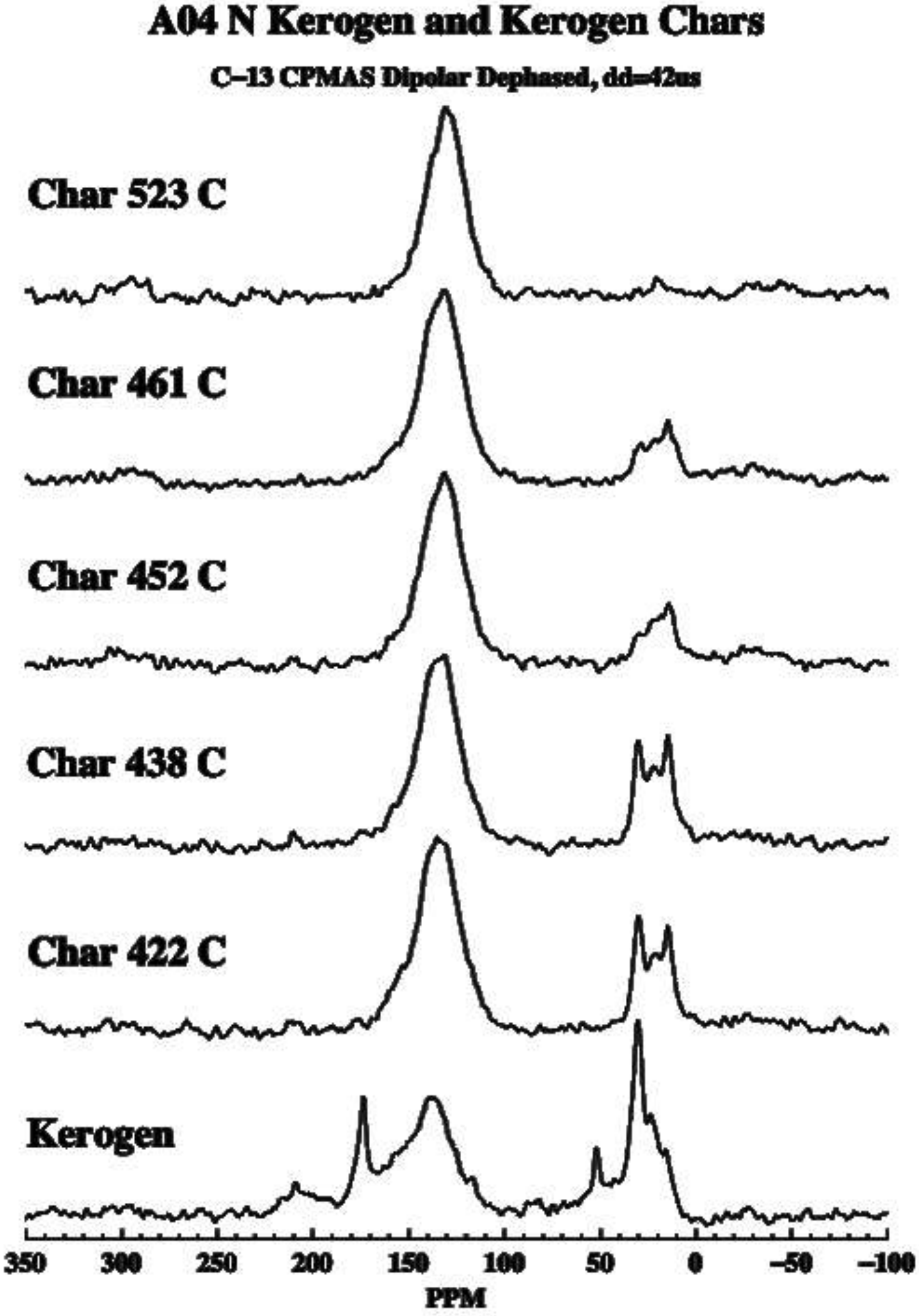

Figure 49. NMR data showing the decrease in aliphatic (shift ~30-40) with respect to the aromatic (shift ~ 120-160).

7.11. Discussion

Several analytical chemistry results were presented in this chapter to determine structural aspects that are necessary (but not necessarily sufficient) for a model. This chapter was Task 3 of this project. Sections 7.2 and 7.3 described the collection of the tars and chars used through out the chapter. Section 7.5 detailed the results of the XPS analysis. XPS demonstrates that any model must have pyridinic and pyrrolic nitrogens as well as carbonyls and carboxyl groups.

Table 14 showed that the carbon and hydrogen are released during pyrolysis faster than the other elements. This would be explained if the nitrogen and sulfur were in the aromatic clusters and the molecular fragments being lost were, for example, straight chain hydrocarbons. The pyrolysis products which were analyzed by the mass spectrometer and seen in section 7.8 show large amounts of alkane/1-alkene pairs that do not include heteroatoms, supporting this argument. Therefore a chemical structure model of kerogen should have the heteroatoms of nitrogen and sulfur in the aromatic structures (i.e., the portions of the kerogen that are stable at moderate temperatures).

A possible reason that the Green River oil shale shows pyrolysis kinetics that are very close to 1st order is that the major process is just the breaking of the bonds between the aliphatic chains and the aromatic clusters. The energy needed would be largely independent of the chain length because of α and β scission reactions. The analysis of the tar pyrolysis products by GC/MS seem to indicate that at different stages of pyrolysis the same products are produced, which is also consistent with 1st order kinetics scheme where the product distribution is not a function of conversion.

Pyrolysis is a process that is much like a sledge hammer. It adds thermal energy to all the bonds present and when sufficient energy has been added those bonds begin to break. Once the sample is broken into pieces then GC/MS and FTIR help identify those pieces. As stated above one structural feature investigated using the FTIR was the source of the methoxy groups seen in the NMR data. These methoxy groups were not seen with FTIR in the pyrolysis products from the parent sample but were present in the pyrolysis products from the extracted kerogen.

8. Summary and Conclusions

This work had the objective of determining both the kinetic parameters for the pyrolysis of oil shale and kerogen as well as using analytical techniques coupled with pyrolysis to shed light on the structure of a specific Green River Oil Shale. The first task was to fix the TGA. This required extensive replacement of the control hardware and an entirely new control program to be written. The program was written using Labview 7® to easily interface with the National Instruments hardware. The new system was demonstrated to hold pressures at 40 bar ±0.5% and temperature ramp rates from 1 to 60 K/min. This rebuilding process took nearly a year to complete, debug, and characterize the newly rebuilt equipment.

Once the equipment was working, one of the first tasks was to decide how to determine the kinetic parameters from TGA data. Because of the problems with linearized methods and disagreement among literature values and methods, a new method was developed and demonstrated. This new method shares aspects with some other commercially available methods but the new method is unique in that it uses a minimization of sum squared error from both the mass vs temperature curve and the derivative of that curve. This combination was demonstrated to determine the "correct" answer for mathematically generated data within a few percent error and was shown to have a lower sum squared error than the linearized methods.

One unexpected benefit of the method developed to determine the best fit was how a statistical confidence region could be constructed around the ideal set of parameters. This confidence region, unlike many other methods (such as a confidence interval on each parameter separately), gives a more accurate picture of allowable parameter combinations in the parameter space. The confidence region was also used to demonstrate how several sets of parameters determined by various researchers all lie within the confidence regions determined in this study. Despite the inclusion of an area of parameters in the confidence region, all parameters that may lie within the confidence region are not all equal when applied to conditions (such as heating rates) that are drastically different from those at which the parameters were determined. A discussion on how to shrink the size of the confidence region was included in section 6.4.

The curve-fitting methodology was then applied to pyrolysis kinetic data for kerogen and oil shale. Crushed samples of Green Rive Oil Shale were pyrolyzed at heating rates from 1 to 10 K/min at pressures of 1 and 40 bar and temperatures up to 1000°C. Two mass release peaks were observed corresponding to kerogen pyrolysis and carbonate decomposition for size-graded samples. The demineralized sample came from a different location in the Green River formation and showed four peaks for sample A-0. Pyrolysis of samples from subsequent stages of demineralization showed three peaks for A-3 and one peak (with a small shoulder) for A-7. The transient pyrolysis data were fit with a first-order model and a progressive Distributed Activation Energy Model (DAEM). An F-test was used to determine confidence regions and compare the kinetic parameters among the oil shale and demineralized samples for two pressure levels and three heating rates.

The activation energies determined ranged from 173 to 226 kJ/mol, with most values around 200-220 kJ/mol. The kinetic coefficients determined for oil shale and the demineralized samples were statistically the same. Only small differences in kinetic coefficients were seen in the size-graded samples, indicating negligible mass transfer resistances at the heating rates used in these experiments. The difference in the kinetic coefficients for the pyrolysis at 1 bar and 40 bar was small (~3 kJ/mol) and not statistically significant. The first-order and DAEM models were shown to be statistically different, but a visual inspection revealed that both models performed well. The largest effect on the kinetic parameters was the difference between samples collected from different geographical locations. Those samples obtained from nearer the surface showed a lower *E* and corresponding *A* than those obtained from a core sample. Despite the differences the kinetic parameters from each sample were within the confidence region for the other samples so there is no statistically significant difference. It was therefore shown for these samples that pressure, particle size, and stage of demineralization do not have a statistically significant effect on the kinetic parameters. This finding agrees with work by Reynolds (1995) on other Green River oil shale samples.

A small oil shale retort (detailed in 4.1.2) was utilized and a small kerogen retort (detailed in 4.1.3) was built for this project. Both retorts could mimic the temperature and heating rate conditions used in the TGA. These retorts allowed for the collection of appreciable char, tars, and light gases for analysis. The pyrolysis products (and the parent kerogen sample) were analyzed by several chemical techniques to determine chemical structure information about the parent sample.

The carbon and hydrogen were released during pyrolysis faster than the other elements. This would be explained if the nitrogen and sulfur were in the aromatic clusters and the structural elements being lost were straight chain hydrocarbons. The pyrolysis products which were analyzed by the mass spectrometer showed large amounts of alkane/1-alkene pairs that did not include heteroatoms, supporting this argument. XPS analysis demonstrated that any model must have pyridinic and pyrrolic nitrogens as well as carbonyls and carboxyl groups. Therefore a chemical structure model of kerogen should have the heteroatoms of nitrogen and sulfur in the aromatic region (i.e., the portions of the kerogen that are stable at moderate temperatures).

Pyrolysis is a process that is much like a sledge hammer. It adds thermal energy to all the bonds present and when sufficient energy has been added those bonds begin to break. Once the molecular structure is fragmented then GC/MS and FTIR help identify those fragments. The GC/MS data showed a distribution of alkenes/alkanes that have most frequently lengths of around 11 to 12 carbons. These alkanes/1-alkenes pairs show a peak around undecane/1-undecene and dodecane/1-dodecene (around 12 and 14 minutes on the column respectively).

As stated in section 7.9 one structural feature investigated using the FTIR was the source of the methoxy groups seen in the NMR data. These methoxy groups were not seen with FTIR in the parent sample but were present in the kerogen after demineralization. That extraction process utilized methanol. It is probable that the methoxy groups seen in the NMR data were introduced by the extraction process. Any chemical structural model must take into account these data for an accurate representation of the samples used in this study.

The NMR data also support the findings of the GC/MS in section 7.8 that during the pyrolysis of kerogen the aliphatic portion is lost. Likewise as the pyrolysis reaction progresses the fraction of aromatic carbons increases. This can be seen from Table 17 where f_{al} decreases with extent of reaction; similar data can be seen in Figure 49 where the indicated f_{al}^H decreases relative to the aromatic compounds. The f_{al}^H represents CH and CH_2 groups that are present in the side chains while f_{al}^* represents CH_3 groups or non-protonated aliphatic carbons.

9. Recommendations for Future Work

It would be impossible to examine in one dissertation all the aspects of oil shale structure. “No man is an island” once penned John Donne hundreds of years ago, and this statement is still true today. This work has benefited from past published work and future work is still to be done to unlock the secrets of oil shale. One major item of future work is to continue to collect analytical chemistry data from various sources and create a valid chemically accurate 3-D chemical structure model of oil shale from the Green River formation. Such a model would assist in both knowing what potential products could be as well as assist in determining strategies to produce the resource.

As discussed in section 6.4 one method for shrinking the confidence regions for kinetic coefficients would be to include experiments at even slower heating rates. A recommended set of experiments would be to add additional capacity to the inlet gas flow rates and conduct experiments at increasingly slower heating rates such as 0.1 K/min. These experiments could be conducted at temperatures of 550°C in order to make such experiments more reasonable. This would help in more accurate parameter determination. This work does not claim that the kinetic parameters determined herein are valid for all types of oil shale from around the globe. Differences in the shales have been previously demonstrated by several researchers to yield differences in kinetic parameters. Therefore it would be advisable to continue this work on different shales.

The global kinetic model presented in this work is suitable for many engineering applications but is not necessarily a representation of the mechanism of oil shale pyrolysis. There have been some attempts to delve into a model that would incorporate vapor-liquid equilibrium, different possible reactions, and mass transfer mechanisms. One recommendation for further work would be to develop a Chemical Pecolation Model for Devolatilization (CPD) type model of oil shale pyrolysis that would include a few mechanisms for cross linking and boiling of the pyrolysis product.

The disagreement on the bridge length between the NMR data and the pyrolysis GC/MS data is another area needing further work. It is recommended to future researchers to start with the assumptions for the determination of the NMR parameters.

10. References

Abu-Qudais, M., J. O. Jaber and S. Sawalha, "Kinetics of Pyrolysis of Attarat Oil Shale by Thermogravimetry," *Oil Shale,* **22**(1), 51-63 (2005).

Ahmad, N. and P. T. Williams, "Influence of Particle Grain Size on the Yield and Composition of Products from the Pyrolysis of Oil Shales," *Journal of Analytical and Applied Pyrolysis,* **46**(1), 31-49 (1998).

Andrews, A., "Oil Shale: History, Incentives, and Policy," CRS Report for Congress (2006).

Avid, B., B. Purevsuren and J. Dugarjav, "Pyrolysis and Thermogravimetric Investigation of the Mongolian Khoot Oil Shale," *Oil Shale,* **17**(3), 241-251 (2000).

Ballice, L., "Classification of Volatile Products of Temperature-Programmed Co-Pyrolysis of Turkish Soma Lignite and Göynük Oil Shale," *Oil Shale,* **19**(1), 57-73 (2002a).

Ballice, L., "Co-Pyrolysis of Turkish Soma Lignite and Srnak Asphaltite. Analysis of Co-Pyrolysis Products by Capillary Gas Chromatography Total Stream Sampling Technique," *Oil Shale,* **19**(2), 127-141 (2002b).

Ballice, L., "Classification of Aliphatic Hydrocarbons Formed at Temperature-Programmed Co-Pyrolysis of Turkish Oil Shales of Kerogen Types I and Ii," *Oil Shale,* **20**(1), 33-46. (2003).

Ballice, L., "Effect of Demineralization on Yield and Composition of the Volatile Products Evolved from Temperature-Programmed Pyrolysis of Beypazari (Turkey) Oil Shale," *Fuel Processing Technology,* **86**(6), 673-690 (2005).

Benbouzid, M. and S. Hafsi, "Thermal and Kinetic Analyses of Pure and Oxidized Bitumens," *Fuel,* **87**(8-9), 1585-1590 (2008).

Boucher, R. J., G. Standen, R. L. Patience and G. Eglinton, "Molecular Characterisation of Kerogen from the Kimmeridge Clay Formation by Mild Selective Chemical Degradation and Solid State 13c-Nmr," *Organic Geochemistry,* **16**(4-6), 951-958 (1989).

Boucher, R. J., G. Standen and G. Eglinton, "Molecular Characterization of Kerogens by Mild Selective Chemical Degradation -- Ruthenium Tetroxide Oxidation," *Fuel*, **70**(6), 695-702 (1991).

Braun, R. L. and A. J. Rothman, "Oil-Shale Pyrolysis: Kinetics and Mechanism of Oil Production," *Fuel*, **54**(2), 129-131 (1975).

Braun, R. L., A. K. Burnham and J. G. Reynolds, "Oil and Gas Evolution Kinetics for Oil Shale and Petroleum Source Rocks Determined from Pyrolysis-Tqms Data at Two Heating Rates," *Energy & Fuels*, **6**(4), 468-474 (1992).

Brill, T. B., P. E. Gongwer and G. K. Williams, "Thermal Decomposition of Energetic Materials. 66. Kinetic Compensation Effects in Hmx, Rdx, and Nto," *The Journal of Physical Chemistry*, **98**(47), 12242-12247 (1994).

Burlingame, A. L., P. A. Haug, H. K. Schnoes and B. R. Simoneit, "Fatty Acids Derived from the Green River Formation Oil Shale by Extractions and Oxidations - a Review," Advances in organic geochemistry International Meeting on Organic Geochemistry 4th, Amsterdam (1968).

Burnham, A. K., E. B. Huss and M. F. Singleton, "Pyrolysis Kinetics for Green River Oil Shale from the Saline Zone," *Fuel*, **62**(10), 1199-1204 (1983).

Burnham, A. K., "Oil Evolution from a Self-Purging Reactor: Kinetics and Composition at 2.Degree.C/Min and 2.Degree.C/H," *Energy & Fuels*, **5**(1), 205-214 (1991).

Burnham, A. K. and R. L. Braun, "Global Kinetic Analysis of Complex Materials," *Energy & Fuels*, **13**(1), 1-22 (1999).

Cai, J. and L. Bi, "Precision of the Coats and Redfern Method for the Determination of the Activation Energy without Neglecting the Low-Temperature End of the Temperature Integral," *Energy & Fuels*, **22**(4), 2172-2174 (2008).

Campbell, J. H., G. H. Koskinas and N. D. Stout, "Kinetics of Oil Generation from Colorado Oil Shale," *Fuel*, **57**(6), 372-376 (1978).

Campbell, J. H., G. J. Koskinas, G. Gallegos and M. Gregg, "Gas Evolution During Oil Shale Pyrolysis. 1. Nonisothermal Rate Measurements," *Fuel*, **59**(10), 718-726 (1980).

Chakravarty, T., W. Windig, K. Taghizadeh, H. L. C. Meuzelaar and L. J. Shadle, "Computer-Assisted Interpretation of Pyrolysis Mass Spectra of Two Oil Shales and Their Corresponding Kerogens," *Energy & Fuels*, **2**(2), 191-196 (1988).

Charpenay, S., M. A. Serio, R. Bassilakis, P. R. Solomon and P. Landais, "Influence of Maturation on the Pyrolysis Products from Coals and Kerogens. 2. Modeling," *Energy & Fuels*, **10**(1), 26-38 (1996).

Clayton, D., "Modeling Flow Effects During Polymer Decomposition Using Percolation Lattice Statistics," dissertation, Department of Chemical Engineering, Brigham Young University (2002).

Coats, A. W. and J. P. Redfern, "Kinetic Parameters from Thermogravimetric Data," *Nature,* **201**(4914), 68-69 (1964).

Djuricic, M., R. C. Murphy, D. Vitorovic and K. Biemann, "Organic Acids Obtained by Alkaline Permanganate Oxidation of Kerogen from the Green River (Colorado) Shale," *Geochimica et Cosmochimica Acta,* **35**(12), 1201-1207 (1971).

Dogan, O. M. and B. Z. Uysal, "Non-Isothermal Pyrolysis Kinetics of Three Turkish Oil Shales," *Fuel,* **75**(12), 1424-1428 (1996).

Doyle, C. D., "Kinetic Analysis of Thermogravimetric Data," *Journal of Applied Polymer Science,* **5**(15), 285-292 (1961).

Draper, N. R. and H. Smith, Applied Regression Analysis, John Wiley and Sons, Inc. (1998).

Durand, B., Ed. Kerogen: Insoluble Organic Matter from Sedimentary Rocks, Paris, Imprimerie Bayeusaine, 14401 Bayeux (1980).

Dyni, J. R., "Geology and Resources of Some World Oil-Shale Deposits: U.S. Geological Survey Scientific Investigations Report 2005–5294," U. S. G. Survey**:** 42 (2006).

Ekstrom, A. and G. Callaghan, "The Pyrolysis Kinetics of Some Australian Oil Shales," *Fuel,* **66**(3), 331-337 (1987).

Espitalié, J., K. Senga Makadi and J. Trichet, "Role of the Mineral Matrix During Kerogen Pyrolysis," *Organic Geochemistry,* **6**, 365-382 (1984).

Essenhigh, R. H. and M. K. Misra, "Autocorrelations of Kinetic Parameters in Coal and Char Reactions," *Energy & Fuels,* **4**(2), 171-177 (1990).

Fletcher, T. H., D. M. Grant, R. J. Pugmire and A. R. Kerstein, "Chemical Model of Coal Devolatilization Using Percolation Lattice Statistics," *Energy & Fuels,* **3**(2), 175-186 (1989).

Fletcher, T. H., A. R. Kerstein, R. J. Pugmire and D. M. Grant, "Chemical Percolation Model for Devolatilization. 2. Temperature and Heating Rate Effects on Product Yields," *Energy & Fuels,* **4**(1), 54-60 (1990).

Fletcher, T. H., A. R. Kerstein, R. J. Pugmire, M. S. Solum and D. M. Grant, "Chemical Percolation Model for Devolatilization. 3. Direct Use of 13c Nmr Data to Predict Effects of Coal Type," *Energy & Fuels,* **6**(4), 414-431 (1992).

Franks, A. J. and B. Goodier, D., "Preliminary Study of the Organic Matter of Colorado Oil Shales," *Quarterly of the Colorado School of Mines*, **17**(4), 3-16 (1922).

Freeman, E. S. and B. Carroll, "The Application of Thermoanalytical Techniques to Reaction Kinetics: The Thermogravimetric Evaluation of the Kinetics of the Decomposition of Calcium Oxalate Monohydrate," *J. Phys. Chem.*, **62**(4), 394-397 (1958).

Freund, H., J. A. Clouse and G. A. Otten, "Effect of Pressure on the Kinetics of Kerogen Pyrolysis," *Energy Fuels*, **7**(6), 1088-1094 (1993).

Freund, H., S. R. Kelemen, C. C. Walters, M. Siskin, M. L. Gorbaty, D. J. Curry and A. E. Bence, "Predicting Oil and Gas Compositional Yields Via Chemical Structure-Chemical Yield Modeling (Cs-Cym): Part 1 - Concepts and Implementation," *Organic Geochemistry*, **38**(2), 288-305 (2007).

Granoff, B. and H. E. Nuttall, "Pyrolysis Kinetics for Oil-Shale Particles," *Fuel*, **56**(3), 234-240 (1977).

Grant, D. M., R. J. Pugmire, T. H. Fletcher and A. R. Kerstein, "Chemical Model of Coal Devolatilization Using Percolation Lattice Statistics," *Energy & Fuels*, **3**(2), 175-186 (1989).

Hagaman, E. W., F. M. Schell and D. C. Cronauer, "Oil-Shale Analysis by Cp/Mas-13c N.M.R. Spectroscopy," *Fuel*, **63**(7), 915-919 (1984).

Hecker, W. C., P. M. Madsen, M. R. Sherman, J. W. Allen, R. J. Sawaya and T. H. Fletcher, "High-Pressure Intrinsic Oxidation Kinetics of Two Coal Chars," *Energy & Fuels*, **17**(2), 427-432 (2003).

Hillier, J., T. Bezzant and T. H. Fletcher, "Improved Method for the Determination of Kinetic Parameters from Non-Isothermal Thermogravimetric Analysis (Tga) Data," *Energy & Fuels*, **24**(5), 2841-2847 (2010).

Hillier, J. L. and T. H. Fletcher, "Pyrolysis Kinetics of a Green River Oil Shale Using a Pressurized Tga," *Energy & Fuels*, **25**(1), 232-239 (2011).

Hubbard, A. B. and W. E. Robinson, "A Thermal Decomposition Study of Colorado Oil Shale," *Bureau of Mines Report of Investigations 4744*, (1950).

Huggins, C. W. and T. E. Green, "Thermal Decomposition of Dawsonite," *American Mineralogist*, **58**, 548-550 (1973).

Huizinga, B. J., E. Tannenbaum and I. R. Kaplan, "The Role of Minerals in the Thermal Alteration of Organic Matter--Iii. Generation of Bitumen in Laboratory Experiments," *Organic Geochemistry*, **11**(6), 591-604 (1987a).

Huizinga, B. J., E. Tannenbaum and I. R. Kaplan, "The Role of Minerals in the Thermal Alteration of Organic Matter--Iv. Generation of N-Alkanes, Acyclic Isoprenoids, and Alkenes in Laboratory Experiments," *Geochimica et Cosmochimica Acta,* **51**(5), 1083-1097 (1987b).

Huizinga, B. J., Z. A. Aizenshtat and K. E. Peters, "Programmed Pyrolysis-Gas Chromatography of Artificially Matured Green River Kerogen," *Energy & Fuels,* **2**(1), 74-81 (1988).

Jaber, J. O. and S. D. Probert, "Non-Isothermal Thermogravimetry and Decomposition Kinetics of Two Jordanian Oil Shales under Different Processing Conditions," *Fuel Processing Technology,* **63**(1), 57-70 (2000).

Karabakan, A. and Y. Yurum, "Effect of the Mineral Matrix in the Reactions of Oil Shales: 1. Pyrolysis Reactions of Turkish Goynuk and Us Green River Oil Shales," *Fuel,* **77**(12), 1303-1309 (1998).

Kelemen, S. R., M. L. Gorbaty and P. J. Kwiatek, "Quantification of Nitrogen Forms in Argonne Premium Coals," *Energy & Fuels,* **8**(4), 896-906 (1994).

Kelemen, S. R. and P. J. Kwiatek, "Quantification of Organic Oxygen Species on the Surface of Fresh and Reacted Argonne Premium Coal," *Energy & Fuels,* **9**(5), 841-848 (1995).

Kelemen, S. R., H. Freund, M. L. Gorbaty and P. J. Kwiatek, "Thermal Chemistry of Nitrogen in Kerogen and Low-Rank Coal," *Energy & Fuels,* **13**(2), 529-538 (1999).

Kelemen, S. R., M. Afeworki, M. L. Gorbaty, P. J. Kwiatek, M. S. Solum, J. Z. Hu and R. J. Pugmire, "Xps and 15n Nmr Study of Nitrogen Forms in Carbonaceous Solids," *Energy & Fuels,* **16**(6), 1507-1515 (2002).

Kelemen, S. R., M. Afeworki, M. L. Gorbaty, M. Sansone, P. J. Kwiatek, C. C. Walters, H. Freund, M. Siskin, A. E. Bence, D. J. Curry, M. Solum, R. J. Pugmire, M. Vandenbroucke, M. Leblond and F. Behar, "Direct Characterization of Kerogen by X-Ray and Solid-State 13C Nuclear Magnetic Resonance Methods," *Energy & Fuels,* **21**(3), 1548-1561 (2007).

Knicker, H., A. W. Scaroni and P. G. Hatcher, "13c and 15n Nmr Spectroscopic Investigation on the Formation of Fossil Algal Residues," *Organic Geochemistry,* **24**(6-7), 661-669 (1996).

Kök, M. and A. Iscan, "Oil Shale Kinetics by Differential Methods," *Journal of Thermal Analysis and Calorimetry,* **88**(3), 657-661 (2007).

Kok, M. V. and R. Pamir, "Pyrolysis Kinetics of Oil Shales Determined by Dsc and Tg/Dtg," *Oil Shale,* **20**(1), 57-68 (2003).

Lee, S., Oil Shale Technology, Boca Raton, Fla., CRC Press (1991).

Li, S. and C. Yue, "Study of Pyrolysis Kinetics of Oil Shale," *Fuel,* **82**(3), 337-342 (2003).

Linder, G., L. A. Andersson and I. Bjerle, "Influence of Heating Rate on the Pyrolysis of Oil Shale," *Fuel Processing Technology,* **8**(1), 19-31 (1983).

Liu, L. K., "Discrete Optimization of Pipe Networks Systems by Simulated Annealing," Masters Thesis, Mechanical Engineering, Brigham Young University (1990).

M. Abu-Qudais, J. O. J., S. Sawalha, "Kinetics of Pyrolysis of Attarat Oil Shale by Thermogravimetry," *Oil Shale,* **22**(1), 51-63 (2005).

Mochidzuki, K., A. Sakoda and M. Suzuki, "Measurement of the Hydrothermal Reaction Rate of Cellulose Using Novel Liquid-Phase Thermogravimetry," *Thermochimica Acta,* **348**(1-2), 69-76 (2000).

Mohlen, H. J. and A. Sulimma, "High Temperature, High Pressure Thermogravimetry of Coal Gasification-Apparatus, Data Acuisition and Numerical Evaluation," *Thermochimica Acta,* **103**(1), 163-168 (1986).

Moulder, J. F., W. F. Stickle, P. E. Sobol and K. D. Bomben, Handbook of X Ray Photoelectron Spectroscopy: A Reference Book of Standard Spectra for Identification and Interpretation of Xps Data, Minnesota, Physical Electronics Inc (1995).

Mraz, T., R. Rosenvold, J. DuBow and K. Rajeshwar, "Acid Dissolution of Mineral Matrix in Green River Oil Shale. 2. Effect of Ultrasonic Field," *Fuel,* **63**(7), 927-930 (1984).

Ozawa, T., "A New Method of Analyzing Thermogravimetric Data," *Bulletin of the Chemical Society of Japan,* **38**(11), 1881-1886 (1965).

Parkinson, A. R. and R. J. Balling, "The Optdesx Design Optimization Software," *Structural and Multidiciplinary Optimization,* **23**(2), 127-139 (2002).

Popescu, C., E. Segal and C. Oprea, "A Comparison of Some Integral Methods," *Journal of Thermal Analysis and Calorimetry,* **38**(4), 929-933 (1992).

Popescu C., E. S., "Critical Considerations on the Methods for Evaluating Kinetic Parameters from Nonisothermal Experiments," *International Journal of Chemical Kinetics,* **30**(5), 313-327 (1998).

Price, L. C. and L. M. Wenger, "The Influence of Pressure on Petroleum Generation and Maturation as Suggested by Aqueous Pyrolysis," *Organic Geochemistry,* **19**(1-3), 141-159 (1992).

Pugmire, R. J., M. S. Solum, D. M. Grant, S. Critchfield and T. H. Fletcher, "Structural Evolution of Matched Tar-Char Pairs in Rapid Pyrolysis Experiments," *Fuel,* **70**(3), 414-423 (1991).

Rajeshwar, K., "The Kinetics of the Thermal Decomposition of Green River Oil Shale Kerogen by Non-Isothermal Thermogravimetry," *Thermochimica Acta,* **45**(3), 253-263 (1981).

Rajeshwar, K. and J. Dubow, "On the Validity of a First-Order Kinetics Scheme for the Thermal Decomposition of Oil Shale Kerogen," *Thermochimica Acta,* **54**(1-2), 71-85 (1982).

Reynolds, J. G., R. W. Crawford and A. K. Burnham, "Analysis of Oil Shale and Petroleum Source Rock Pyrolysis by Triple Quadrupole Mass Spectrometry: Comparisons of Gas Evolution at the Heating Rate of 10.Degree.C/Min," *Energy & Fuels,* **5**(3), 507-523 (1991).

Reynolds, J. G. and A. K. Burnham, "Comparison of Kinetic Analysis of Source Rocks and Kerogen Concentrates," *Organic Geochemistry,* **23**(1), 11-19 (1995).

S. R. Kelemen, M. A., M. L. Gorbaty, M. Sansone, C. C. Walters, H. Freund, "Direct Characterization of Kerogen by X-Ray and Solid-State 13c Nmr Methods," (2006).

Schmidt-Collerus, J. J. and C. H. Prien, "Investigations of the Hydrocarbon Structure of Kerogen from Oil Shale of the Green River Formation," *ACS Division Fuel Chemistry,* **19**(2), 100-108 (1974).

Scott, S. A., J. S. Dennis, J. F. Davidson and A. N. Hayhurst, "Thermogravimetric Measurements of the Kinetics of Pyrolysis of Dried Sewage Sludge," *Fuel,* **85**(9), 1248-1253 (2006a).

Scott, S. A., J. S. Dennis, J. F. Davidson and A. N. Hayhurst, "An Algorithm for Determining the Kinetics of Devolatilisation of Complex Solid Fuels from Thermogravimetric Experiments," *Chemical Engineering Science,* **61**(8), 2339-2348 (2006b).

Seber, G. A. F. and C. J. Wild, Nonlinear Regression, Wiley & Sons (2003).

Shao, J., R. Yan, H. Chen, B. Wang, D. H. Lee and D. T. Liang, "Pyrolysis Characteristics and Kinetics of Sewage Sludge by Thermogravimetry Fourier Transform Infrared Analysis," *Energy & Fuels,* **22**(1), 38-45 (2008).

Shih, S. M. and H. Y. Sohn, "Nonisothermal Determination of the Intrinsic Kinetics of Oil Generation from Oil Shale," *Ind. Eng. Chem. Proc. Des. Dev.,* **19**(3), 420-426 (1980).

Shuyuan, L., Y. Zhe, Q. Jialin and G. Shaohui, "Thermogravimetric Kinetics Study on Some Chinese Oil Shales," *Oil Shale,* **18**(4), 307-314 (2001).

Silbernagel, B. G., L. A. Gebhard, M. Siskin and G. Brons, "Esr Studies of Kerogen Conversion in Shale Pyrolysis," *Energy & Fuels,* **1**(6), 501-506 (1987).

Siskin, M., C. G. Scouten, K. D. Rose, T. Aczel, S. G. Colgrove and J. R. E. Pabst, "Detailed Structural Characterization of the Organic Material in Rundle Ramsay Crossing and Green River Oil Shales," Composition, Geochemistry and Conversion of Oil Shales, C. Snape, Dordrecht, Netherlands, Kluwer Academic Publishers**:** 143-158 (1995).

Skala, D., H. Kopsch, M. Sokic, H. J. Neumann and J. A. Jovanovic, "Kinetics and Modelling of Oil Shale Pyrolysis," *Fuel,* **69**(4), 490-496 (1990).

Solum, M. S., R. J. Pugmire and D. M. Grant, "Carbon-13 Solid-State Nmr of Argonne-Premium Coals," *Energy & Fuels,* **3**(2), 187-193 (1989).

Torrente, M. C. and M. A. Galan, "Kinetics of the Thermal Decomposition of Oil Shale from Puertollano (Spain)," *Fuel,* **80**(3), 327-334 (2001).

Van de Meent, D., S. C. Brown, R. P. Philp and B. R. T. Simoneit, "Pyrolysis-High Resolution Gas Chromatography and Pyrolysis Gas Chromatography-Mass Spectrometry of Kerogens and Kerogen Precursors," *Geochimica et Cosmochimica Acta,* **44**(7), 999-1013 (1980).

Vandegrift, G. F., R. E. Winans, R. G. Scott and E. P. Horwitz, "Quantitative Study of the Carboxylic Acids in Green River Oil Shale Bitumen," *Fuel,* **59**(9), 627-633 (1980).

Vandenbroucke, M. and C. Largeau, "Kerogen Origin, Evolution and Structure," *Organic Geochemistry,* **38**(5), 719-833 (2007).

Vyazovkin, S. and C. A. Wight, "Model-Free and Model-Fitting Approaches to Kinetic Analysis of Isothermal and Nonisothermal Data," *Thermochimica Acta,* **340-341**, 53-68 (1999).

Williams, P. T. and N. Ahmad, "Influence of Process Conditions on the Pyrolysis of Pakistani Oil Shales," *Fuel,* **78**(6), 653-662 (1999).

Williams, P. T. and N. Ahmad, "Investigation of Oil-Shale Pyrolysis Processing Conditions Using Thermogravimetric Analysis," *Applied Energy,* **66**(2), 113-133 (2000).

Yen, T. F., Ed. Science and Technology of Oil Shale, Ann Arbor, Ann Arbor Science Publishers (1976).

Yen, T. F. and G. V. Chilingarian, Oil Shale, Elsevier Scientific Publishing Company (1976).

Zhang, H., "Nitrogen Evolution and Soot Formation During Secondary Coal Pyrolysis," Chemical Engineering, Brigham Young University (2001).

A. **Appendix**

A.1. Critiques of Method (see section 5.5)

A.1.1. Overview of Critique

In response to this method one researcher claimed,

> *"Since there is correlation between the activation energy (E) and the prefactor (A), one would expect many combinations of E and A to give similar results, especially when one considers experimental variability. This is why one should not compare only activation energies. One should compare A and E combinations. For example, Brill et al. (J. Phys. Chem. 1994, 98, 12242). outlined the kinetic compensation effect by plotting ln(A) versus E. The ln(A) versus E points should lie on a straight line, if the fits are acceptable. I plotted ln(A) versus E for your fits and they did not lie on a straight line indicating that your fits were not adequate. Again, you should be comparing combinations of A and E, not these values separately. Once you understand kinetic compensation, you will notice that one could use a wide range of activation energies, and select a value of A that would fit the data within the measurement error. I have done this with one of your data sets and fit the data with a simple adjustment of the prefactor, thus arriving at a combination of A and E that is acceptable. For example, using your derivative with all points fit E=145.7 and lnA = 32.05, I changed lnA to 28 and matched the data!"*

This researcher brings up the point that the ln(A) and the E are linearly correlated and references a paper by Brill (1994) that describes a method to compensate for this effect. This effect was not first pointed out by Brill and has been described elsewhere in literature (Essenhigh and Misra, 1990). The reason for this effect can be seen from the Arrhenius form rate constant and forms the basis for the rebuttal to this researcher's critique.

A.1.2. Response

Another explanation for the observed effect can be seen when a joint 95% confidence region is constructed for the parameters. The shape of the confidence region is similar to a narrow crescent for A vs. E or it is a narrow oval for ln(A) vs. E. The major axis of the oval shaped confidence region is oriented diagonally with a positive slope in a plot of ln(A) vs. E. After reading the paper by Brill et al. It was hypothesized that the kinetic parameter combinations that lie on a line are most likely all within the confidence region for the combination of the data sets. This would lead to the conclusion that Brill's method is nothing more than a description of a line that is the major axis for that confidence region. Such an analysis could be performed by collecting all the data sets, analyzing them for a best estimate of parameters and constructing a joint confidence region for comparison. The methodology for constructing a joint confidence region can be found in statistics textbooks such as Nonlinear Regression by Seber and published by Wiley or Applied Regression Analysis by Draper and published by Wiley. This would indicate that the adjustment in the paper by Brill is nothing more than an adjustment to bring values back into the confidence region and would explain why all the parameters line in a line. That line is nothing more than the major axis for the confidence region with an **optimum that can be found**. However, as shown below, all E and A combinations along Brill's line (and hence possibly in the confidence region) do not describe the data equally well.

The method by Brill indicates that any value of E could be chosen and a corresponding A can be found. The problem of course comes as you deviate from the "true" set of kinetic parameters. This can be best seen when E is either 0 or really large.

This would represent exceeding the limits of the confidence region. This can be seen by taking a mass trace and two good parameter sets of the data to determine the a and b for Brill’s method. Then predicting a new ln(A) based on other values of E and comparing them back to the original mass trace. As the E becomes large the reaction happens in an ever increasingly narrow temperature range with the limit being a step change in the mass. As the E becomes smaller the rate of maximum change is predicted at a lower and lower temperature and the shape of the trace becomes broader. Figures Figure A- 50, Figure A-51, and Figure A-52 are one demonstration of why Brill’s method is unacceptable. In Figure A- 50 was generated from a mass trace and fit two curves using different activation energies. These activation energies are in J/mol and lie within the ranges reported for the samples in Brill’s paper. Using these two “good” fits it was found that the a and b values used in the Brill method. E’s were then chosen which spanned the range for the same sample in Brill’s paper. Next the method was used to predict the A’s using the a and b parameters that were found previously as recommended by Brill and seen in Figure A-51. Then each of these combinations were used to predict the non-isothermal mass loss curves and compared them to the original mass trace. This is the same mass trace shown in Figure A- 50. It can be seen in Figure A-52 that the Brill method does not give acceptable results especially the farther the E deviates from the “good” fits. This would indicate that a unique optimum can be found.

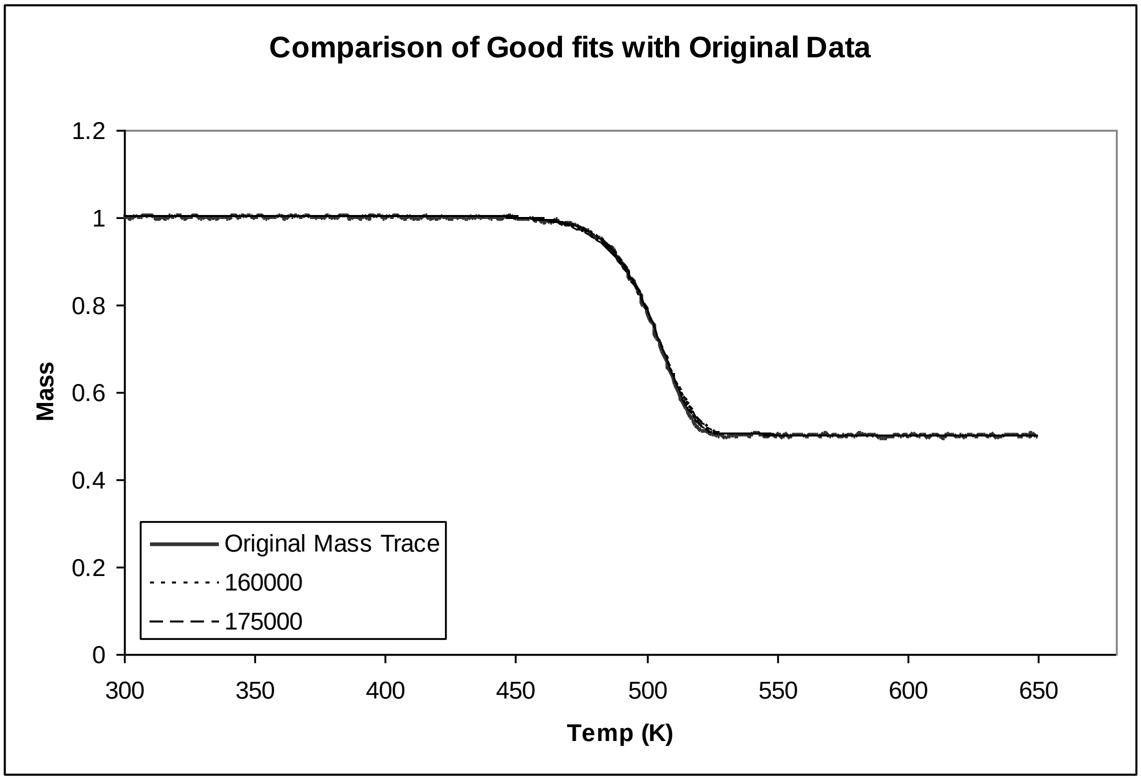

Figure A- 50. Determination of Two Good fits for use in the Brill Method

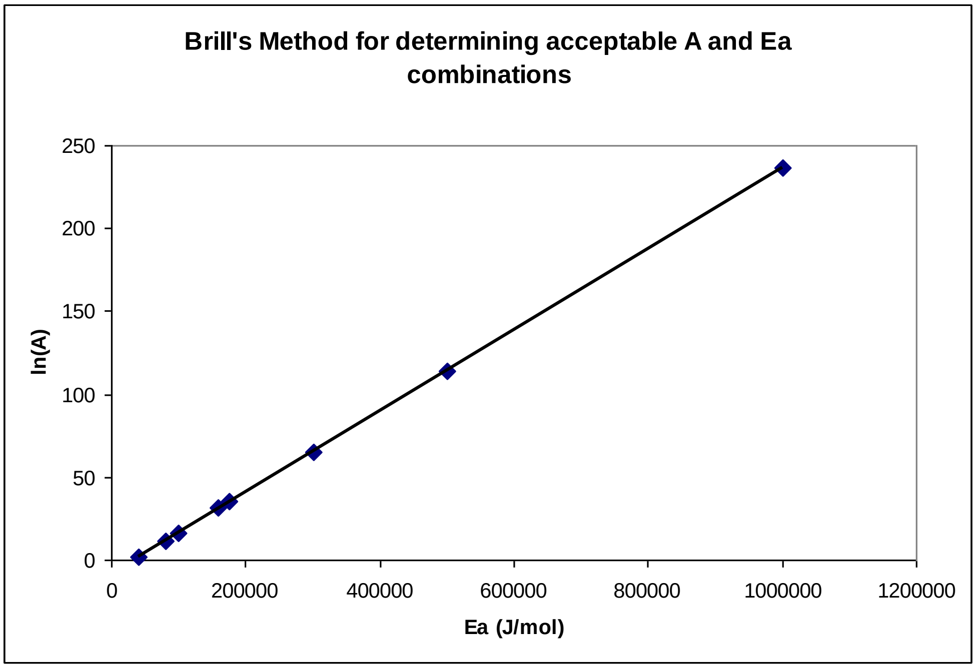

Figure A-51. Acceptable E and A combinations as predicted by the Brill method

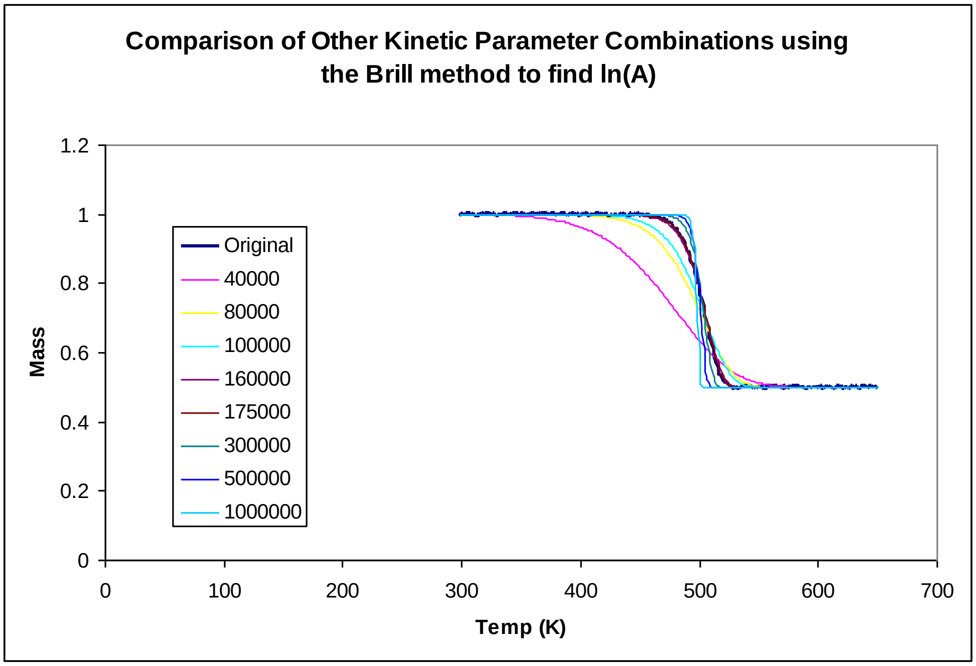

Figure A-52. Use of "Acceptable" E and A combinations to predict mass loss as determined by Brill method. E's here are in J/mol.

Even if an apparently good fit can be determined by adjusting the value of A; it can never get the best fit unless both values match the true values. Adjusting the A merely brings the combination back into the confidence region unless of course the E has exceeded the limits of the confidence region and then no adjustment of A will be adequate such as the E = 40,000J/mol seen in Figure A-52. A comparison of a set of kinetic parameters determined by first getting the E from the derivative method and then the A from the Brill method will not usually yield a result that is better than the method described in this chapter. Also of note is that as the heating rate changes only the true E and A combination will continue to match the curve. Take the case pointed out by the researcher. The data set from which the experiment was conducted involved a heating rate of 1K/s. The reviewer describes how using the Brill method to determine the ln(A) for an E of 145.7 kJ matches the data. Returning to that heating rate the values were plotted which were described as the “actual” values. This “match” is shown here in Figure A-53 with a heating rate of 1K/s.

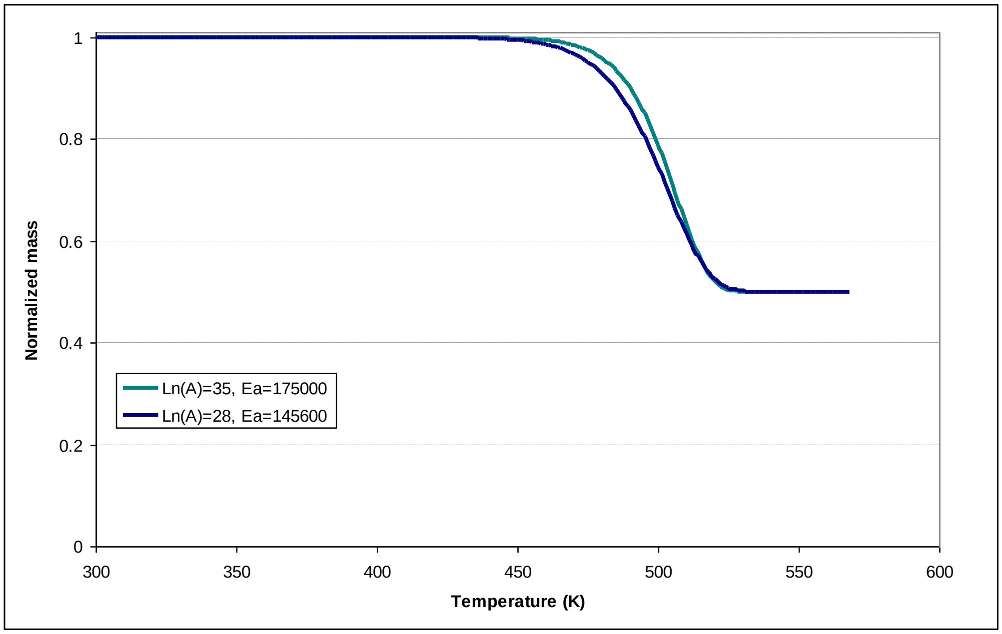

Figure A-53. A comparison between the actual values and the reviewers values at 1K/s

Note the slight discrepancy in the lower temperature range. These are the values that the reviewer used to “match” the data. Furthermore if the heating rate is changed the discrepancy becomes even more drastic as shown in Figure A-54 with a heating rate of 100 K/s and in Figure A-55 with a heating rate of 0.01K/s. A different adjustment would be required at each heating rate where as an optimally determined set of kinetic parameters from multiple heating rates would track the intrinsic kinetics across various heating rates. The method explained in this chapter and in two papers by Hillier et al.(Hillier et al., 2010; Hillier and Fletcher, 2010) describes using multiple heating rates, which ones to select, and discusses the benefits of a proper selection in regards to this work.

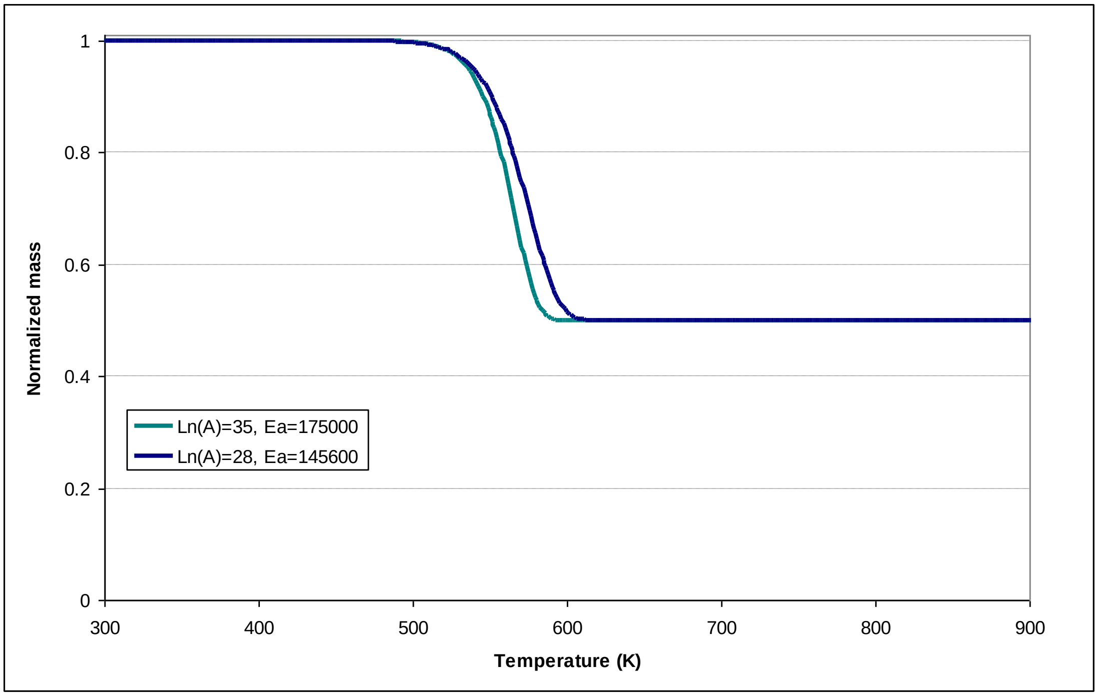

Figure A-54. A comparison between the actual values and the reviewers values at 100K/s.

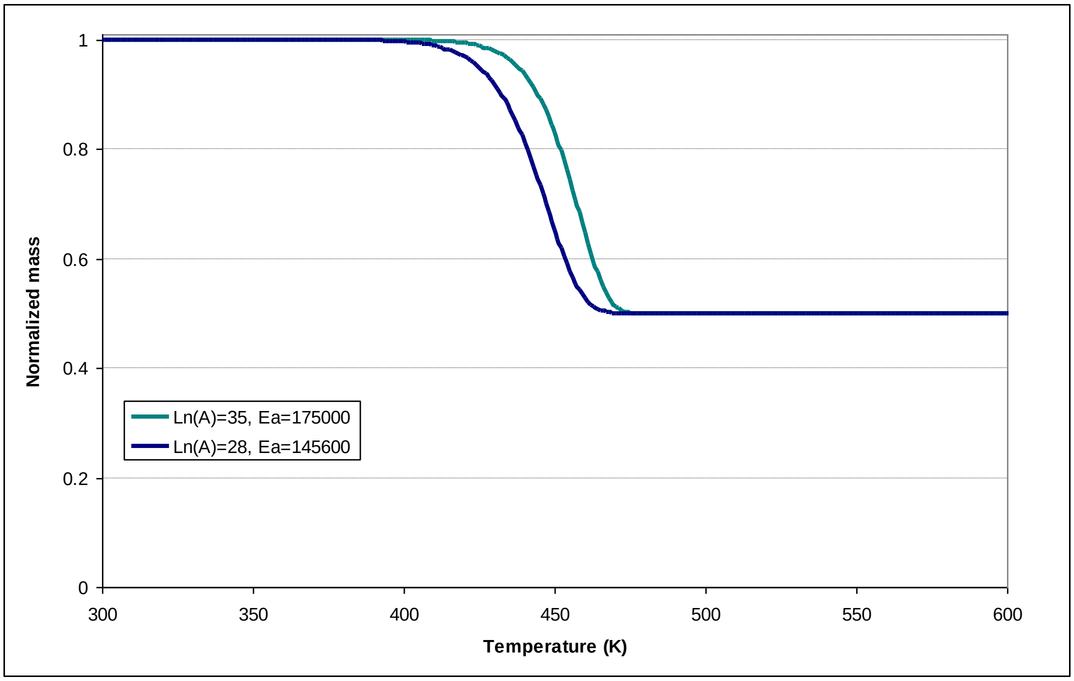

Figure A-55. A comparison between the actual values and the reviewers values at 0.01K/s

A.2. Pseudo Code for optimization program

This pseudo code is written for one data file with four reactions and the distributed activation energy model. Additional data files would require additional lines of code.

```
(#includes)

(Declare variables)

(Read in data files)

/*-------------------------------------------------------------------------------------------------*/
/*--------------------Below is the actual optimization routine---------------------------------*/
/*-------------------------------------------------------------------------------------------------*/


        avdscaC( &A1, "A1" );

        avdscaC( &Ea01, "Ea01" );

        avdscaC( &sigma1, "sigma1" );

        avdscaC( &m1o1, "m1o1" );
        avdscaC( &m2o1, "m2o1" );
        avdscaC( &m3o1, "m3o1" );
        avdscaC( &m4o1, "m4o1" );



m11[1]=m1o1,m21[1]=m2o1,m31[1]=m3o1,m41[1]=m4o1;


        /*constraints on the masses*/
mtoto1=m1o1+m2o1+m3o1+m4o1;


        sserr=0, ssed=0, ssem=0, ssed1=0,ssed2=0,ssed3=0,ssed4=0;

/*Data set 1***************************/
```

```
for (i=1;i<(n1-1);i++)
{

        mtot1[i]=m11[i]+m21[i]+m31[i]+m41[i];

        x1=inverf((1-m11[i]/m1o1));
        Ea1=Ea01+x1*sigma1;
        k11[i]=-pow(A1,10)*exp(-Ea1/(R*mtemp1[i]));
        m11[i+1]=max(m11[i]+k11[i]*(mtm1[i+1]-mtm1[i])*m11[i],0);

        for (j=1;j<dn11;j++)
        {
                if(dtm11[j]==mtm1[i+1]) {
                dmdt11[j]=k11[i]*m11[i];
                ssed1=ssed1+pow(ddmdt11[j]-dmdt11[j],2)/dn11+pow(mmass1[i]-
mtot1[i],2.)/n1;
                }
                else{
                }

        }

        x2=inverf((1-m21[i]/m2o1));
        Ea2=Ea02+x2*sigma2;
        k21[i]=-pow(A2,10)*exp(-Ea2/(R*mtemp1[i]));
        m21[i+1]=max(m21[i]+k21[i]*(mtm1[i+1]-mtm1[i])*m21[i],0);

        for (j=1;j<dn21;j++)
        {
                if(dtm21[j]==mtm1[i+1]) {
                dmdt21[j]=k21[i]*m21[i];
                ssed2=ssed2+pow(ddmdt21[j]-dmdt21[j],2)/dn21+pow(mmass1[i]-
mtot1[i],2.)/n1;
                }
                else{
                }


        }

        x3=inverf((1-m31[i]/m3o1));
        Ea3=Ea03+x3*sigma3;
        k31[i]=-pow(A3,10)*exp(-Ea3/(R*mtemp1[i]));
        m31[i+1]=max(m31[i]+k31[i]*(mtm1[i+1]-mtm1[i])*m31[i],0);
```

```
          for (j=1;j<dn31;j++)
          {
                    if(dtm31[j]==mtm1[i+1]) {
                    dmdt31[j]=k31[i]*m31[i];
                    ssed3=ssed3+pow(ddmdt31[j]-dmdt31[j],2)/dn31+pow(mmass1[i]-
mtot1[i],2.)/n1;
                    }
                    else{
                    }



          }



          x4=inverf((1-m41[i]/m4o1));
          Ea4=Ea04+x4*sigma4;
          k41[i]=-pow(A4,10)*exp(-Ea4/(R*mtemp1[i]));
          m41[i+1]=max(m41[i]+k41[i]*(mtm1[i+1]-mtm1[i])*m41[i],0);


          for (j=1;j<dn41;j++)
          {
                    if(dtm41[j]==mtm1[i+1]) {
                    dmdt41[j]=k41[i]*m41[i];
                    ssed4=ssed4+pow(ddmdt41[j]-dmdt41[j],2)/dn41+pow(mmass1[i]-
mtot1[i],2.)/n1;
                    }
                    else{
                    }

          }



          ss1[i]=pow(mmass1[i]-mtot1[i],2.)/n1;
          ssem=ssem+ss1[i];



}
          ssed=ssed1+ssed2+ssed3+ssed4;
          sserr=ssem+ssed;


  /* send functions to OptdesX ("Function names 16 chars max")*/
  afdscaC( sserr, "SSError" );
  afdscaC( mtoto1, "mtoto1" );
  afdscaC( ssed1, "ssed1" );
```

```
  afdscaC( ssed2, "ssed2" );
  afdscaC( ssed3, "ssed3" );
  afdscaC( ssed4, "ssed4" );
}

/*=========================================================================
   Function anaposC
     Postprocessing Function
---------------------------------------------------------------------------*/
void anaposC( void )
{

}

/*=========================================================================
   Function inverf
     Inverse Error Function
                This program calculates the inverse of the area under the normal curve.
                if y=area(x), then given y, this program will calculate x.
                A table lookup is performed.
---------------------------------------------------------------------------*/

double inverf(double y)
         {
          int i;
          double fac, yp, x;
          double xx []= {3.4,3.2,3.,2.8,2.6,2.4,2.2,2.,1.8,1.6,1.4,1.2,1.,.8,.6,.4,.2,0.};
    double yy []=
{.9997,.9993,.9987,.9974,.9953,.9918,.9861,.9772,.9641,.9452,.9192,.8849,.8413,.7881,.
7257,.6554,.5793,.5};


    fac = 1.;
/*  check to see if y is within range */
     if(y < 0.0228){
       x = -2.0;
       return (x);
                 }
     else if(y < 0.5){
      yp = 1.-y;
      fac = -1.;
                }
     else if(y > 0.9997){
      x = 3.5;
                return (x);
                }
```

```
    else
                {
      yp = y;
                }

/*  search for range */


            for(i=17;i>0;i--)
            {
              if(yp < yy[i-1]){
          x = xx[i] + (yp-yy[i])*(xx[i-1]-xx[i])/(yy[i-1]-yy[i]);
          x = fac*x;
                          return(x);
              }
              else{
              }
            }

            return(x);


}


double max(double a, double b)
{
            double x;

            if(a > b){
                        x=a;
                        return(x);
            }
            else {
                        x=b;
                        return(x);
            }

}
```

This pseudo code is written for one data file with four reactions and 1st order model. Additional data files would require additional lines of code.

```
(#includes)

(Declare variables)

(Read in data files)


/*-------------------------------------------------------------------------------------------------*/
/*--------------------Below is the actual optimization routine--------------------------------*/
/*-------------------------------------------------------------------------------------------------*/


   avdscaC( &A1, "A1" );
   avdscaC( &A2, "A2" );
   avdscaC( &A3, "A3" );
   avdscaC( &A4, "A4" );

   avdscaC( &Ea1, "Ea1" );
   avdscaC( &Ea2, "Ea2" );
   avdscaC( &Ea3, "Ea3" );
   avdscaC( &Ea4, "Ea4" );

   avdscaC( &m1o1, "m1o1" );
   avdscaC( &m2o1, "m2o1" );
   avdscaC( &m3o1, "m3o1" );
   avdscaC( &m4o1, "m4o1" );




m11[1]=m1o1,m21[1]=m2o1,m31[1]=m3o1,m41[1]=m4o1;

mtoto1=m1o1+m2o1+m3o1+m4o1; /*constraints on the masses*/



sserr=0;

/*Data set 1***************************/
for (i=1;i<n1;i++)
{
            k11[i]=-pow(A1,10)*exp(-Ea1/(R*mtemp1[i]));
            k21[i]=-pow(A2,10)*exp(-Ea2/(R*mtemp1[i]));
            k31[i]=-pow(A3,10)*exp(-Ea3/(R*mtemp1[i]));
```

```
        k41[i]=-pow(A4,10)*exp(-Ea4/(R*mtemp1[i]));

    }

    for (i=1;i<(n1-1);i++)
    {
        m11[i+1]=m11[i]*exp(((k11[i+1]+k11[i])/2)*(mtm1[i+1]-mtm1[i]));
        for (j=1;j<dn11;j++)
        {
            if(dtm11[j]=mtm1[i+1]) {
            dmdt11[j]=k11[i]*m11[i+1];
            sserr=sserr+pow(ddmdt11[j]-dmdt11[j],2);
            }
            else{
            }



        }

        m21[i+1]=m21[i]*exp(((k21[i+1]+k21[i])/2)*(mtm1[i+1]-mtm1[i]));
        for (j=1;j<dn21;j++)
        {
            if(dtm21[j]=mtm1[i+1]) {
            dmdt21[j]=k21[i]*m21[i+1];
            sserr=sserr+pow(ddmdt21[j]-dmdt21[j],2);
            }
            else{
            }



        }

        m31[i+1]=m31[i]*exp(((k31[i+1]+k31[i])/2)*(mtm1[i+1]-mtm1[i]));
        for (j=1;j<dn31;j++)
        {
            if(dtm31[j]=mtm1[i+1]) {
            dmdt31[j]=k31[i]*m31[i+1];
            sserr=sserr+pow(ddmdt31[j]-dmdt31[j],2);
            }
            else{
            }
        }

        m41[i+1]=m41[i]*exp(((k41[i+1]+k41[i])/2)*(mtm1[i+1]-mtm1[i]));
        for (j=1;j<dn41;j++)
        {
```

```
                if(dtm41[j]=mtm1[i+1]) {
                dmdt41[j]=k41[i]*m41[i+1];
                sserr=sserr+pow(ddmdt41[j]-dmdt41[j],2);
                }
                else{
                }
        }

        mtot1[i]=m11[i]+m21[i]+m31[1]+m41[1];
        ss1[i]=pow(mmass1[i]-mtot1[i],2.);
        sserr=sserr+ss1[i];


}


  /* send functions to OptdesX ("Function names 16 chars max") */
  afdscaC( sserr, "SSError" );
  afdscaC( mtoto1, "mtoto1" );

}

/*=============================================================
===============
   Function anaposC
     Postprocessing Function
----------------------------------------------------------------------------*/
void anaposC( void )
{
}
```

B. **References for Appendix**

Brill, T. B., P. E. Gongwer and G. K. Williams, "Thermal Decomposition of Energetic Materials. 66. Kinetic Compensation Effects in Hmx, Rdx, and Nto," *The Journal of Physical Chemistry,* **98**(47), 12242-12247 (1994)

Essenhigh, R. H. and M. K. Misra, "Autocorrelations of Kinetic Parameters in Coal and Char Reactions," *Energy & Fuels,* **4**(2), 171-177 (1990)

Hillier, J., T. Bezzant and T. H. Fletcher, "Improved Method for the Determination of Kinetic Parameters from Non-Isothermal Thermogravimetric Analysis (Tga) Data," *Energy & Fuels,* **24**(5), 2841-2847 (2010)

Hillier, J. L. and T. H. Fletcher, "Pyrolysis Kinetics of a Green River Oil Shale Using a Pressurized Tga," *Energy & Fuels,* **25**(1), 232-239 (2011)